HELLENIC REPUBLIC
UNIVERSITY OF IOANNINA
SCHOOL OF ENGINEERING
DEPARTMENT OF MATERIALS SCIENCE AND ENGINEERING
POSTGRADUATE COURSE
«ADVANCED MATERIALS»

Master Thesis

Aikaterini Syntychaki

NUMERICAL MODELLING OF BONE FRACTURE HEALING UNDER THE ULTRASOUND EFFECT

Ioannina, 2019

ΕΛΛΗΝΙΚΗ ΔΗΜΟΚΡΑΤΙΑ
ΠΑΝΕΠΙΣΤΗΜΙΟ ΙΩΑΝΝΙΝΩΝ
ΠΟΛΥΤΕΧΝΙΚΗ ΣΧΟΛΗ
ΤΜΗΜΑ ΜΗΧΑΝΙΚΩΝ ΕΠΙΣΤΗΜΗΣ ΥΛΙΚΩΝ
ΠΡΟΓΡΑΜΜΑ ΜΕΤΑΠΤΥΧΙΑΚΩΝ ΣΠΟΥΔΩΝ
«ΠΡΟΗΓΜΕΝΑ ΥΛΙΚΑ»

ΜΕΤΑΠΤΥΧΙΑΚΗ ΔΙΑΤΡΙΒΗ

Αικατερίνη Συντυχάκη

ΥΠΟΛΟΓΙΣΤΙΚΗ ΜΟΝΤΕΛΟΠΟΙΗΣΗ ΤΗΣ ΠΩΡΩΣΗΣ ΚΑΤΑΓΜΑΤΩΝ ΥΠΟ ΤΗΝ ΕΠΙΔΡΑΣΗ ΥΠΕΡΗΧΩΝ

Ιωάννινα, 2019

Η παρούσα Μεταπτυχιακή Διατριβή εκπονήθηκε στο πλαίσιο των σπουδών για την απόκτηση του Μεταπτυχιακού Διπλώματος Ειδίκευσης στην εξειδίκευση:

Βιοϋλικά και Βιοϊατρική Τεχνολογία

που απονέμει το Τμήμα Μηχανικών Επιστήμης Υλικών του Πανεπιστημίου Ιωαννίνων.

Εγκρίθηκε την…….. από την εξεταστική επιτροπή:

1. **Καθ. Δημήτριος Φωτιάδης**, Τμήμα Μηχανικών Επιστήμης Υλικών, Πολυτεχνική Σχολή, Πανεπιστήμιο Ιωαννίνων **(Επιβλέπων)**.
2. **Επικ. Καθ. Λεωνίδας Γεργίδης,** Τμήμα Μηχανικών Επιστήμης Υλικών, Πολυτεχνική Σχολή, Πανεπιστήμιο Ιωαννίνων.
3. **Καθ. Δημοσθένης Πολύζος,** Τμήμα Μηχανολόγων και Αεροναυπηγών Μηχανικών, Πολυτεχνική Σχολή, Πανεπιστήμιο Πατρών.

ΥΠΕΥΘΥΝΗ ΔΗΛΩΣΗ

«Δηλώνω υπεύθυνα ότι η παρούσα διατριβή εκπονήθηκε κάτω από τους διεθνείς ηθικούς και ακαδημαϊκούς κανόνες δεοντολογίας και προστασίας της πνευματικής ιδιοκτησίας. Σύμφωνα με τους κανόνες αυτούς, δεν έχω προβεί σε ιδιοποίηση ξένου επιστημονικού έργου και έχω πλήρως αναφέρει τις πηγές που χρησιμοποίησα στην εργασία αυτή.»

ACKNOWLEDGEMENTS

First, I would like to thank my family for their encouraging and support. Without their help, I would have never accomplished my goals.

I would like to thank my supervisor Prof. Dimitrios Fotiadis, Dept. of Materials Science and Engineering, University of Ioannina, for all his guidance and assistance.

I would also like to thank Dr. Konstantinos Grivas for our excellent collaboration. His help was essential for the completion of this master thesis.

Finally, I would to acknowledge post-doctoral researcher Aurelie Carlier for her guidance.

ABSTRACT

Bone healing is a complicated process during which plenty of cellular and molecular mechanisms occur. The main objective of this study was the presentation of a computational model that simulates these cellular mechanisms during fracture healing and the effects of Low Intensity Pulsed Ultrasound (LIPUS) on bone fracture healing, in order to examine the effect which causes the enhancement of bone healing.

The hybrid biological mathematical model is based on that of Peiffer et al. (2011). The model consists of a system of partial differential equations (PDEs) which describes the spatiotemporal evolution of cell, growth factors, tissues, oxygen and nutrients and acoustic pressure. It was assumed that the ultrasound affects Vascular Endothelial Growth Factor (VEGF) transport, as several *in vitro* studies have reported. Using velocity equations, the growth of the blood vessel network was described.

As a result, this model could be a step towards a better understanding of the influence of ultrasound on fracture healing. However, more experiments should be conducted along with the advancement of a more detailed theoretical background.

ΠΕΡΙΛΗΨΗ

Η πώρωση καταγμάτων είναι μια πολύπλοκη διαδικασία κατά την οποία πληθώρα κυτταρικών και μοριακών μηχανισμών συμβαίνουν. Ο κύριος σκοπός αυτής της εργασίας ήταν η παρουσίαση ενός υπολογιστικού μοντέλου που προσομοιώνει αυτούς τους κυτταρικούς μηχανισμούς κατά τη διάρκεια της πώρωσης των καταγμάτων και τις επιπτώσεις των υπερήχων στην πώρωση καταγμάτων, ώστε να ερευνηθεί η επίδραση που προκαλεί τη βελτίωση της πώρωσης του οστού.

Το υβριδικό βιολογικό μαθηματικό μοντέλο βασίζεται στο μοντέλο του Peiffer et al. (2011). Το μοντέλο αποτελείται από ένα σύστημα μερικών διαφορικών εξισώσεων που περιγράφουν τη χωροχρονική εξέλιξη των κυττάρων, αυξητικών παραγόντων, ιστών, οξυγόνου, θρεπτικών συστατικών και ακουστικής πίεσης. Θεωρήθηκε ότι οι υπέρηχοι επιδρούν τη μεταφορά του αγγειακού ενδοθηλιακού αυξητικού παράγοντα (VEGF), όπως πολλές *in vitro* μελέτες έχουν δείξει. Χρησιμοποιώντας εξισώσεις ταχύτητας, η ανάπτυξη του δικτύου αιμοφόρων αγγείων περιεγράφηκε.

Σαν αποτέλεσμα, αυτό το μοντέλο θα μπορούσε να είναι ένα βήμα προς την καλύτερη κατανόηση της επίδρασης των υπερήχων στην πώρωση του οστού. Ωστόσο, περισσότερα πειράματα θα πρέπει να διεξαχθούν μαζί με την ανάπτυξη ενός πιο λεπτομερούς θεωρητικού υπόβαθρου.

CONTENTS

LIST OF FIGURES

LIST OF TABLES

NOMECLATURE

Abbreviations

2D	Two-dimensional
3D	Three-dimensional
bFGF	Basic fibroblast growth factor
BGLAP	Bone δ-carboxyglutamic acid-containing protein
BSU	Bone structural unit
CCFD	Cell center finite difference
CFL	Courant-Friendricks-Lewy
DO	Distraction osteogenesis
EC	Endothelial cell
EF	External fixation
FVM	Finite Volume Method
GAG	Glycosaminoglycan
Gla	γ-carboxylglutamic acid
IF	Internal fixation
IL-1	Interleukin-1 family
IL-6	Interleukin 6
IL-11	Interleukin 11
IL-18	Interleukin 18
LIPUS	Low intensity pulsed ultrasound
MGP	Matrix Gla protein
MMPs	Matrix metalloproteinases
MOL	Method of lines
ODE	Ordinary differential equation
Npr1	Neuropilin 1
Npr2	Neuropilin 2
OPG	Osteoptotegerin
PDE	Partial differential equation
PDGF	Platelet-derived growth factor
PF	Post fracture
PIGF	Placental growth factor
RANKL	Receptor activator of NF-Kb ligand
TNFα	Tumor necrosis factor alpha
TNFR1	Tumor necrosis factor receptor 1
US	Ultrasound
VEGF	Vascular endothelial growth factor
VEGFR	VEGF receptor

CHAPTER 1

INTRODUCTION

Fracture healing is a complex procedure which occurs in stages and several cells have an active role. After a fracture, there is an inflammatory stage and the callus is created. Tissues differentiate within the callus. The healing is finished when the callus is absorbed and bone remodeled.

An essential part of the bone healing is angiogenesis, since it regulates blood flow. Without adequate blood flow, ischemic necrosis occurs, and repair is delayed. There are many angiogenic growth factors such as vascular endothelial growth factor (VEGF), fibroblast growth factor (FGF) and bone morphogenic protein (BMP). Although the exact mechanisms of angiogenesis are not thoroughly understood, several studies have reported that VEGF has a critical role during bone healing. It activates they endothelial cells to become "tip cell" that create a new blood vessel branch. Several computational models have been introduced in order to investigate the mechanisms of angiogenesis and the cells that participate in the process.

Ultrasound has been used in *in vitro* and *in vivo* experiments and clinical trials in order to enhance the fracture healing. It has been reported that ultrasound stimulate several cells that take part in bone healing, angiogenesis and osteogenesis. As a result, the healing time is reduced. However, the parameters of the ultrasound, such as intensity, are critical of this influence. Although, many experiments have been conducted, the exact mechanisms of the effect of the ultrasound on fracture healing are not thoroughly understood.

The objective of this study was to present a computational model that describe the cellular procedures happening during fracture healing, while also simulating the effect of ultrasound. The computational model was based on that of Peiffer et al. (2011) but was modified in order to include the influence of ultrasound on bone fracture healing. The ultrasound was assumed to affect VEGF transport. As a result, the spatiotemporal tissue evolution under the influence of ultrasound and the effect of ultrasound intensity on vascularization were illustrated.

In chapter 2 the physiology of bone is presented. The composition of bone, the main structural components, the bone cells and blood supply are described. Furthermore, the two types of bone healing are presented. The role of oxygen during bone healing is also mentioned.

Chapter 3 introduces the angiogenesis and the role of VEGF on the inflammation stage, endochondral and intramembranous ossification is described. In addition, the mathematical models that simulate angiogenesis are presented.

In chapter 4 the effects of ultrasound on bone healing are presented. After an introduction in the use of LIPUS in bone healing , experimental results from animal and clinical studies are described. Moreover, the effects of ultrasound parameters on fracture healing are also mentioned.

Chapter 5 begins with the presentation of the computational model of Peiffer et al. (2011) that describe bone regeneration and angiogenesis. Additionally, the new biological model for describing fracture healing under the influence of ultrasound is exhibited.

In chapter 6 a brief introduction of the numerical methods used during the simulation of the model is presented. For each numerical method, the objective and the basic mathematical equations are presented.

In chapter 7 the results from the computational model are presented. Fracture healing is investigated with or without ultrasound for two cases: a normal fracture healing, and the fracture healing of an aged human. The evolution of vasculature, bone matrix density and vascular density for different hydraulic conductivities is

investigated. Finally, the influence of ultrasound intensity on fracture healing was examined.

CHAPTER 2

PHYSIOLOGY OF BONE AND FRACTURE HEALING

2.1 Long bone

The long bones are the type of bone that are longer than they are wide. Bones can be categorized in 5 types: long, short, flat, irregular and sesamoid. The long bones encounter most of the load during daily activities and they are important for skeletal mobility.

The elongation of long bones is a result of endochondral ossification at the epiphyseal plate. The epiphyseal plate is a hyaline cartilage plate in the metaphysis at each end of a long bone. The metaphysis is the narrow portion of a long bone between the epiphysis and the diaphysis. In the epiphyseal plate the bone growth takes place. The plate is found in children and juveniles; in adults, whom growth has stopped, the plate is displaced by an epiphyseal line. This replacement is named epiphyseal closure or growth plate fusion. Bone growth in length is stimulated by the production of a growth hormone, which is a secretion of the anterior lobe of the pituitary gland.

The long bones include: femora, tibiae and fibulae (legs), humeri, metacarpals and metatarsals (hands and feet), radii and ulnae (arms), clavicles (in collar bones), and phalanges (fingers and toes).

The functions of long bones include providing support for the body against gravity and acting as a rigid lever system for muscular action. The primary metabolic function of long bone lies in its ability to serve as a repository for calcium which is necessary for nerve conduction, muscle contraction, clot formation and cell secretion. It is theorized that bone plays a major role in the induction of hemopoietic marrow.

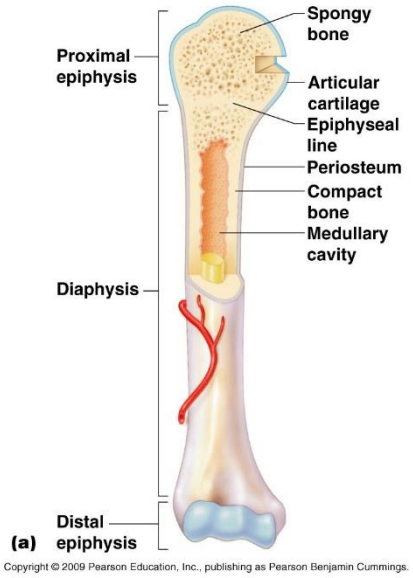

Figure 2.1 The anatomy of bone (2009 Pearson Education Inc., publishing as Pearson Benjamin Cummings)

2.2 Composition of bone

Bone is a composite material containing about 70% mineral (hydroxyapatite), 22% proteins (type I collagen) and 8% water by weight (Webster S.S. Jee, 2011).

Organic phase

Bone consists of organic phase, inorganic phase and water. Type I collagen, proteoglycans and non-collagenous proteins constitute the organic phase. The organic phase composes 50% of bone by volume (25% by weight) and contains 90% type I collagen and 10% proteoglycans.

Type I collagen

Type I collagen is the most abundant type of collagen of the human body which forms large, eosinophilic fibers known as collagen fibers (Henriksen and Karsdal, 2016). It provides bone with tensile strength and flexibility.

There is a basic molecular unit upon which the collagen fibers are built on. This unit is tropocollagen and it is a rod-like asymmetric molecule that its length is approximately 300 nm and 1.5 mm in diameter. It is built up by three polypeptide chains, the α-chains. Two of them are identical (α1-chains) and the other (α2-chain) is slightly different at its amino acid composition. Each α-chain contains approximately 1000 amino acids residues. The majority of the α-chain is coiled in an extended helical conformation with no intra-chain hydrogen bonding between the constituent amino acids. The triple α-chains are coiled together in a helix to form a triple helical collagen molecule of rope-like structure.

However, there is a rapid production of more stable covalent bonds, which contributes to increased stability. These intermolecular bonds are formed between the terminal portions of the α-chains, which are not in the helical structure, but at the helical structure of an adjacent molecule. The nonhelical areas of the tropocollagen molecule are 15 to 30 amino acid residues and are called telopeptides. They are essential for linking the molecules in the final fiber.

The osteoblasts synthetize the collagen for the bone matrix. Collagen is synthetized on membrane-bound ribosomes and it looks like the three α-chains are synthetized simultaneously in an unmodified protein called protocollagen. Then this primary structure of the α-chain is modified by hydroxylation of certain proline and serine residues to form hydroxyproline and hydroxylysine. Once the helical structure of the molecule is formed, no further hydroxylation happens. Then some peptides are released from the protocollagen and the result is a helical tropocollagen molecule.

Proteoglycans

Proteoglycans are proteins which are heavily glycosylated. The elemental proteoglycan unit has a “core protein” with one or more covalently bonded glycosaminoglycan (GAG) chains. (Gabius et al. 2002). The point of connection is a serine residue to which the GAG is connected through a tetrasaccharide bridge. The chains are long, linear carbohydrate polymers that are negatively charged under normal conditions because the presence of uronic acid groups and sulfate. They are a crucial unit of the extracellular matrix. There they form large complexes, both to other proteoglycans and to collagen. The result of the combination of proteoglycans and collagen is cartilage, a resilient and smooth elastic tissue, a rubber-like lining that shields the edges of long bones at the joints.

There is a decline in proteoglycan size and concentration from zone of resting to the zone of mineralized cartilage, probably because of the enzymic digestion of proteoglycans. It is theorized that they induce bone calcification.

Non-collagenous proteins

Several non-collagenous proteins have been insulated from bone, and although their role is not always understood, at least a number appear to be biologically active (Al-Qtaitat et al. 2014). Osteocalcin (or bone δ-carboxyglutamic acid-containing protein (BGLAP)) the most abundant noncollagenous protein in bone comprising about 20% of the non-collagen matrix proteins and is synthetized by osteoblasts. It contains three γ-carboxylglutamic acid (Gla) residues that bind calcium. Its physiological role in mineralization is not certain. It has been hypothesized that rather than facilitating calcification it could retard it, and also that it is a chemoattractant for osteoclasts. It has a usage as a clinically indicator of osteoblast activity. Matrix Gla Protein (MGP), is a hypothetical regulator of extracellular matrix calcification. Lipid and proteolipids are acidic phospholipids that create structures with calcium phosphate and may take part in the mineralization process. Alkaline phosphatase is an ecto-enzyme secreted by osteoblasts and is linked by to the mineralization process. It may take part in the degradation phosphate esters to give a local concentration of phosphate or it may extract pyrophosphate to facilitate mineralization to continue.

Inorganic phase

The inorganic phase mostly consists of hydroxyapatite crystals and provides compressive strength and rigidity to bone. It is a naturally occurring mineral form of calcium apatite. Its formula is $Ca_{10}(PO_4)_6(OH)_2$ to express that the crystal unit cell consists of two entities. Up to 50% by volume and 70% by weight of human bone is a converted structure of hydroxyapatite, known as bone mineral (Junqueira et al. 2003). During bone formation, whether intramembranous of endochondral, uncalcified osteoid is secreted by osteoblasts. Hydroxyapatite crystals then precipitate in an orderly way around collagen fibers present in the osteoid. The osteoid rapidly becomes about 70% calcified in a few days, with maximum calcification occurring after several months.

Components of bone

The bone is composed of the periosteum, articular cartilage, ossified tissue, bone marrow and endosteum. The periosteum is a membrane that envelopes the outer part of the bone and has a dense irregular connective tissue (Brighton et al. 1997). It consists of two parts: the exterior which is a fibrous layer and an interior which is a cambium layer. The inner part contains fibroblasts, while the outer part contains progenitor cells that develop into osteoblasts. Fibroblasts are a category of cell that produce the extracellular matrix and collagen, which are the structural framework for tissues, and have an essential role in wound healing. When a bone fracture occurs, the progenitor cells differentiate into osteoblasts and chondroblasts, which have an essential role to the healing mechanism.

Articular cartilage coats the ends of the epiphyses (Fox et al. 2009). It is a specialized tissue of diarthrodial joints. Its main function is to give a smooth, lubricated area for articulation and to help the transmission of loads with a low frictional coefficient. Bone marrow is a semi-solid tissue in the trabecular parts of bones (Farhi et al. 2009). It is the primary region of the production of new blood cells or hematopoiesis. Endosteum lines the interior area of the medullary cavity of all long

bones (Netter et al. 1987). The ossified tissue is non-homogeneous, porous and anisotropic. It is arranged in cortical and trabecular bone.

Trabecular bone

Trabecular (or cancellous) bone is like a highly porous sponge with a three-dimensional (3D) structure made of connected plates and/or rods, called trabeculae (Guo, 2001). Bone marrow fills the cavities created from the trabeculae network. In the major long bones there is minimal trabecular bone in the diaphyseal regions.

Trabecular bone changes patterns with time and provides support for transmitting applied loads. It is oriented to provide maximum strength while utilizing minimum osseous material.

The basic architecture comprises oriented plates of cortical bone interconnected by rod-shaped supports running perpendicular to the plates. These plates do not form layers in all locations and they vary in width.

The axis of the trabeculae is usually positioned at 90^{o} to deformational forces from muscle tension and weight-bearing. Trabeculae may contain a nucleus of cartilage which is mineralized if they were formed in regions of endochondral ossification. The trabecular surface is coated by a thin film of nonmineralized osteoid produced by the surface osteoblasts. Trabeculae may get significant cross-sectional dimensions in areas of great functional stress. As a result, osteocytes are also commonly observed in lacunae inward the trabeculae. The number, size and distribution of trabeculae are integrally related to the weight-bearing functions of bone as well as to the calcium storage.

Cortical bone

Cortical (or compact) bone is the external wrapping of all bones. Cortical bone has a dense structure of low porosity (typically of a few % to 15%) that appears compact at the macroscopic level (Lakes, 2011). Trabecular (or cancellous) bone is found inside of bones. It has a dense texture, however there are regions that are relatively porous. The two categories of bone can be recognized by their density. The relative quantity of cortical and trabecular bone varies from bone to bone and even between different parts of the same bone. For example, the cortical shell may be very thin in the vertebra but is thick in most long bones. However, in both cases, it is usually composed of lamellar bone. The organization of lamellae varies significantly from region to region within bone, as well as time.

Cortical bone contains an elaborate system of anastomosing canals through which blood vessels permeate every part of the bone. The canals are incorporated as new bone is made during periods of endosteal or periosteal growth. There are two categories of canals: primary and secondary. Primary canals are incorporated initially whereas secondary result from remodeling activity beginning with resorption along a primary canal followed by bone deposition. All canals, no matter their type, usually follow a predominantly longitudinal course in periosteal-derived cortical bone. The canals of endosteal origin may be arranged more irregularly. Some vascular channels may be oriented in a radial direction perpendicular to the long axis of the shaft (Wilkins 2009). These are Volkmann's canals.

A primary canal is surrounded by a variably developed, elongated cylinder of concentric lamellae and this arrangement is named a primary osteon. These primary osteons usually contain only a few layers of lamellae, so they do not approach the size of the more mature, better defined secondary osteons. Primary osteons appear more in

young bone, and they decrease with increasing age. The secondary osteons are called Haversian systems. They come from remodeling procedure along a pre-existing primary canal. Any type of primary osteon can be reconstructed to a secondary osteon, so the distribution of secondary osteons depends on the primary canals. The conversion of a primary osteon to a secondary osteon begins with resorption and ends with deposition of new bone.

This remodeling mechanism allows bone to improved adaption to physical stimuli, since it allows changes of internal structure without significantly changing overall size or shape. As a result, higher concentrations of secondary osteons develop in certain regions with increasing age. These regions correspond to sites of greater stress.

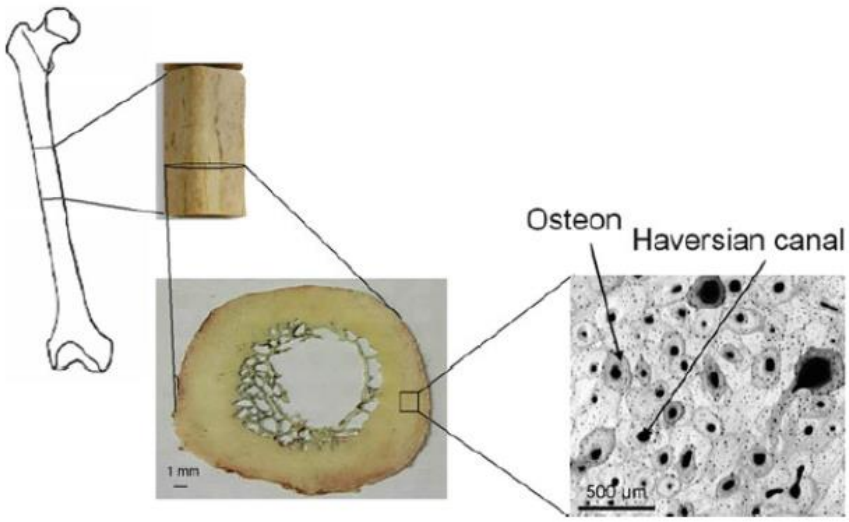

Figure 2.2 The organization of cortical bone. From left to right: mid-diaphysis of a femur; cross section at the mid-diaphysis illustrating the exterior cortical shell and the interior cancellous bone compartment at the periphery of the medullary canal; scanning acoustic microscopy of cortical bone showing the osteons, Haversian canals and osteocytes lacunae (black dots) (Jee, 2001).

2.3 Hierarchical structure of cortical bone

Cortical bone has several organization levels. At the nanoscale, the basic components are collagen and hydroxyapatite. The bone consists of collagen molecules which are organized in collagen fibrils. Collagen fibrils are ordered in collagen fibers (Mitton et al. 2011). The crystals, aligned with the fibers, are settled in the interfibrillar spaces. Mineralized fibers are aligned to form bone lamellae. The orientation of the fibers depends on the lamella and may change within lamellar sublayers. The osteon comprises the bone structural unit (BSU) in cortical bone.

An osteon is a quasi-cylindrical structure comprising of several concentric lamellae surrounding a Haversian canal. They are 100-300 μm in diameter and 10mm long. 3-8 lamellae of 3-7μm thick are wrapped around each osteon. The Haversian canals of 50-100 μm long encompass the blood vessels and nerves.

Osteons

The osteons are made on bone surface by successive periods of matrix apposition in the walls of trenches or grooves or by filling in spaces between trabeculae of trabecular bone. Osteons formed by apposition onto periosteal or endosteal surface

grooves or formed within the lattice of trabecular bone are called primary osteons. The osteons formed in tunnels made during the remodeling are called secondary osteons. The boundaries of secondary osteons are easily identified because a cement line separates them from adjacent mineralized tissue.

During remodeling, the relative position of new osteons generated in existing compact bone is not limited to the limits of former osteons. As a result, parts of older osteons may be eroded by the osteoclasts which synthetize the new osteons. It is possible that partial osteons lie between other osteons.

Cross-session views of cortical bone demonstrate that osteons have a relatively constant overall diameters but significant differences in internal diameters of the vascular canals lined by osteocytes. There is also a variance in the extend of mineral density in each lamella and each osteon in bones in which active remodeling is happening.

In addition to large lumen capillaries and other vessels in osteons, nonmyelinated nerve fibers are also found in many osteons. These fibers carry sensory information. They arise primarily as collaterals from nerves distributed in the periosteum.

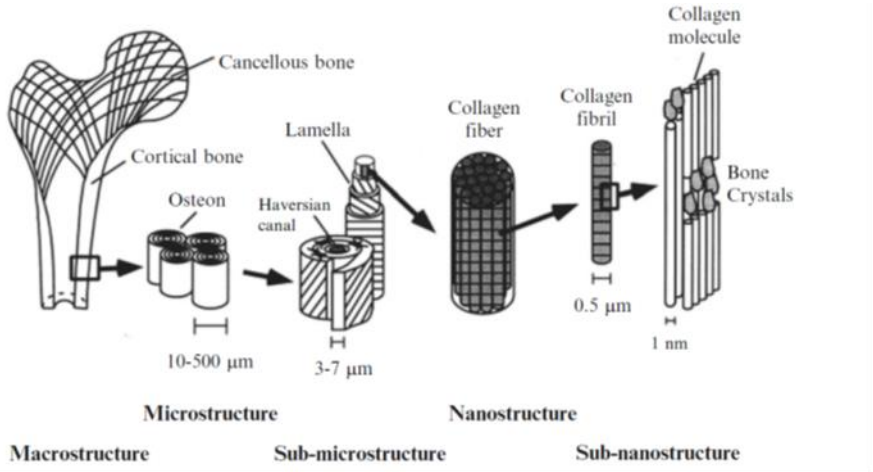

Figure 2.3 Hierarchical structural organization of bone (Rho et al.1998)

2.4 Bone cells

The bone has different types of cells: osteoblasts, osteoclasts and osteocytes. The cells that cover most of the bone surface are the osteoblasts (Jee 2001). On the bone surface there are also osteoclasts. Although there are very few spots where no cell-bone relationship is detected.

Osteoclasts

The role of osteoclasts is to destroy old bone. They come from precursors of bone marrow. They are giant, multinucleated cells with a characteristic ruffled, membranous border along the bone surface. These cells are up to 100 µm in diameter and contain 50 nuclei. They have several Golgi apparatuses for the production of lysosomes which aid in breaking down the old bone. The cytoplasm of osteoclasts may exhibit many vacuoles containing the remains of bone particles that were phagocytosed.

The process of absorption is ensured from the broad number of mitochondria in their cytoplasm (Martinez 1986). The cytoplasm membrane creates an acid environment in which the organic matrix loses its metallic ions and is dissolved. Osteoclasts react strongly for acid phosphate as evidence of their high lysosomal content.

When osteoclasts are actively resorbing both mineral and organic parts of the matrix, a surface irregularity happens to the matrix, that becomes a concavity approximating the cell shape. The presence of a cell in these cavities (Howship's lacunae) is not adequate to call it an osteoclast, because these cavities are usually repaired and filled with new bone by osteoblasts that migrate into the area vacated by osteoclasts (Eberle et al. 2012).

It is thought that modification of the pH at the site of the old bone is a key factor in demineralization and it is clear that the osteoclasts are capable of producing plenty of organic acids.

Osteoblasts

The osteoblasts are bone-forming cells. Other adjacent cells may resemble osteoblasts morphologically, but they may be differentiating osteo-progenitor cells. They are typically cuboid cells, each with a single, rounded nucleus usually surrounded by extensive endoplasmic reticulum (Majeska 2001). This rough endoplasmic reticulum is associated with protein production, collagen and proteoglycan found in the osteoid.

Interspersed amid the rough endoplasmic reticulum are mitochondria, which are usually round. They consist of a double membrane, with the inner membrane folded and evaginated to form the characteristic cristae. Some mitochondria contain small granular mineral deposits attached to the outer cristae surface. These dense granules show a high concentration of calcium and phosphate, with traces of magnesium. Some organic substance is also present. Mitochondria, besides their ability to produce energy for the cells, are able to remove calcium ions from cell cytoplasm. Mitochondrial calcium is removed by coprecipitation with phosphate, resulting the formation of mitochondrial granules. This is essential for the regulation of cytoplasmic calcium levels to normal levels of 10^{-6} to 10^{-7} M. Transient rises above these normal intracellular levels are damped by the accretion of excess calcium in mitochondria and in other cell structures with less calcium sequestrating capacity. Osteoblasts adjacent to newly mineralizing matrix often show increased mitochondrial granules, where osteoblasts in adjacent fully mineralized zones show less.

Osteoblasts also have a prominent Golgi apparatus for packaging and modifying proteins for secretion. The organization of cellular components is ordered, with most of the nuclei and other cell components in a similar position in adjacent cells of an active osteoblast population. Osteoblasts are active when they are participating in matrix production.

They are differentiated from mesenchymal stem cells. When they are activated they change their shape and create new ossified organic matrix, the osteoid. They are found as a continuous layer on bone surfaces undergoing active deposition. All organic components of bone matrix are synthetized and secreted by osteoblasts. It has been theorized that they have a role in the initiation of mineralization and modulating electrolyte fluxes between the extracellular fluid and bone fluid. They react strongly for alkaline phosphatase, an enzyme often correlated with mineralization. Then the osteoid

is calcified to create mineralized bone. After mineralization osteoblasts become osteocytes and remain in the mineralized bone matrix.

Osteocytes

The osteocytes are bone-maintaining cells. They are osteoblasts that become totally entrapped in the matrix being synthetized. They sit in cavities inside the organic matrix. With subsequent mineralization of the newly formed matrix, the osteocyte is bounded by a mineralized wall, defining a lacunar space that is completely filled by osteocytes (Majeska 2001). A thin, incomplete layer of nonmineralized pericellular osteoid separates the cell margin from the mineralized lacunar wall. The lacunar surface of the mineralized matrix is a hyperdense area of matrix.

Since the osteocytes result from entrapment of osteoblasts, young osteocytes have many features of active osteoblasts. They contain rough endoplasmic reticulum and they have a Golgi complex, mitochondria and large cell volume. They have oval shape and stick out in small canals, the canaliculi, where they are connected with other osteocytes and osteoblasts. They maintain an extensive network of contacts with adjacent cells via several long, tapering cellular processes lying within openings in the bone called canaliculae. Gap junctions join processes from adjacent cells. These junctions provide a pathway for metabolic diffusion and are essential to maintain viable osteocytes and bone. With continued maturation of the surrounding matrix with mineral, the processes occupy increasingly smaller canals, ultimately occupying most of the canaliculus, with only a thin coat of non-mineralized matrix separating the process from the mineralized canalicular wall. The extension of processes governs the formation and retention of a canalicular network. Processes of adjacent osteocytes may unite end to end or may overlap, forming special junctions at points of cell-cell contact.

An interruption in the canalicular network may result in osteocyte death. The part of bone affected then becomes necrotic and is removed by osteoclasts. Their role is to sustain bone organic matrix and discharge calcium ions from the organic matrix when it is necessary. A small number of osteocytes absorb mineral organic matrix.

Osteocytes that are fully surrounded by mature bone are more stalkless. Since there is little space for additional collagen to be deposited, the organelles of the osteocyte are reduced. Rough endoplasmic reticulum is reduced, with only occasional saccules present. The Golgi complex is reduced to a few lamellae. Mitochondria are larger than those of osteoblasts, and less in quantity. The osteocytes have been delegated to a maintenance role.

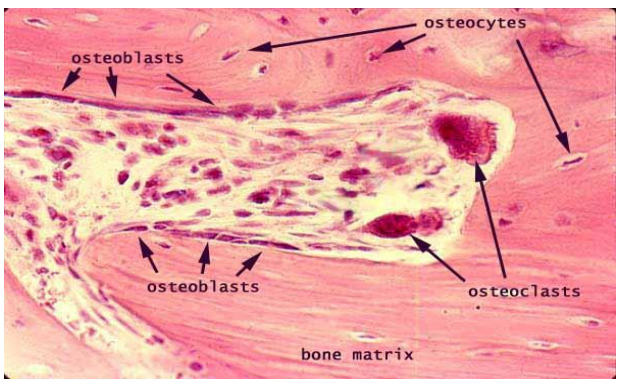

Figure 2.4 The replacement of old bone tissue by new bone tissue (Hunt 2008)

Bone surface

The bone surface can be in one of three functional states: resorbing, forming, or quiescent (Majeska 2001). Surfaces which are bone forming are characterized by osteoid and by a layering of osteoblasts. In contrast, resorbing surfaces contain scalloped concavities (Howship's lacunae) that frequently contain osteoclasts or have osteoclasts located nearby. Quiescent (or resting) bone surfaces are free of osteoclasts and osteoblasts. They are lined by bone-lining cells, osteocytes.

Surface	Surface Area ($\times 10^6$ mm^2)	Total Surface (%)
Periosteal	0.5	4.4
Endocortical (cortical–endosteal)	0.5	4.4
Intracortical–Haversian or osteonal	3.5	30.4
Trabecular–endosteal	7.0	60.8
Total surface	11.5	100.0

Table 2.1 Adult bone surfaces (Recker 1983)

Factors	Cortical	Trabecular
Fractional volume (mm^3/mm^3)	0.95	0.20
Surface/bone volume (mm^2/mm^3)	2.5	20
Total bone volume (mm^3)	1.40×10^6	0.35×10^6
Total internal surface (mm^2)	3.50×10^6	7.0×10^6
Forming (%)	3.0	6.0
Resorbing (%)	0.6	1.2
Quiescent (%)	96.6	92.8

Table 2.2 Comparison of Cortical and Trabecular BoneVolume and Bone Surface (Recker 1983)

2.5 Blood supply

The blood that enfolds bone cells is unique, having ion concentrations and organic components that are different from those of general extracellular fluid. This suggests that either epithelial cells of vessels within bone are different from those in other organs or that some other cellular layer serves to partition general extracellular fluid from bone fluid. It has been suggested that the osteoclasts serve as a functional membrane, separating these two compartments.

There are three major sources of arterial blood supply: the nutrient supply, the metaphyseal arteries and the epiphyseal arteries. The routing of blood is closely connected to patterns of growth, modeling, and remodeling.

The nutrient artery penetrates the long bone, in response to appearance of the primary center of ossification. As the nutrient artery reaches the medullary cavity, it separates into ascending and descending medullary arteries. These medullary arteries

supply marrow tissue, then give off many penetrating branches which enter the inner, endosteal bone surface via Volkmann's canals and continue generally in a radial direction to the outer one third of the cortex near the periosteal surface.

Several metaphyseal arteries pierce the periosteal surface and branch extensively beneath the epiphyseal plate to supply the bone and cartilage in that region. The epiphyseal arteries usually enter the bone above the epiphyseal plate to supply bone and cartilage in that area. Once the epiphyseal plate has closed and growth is completed, the metaphyseal and the epiphyseal circulations are merged.

The periosteal arteries also contribute to the blood supply, but to a lesser extend in normal bone. They supply periosteal structures primary but may penetrate slightly into the periosteal bone surface to supply the outer one third of the cortex. They gain access to the marrow cavities by way of nutrient canals. The periosteal blood circulation also has an essential role in primary fracture callus formation.

Venous drainage from a long bone occurs via venous pathways that accompany the arterial supply. Small venules in the cortex drain periosteally and endosteally. Large emissary veins collect from the central medullary sinus and a periosteal venous system. The central medullary sinus drains the cortical bone and connects with veins exiting at either ends of the bone. For the metaphyseal and epiphyseal regions, venous drainage proceeds parallel to the arterial supply with veins and venules accompanying corresponding arteries and arterioles.

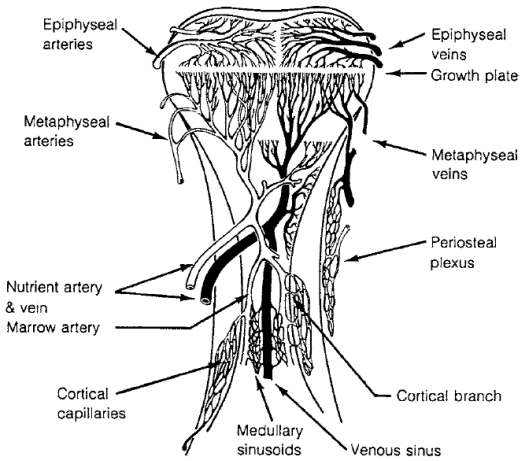

Figure 2.5 Diagram of the blood supply of bone (Wiess 1988)

2.6 Fracture healing

A fracture is technically an abrupt break of the calcified structure of a bone caused by an extrinsic or intrinsic mechanical force. A traumatic fracture is a gross break, with or without shattering of the cortex of a long bone (Cowin 2001). A stress fracture can happen in a normal bone that has been subjected to repeated stresses, that is, in association with strenuous physical activity. Stress fractures happen most commonly in the bones of the foot, the proximal shaft of the tibia, the distal shaft of the femur, the femoral neck and the pubic ramus. A pathologic fracture is secondary to an underlying disease progress. An open fracture is when the injury involves the skin and closed fractured is when the skin remains unharmed.

During fracture healing, the body promotes the repair of the bone fracture. When a bone is fractured, the tissue responses are specific all along the stages of the

healing progress. There is an orderly development of different tissue types. There are three stages. The initial stage is the formation of granulation tissue. The next stage is progressively succeeded by a fibrocartilaginous phase and the final a bony phase. In fractures that do not heal normally, for example in a case of infection, the early stages last for long periods of time. The healing mechanism is primarily regulated by the periosteum. Precursor cells, that develop into chondroblasts and osteoblasts which are critical to the healing of bone, come from the periosteum (Ferretti et al. 2014). Other sources of precursor cells are the bone marrow, endosteum, small blood vessels, and fibroblasts.

Chondroblasts are mesenchymal progenitor cells which, from endochondral ossification, will form chondrocytes in the growing cartilage matrix (Pearle et al. 2005). They are essential in chondrogenesis because they develop into chondrocytes and cartilage matrix which will ultimately form cartilage. Chondroblasts are named chondrocytes when they are in the cartilage matrix. They consist of proteoglycan and collagen fibers, until they are in the matrix lacunae. Once they are in the cartilage matrix, they develop the cartilage matrix by synthetizing more cartilage extracellular matrix rather than by dividing further.

Chondrocytes, through most of the epiphyses, lie in lacunae surrounded by extensive amounts of extracellular matrix (chondroid). Their prime function is to maintain the matrix during growth and prior to ossification (Lee et al. 2013). The cell surface is irregular and has plenty of short cell processes extending out of the matrix. They have an important role in the production of matrix collagen and protein polysaccharides.

One of the main reasons for unfit fracture healing is the lack of angiogenesis. When a fracture is open, it is considered to have a greater risk of non-union because of deprovision of normal blood supply due to tissue damage. As a result, the vascular callus growth is decreased, bone necrosis is increased and the resistance to infections is reduced. Thus, blood flow is crucial for fracture healing. Vessels provide nutrients necessary for the fracture healing, so angiogenesis is essential for osteogenic repair and takes place before the osteogenesis. The new vessels transfer osteoblast and osteoclast precursors to remodeling areas. This process indicates that the endothelium regulates osteoprogenitor cell transfer to the fracture region. Osteoclast precursors attach to the endothelium to migrate to remote bone resorption areas.

Primary healing

Primary healing (or direct healing) happens when there is a stable anatomical reduction, without gap creation. During this stage occurs the remodeling of lamellar bone, the blood vessels and the Haversian canals without callus creation.

Contact healing: happens when the gap in the bone is up to 0.01 mm, and the strain is up to 2%. Osteoclasts form cutting cones and they develop over the fracture lines, creating cavities at a rate of 50–100 μm per day. Osteoblasts lie in the cavities. As a result, lamellar bones formats with a longitudinal orientation along the long axis of the bone. The Haversian system is permeated by blood vessels (Marsell et al. 2012).

Gap healing: when the gap is between 800μm and 1nm, osteoclasts fill the fracture site. Then lamellar bone formates with perpendicular orientation along the axis of the bone. As a result of this orientation, lamellar bone is feeble, and a secondary reconstruction is essential in order to change the orientation of the lamellar bone longitudinally (Marsell et al. 2012).

Secondary healing

The most common way of bone healing is the secondary healing or indirect bone healing. During this process, only endochondral ossification occurs but sometimes intramembranous ossification can occur too. The intramembranous ossification, regulated by periosteal layer of bone, happens without the creation of callus. For endochondral ossification, deposition of bone occurs after the mineralized cartilage (Affshana et al. 2018). There are three major stages of fracture healing: 1. reaction, 2. repair, 3. bone remodeling.

Repair in long bones with periosteum: Within the first few hours after someone sustains a fracture of long bone, the cells of the inner lining of periosteum begin to synthetize DNA and proliferate. This activity happens throughout the periosteum of the fractured bone, not just at the area of the injury. These cells also produce fibroblasts and cells with chondrogenic abilities.

After fracture, blood cells concentrate close to injury site and blood vessels constrict, in order to stop further bleeding. Within a few hours, a hematoma also forms within the fracture area, owing to damage the blood vessels in the periosteum, endosteum, marrow and Haversian canals. Periosteal healing with its proliferative activity and the restitution of vascular continuity with the overlying muscle are essential steps in healing process. The hematoma acts as a template for callus formation and has a variety of blood-borne formed elements including macrophages that resorb fibrin and a fibroblast-rich granulation tissue that forms. The granulation tissue is a loose accumulation of cells, infused with small blood vessels.

The macrophages release inflammatory mediators such as cytokines (tumor necrosis factor alpha (TNFα), interleukin-1 family (IL-1), interleukin 6 (IL-6), 11 (IL-11), and 18 (IL-18)) and raise blood capillary permeability. Inflammation culminates by 24 hours and completes by 7 days. Through tumor necrosis factor receptor 1 (TNFR1) and tumor necrosis factor receptor 2, TNFα mediates the differentiation of mesenchymal stem cells into osteoblast and chondrocytes. IL-1 and IL-6 have an important role in bone healing. IL-1 advocates the creation of callus and blood vessels. IL-6 promotes the differentiation of osteoblasts and osteoclasts. All the cells from the blood clot degenerate and die (Brighton et al. 1991). In this region, the fibroblasts replicate.

When a fracture happens, at the region of the fracture there are devitalized muscle and bone fragments. The muscle fragments undergo autolysis within 5 to 10 days. When they occur as flaps with an initially intact blood supply, they tend to undergo fibrous degeneration, the bone fragments usually show deposition of new bone, possibly because of migrating cells of periosteal origin. The medullary components that were deprived of their blood supply undergo fatty degeneration. However, when the medullary circulation has not been seriously affected by the fracture, some endosteal new bone formation is possible. Osteoblasts can form in the early callus, though osteoclasts are not usually present.

The vascular compromise and the somewhat anaerobic conditions that exist in the early stages of fracture provide the microenvironment for the evolution of a callus that becomes more cartilaginous that osseous (Angle et al. 2015).

Fibrocartilaginous callus stage

When the fibrocartilaginous callus is mature, it consists of a translucent dense fibrous tissue, fibrocartilage and cartilage. However, during the formative stages,

unmineralized tissue dominates. The cartilage happens in nodules that are separated by irregular bands of fibrocartilage. After 3 weeks of the fracture, the callus is wedge-shaped, with the fibrous septa converging at the middle of the fracture gap. These septa carry large-caliber vessels that originate from the repaired periosteal and medullary circulation.

The richer vascular supply of the fibrocartilaginous callus increases the oxygen tension of the tissue in order to occur two changes. First, the fibrocartilaginous components calcify and the chondrocytes at the periphery of the nodules convert to osteocytes (Boyce et al. 2009). Second, osteoclasts appear. As a result, ossification and resorption can proceed on different regions of the same trabeculae that begin to form in the callus. The devitalized parts of cortical bone begin to be resorbed and remodel. The trabeculae close to the fracture gap become thicker and form into the structure of bone lamellae typical of osteons to increase the stability and strength of the fractured bone. The fibrocartilaginous callus is progressively transformed into a bony callus.

Bony callus stage

This stage peaks when the chondrosteoid tissue of the fibrocartilaginous callus is totally converted to bone, that is, when the fractured ends of cortex have joined. Cortical bone has a rich vascular supply and because of many collateral intracortical vessels, most of the endosteal cells and osteocytes survive after fracture (Goodship 2001). Some osteocytes die locally after fracture, about 1cm back from the fracture in cortical bone and about 1mm back from the fracture in trabecular bone. During the formation of the osseous callus, osteoclastic resorption removes dead bone from the periosteal and endosteal surfaces. The cortex begins to become trabecularized even beyond the zone of osteoclastic activity.

The ultimate unification of the bony shaft depends on two events: 1. the continued formation and strengthening of the subperiosteal trabeculae that begin to bridge the fracture gap and 2. continued remodeling of the cortex. The rate of healing is dependent of the length of the gap of the fracture and the surface area of the fracture line. As a result, a communicated fracture may take a longer time to heal than a spiral fracture because it brings a much larger number of progenitor cells.

Cells are proliferated, differentiated and organized in order to create new chondrocytes and osteoblasts in the granulation tissue. The extracellular organic matrices of tissues consist of these cells. Callus tissue has two categories: hard and soft. In the hard callus the intramembranous ossification occurs and in the soft callus the endochondral ossification happens. Near the fracture site osteochondral progenitor cells differentiate into chondrocytes. Then these chondrocytes become hypertrophic and undergo mitosis and synthetize cartilage. Blood vessels are formed in the calcified cartilage, which is then absorbed by osteoclasts. Then the cartilage is replaced by ossified tissue and woven bone is formed via endochondral ossification.

Bone remodeling

When old bone tissue is replaced by new bone tissue, this process is called bone remodeling. Remodeling happens in the adult skeleton to maintain bone mass, to adapt the skeleton to the loads or to repair microcracks. Bone remodeling is also implicated in fracture healing (Tamas et al. 2015). Bone cells act in turns during the remodeling process. First osteoclasts are activated to discard the old bone, then the osteoblast to

form new bone. After mineralization osteoblasts become osteocytes. Osteoid is the new bone tissue which is not mineralized at the start of the remodeling process.

For cortical bone the remodeling process takes place along tunnels and creates osteons. For trabecular bone the remodeling process occurs at the surface of the trabeculae. Although the exact mechanism of bone remodeling is not entirely known at the present time, it is thought that osteocytes and canaliculi act as mecanotransducers to trigger bone remodeling.

There are two categories of bone according to the way of collagen in the osteoid: woven and lamellar bone. In woven bone, collagen fibers have an irregular arrangement. Lamellar bone has a regular parallel alignment of collagen into lamellae sublayers.

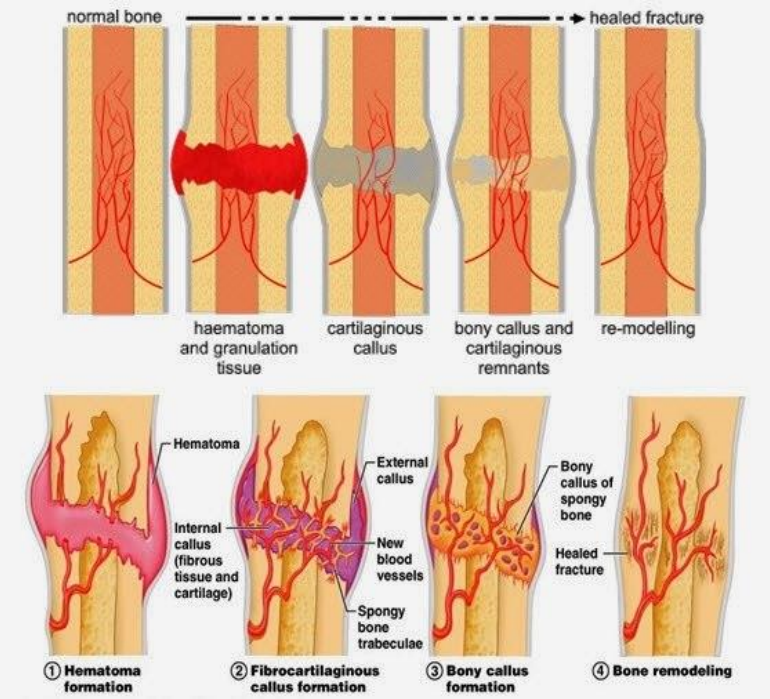

Figure 2.6 Stages of bone healing (2004 Pearson Education, Inc. Publishing as Benjamin Cummings)

Woven bone

Woven bone is formed during fracture healing in adults. When a fracture occurs, woven bone is remodeled, and lamellar bone is placed (Currey 2002). When woven bone formed by the periosteum gradually incorporates into lamellar bone, trabecular bone (especially the subperiosteal type) is converted into cortical bone by compaction and modeling. This procedure is happening in certain parts of the metaphysis during growth.

All bone in healthy human adults is lamellar bone (Singh 2014). It is a characteristic of initial bone formation within fracture callus or adjacent to local inflammatory processes and can also be found as tumor-induced new bone. It also appears as the initial bone formed by the periosteum, particularly if the periosteum is pathologically stressed to undergo a rapid bone formation.

This type of bone shows variation in mineral density, especially when comparing endochondral woven bone with periosteal woven bone. It has a limited degree of orientation because short bundles of oriented collagen are present.

Woven bone responds biomechanically in a different way than mature osteon bone. Its physical properties show no directional preferences, as a result of lack of structural orientation, less organization, relatively low density and high-water content. These characteristics give woven bone greater flexibility, lower modulus of elasticity and less strength to be able to resist the same forces as lamellar bone without significant deformation. However, these properties of woven bone allow a certain resistance to encountered biologic forces, while allowing rapid bone growth. The lack of orientation allows it to be laid down rapidly and probably facilitates later remodeling features, which also enhance repair at all ages.

Lamellar bone

Lamellar bone is mature and biomechanically responsive. It has a lamellated structure, with tine collagen fibrils in each of the multiple lamellae running in different directions. In trabecular bone the lamellae usually run parallel to the trabeculae, whereas in cortical bone many patterns occur. This is especially present in the osteons, in which concentric orientation of multiple layers occurs around vascular canals.

When lamellar bone occurs in the midshaft of a long bone, it consists of concentrically arranged laminae. The thickness of the lamina is about 200 μm (Gui 2016). Between each lamina and the next there is a net-like system of blood vessels. Occasional large radial vessels through a lamina connect these nets. Each lamina is split into the three areas. The first, extends from the surface of the vascular network to about one third of the way across lamina. It is composed of highly organized dense bone. The second extends the next one third of the distance. It is composed of a poorly organized tissue. This zone is interrupted in the middle by the boundary between the two blood supply networks bounding the lamina. Under ordinary light microscopy, this boundary appears as a bright line.

One layer of lamellae is isotropic and the other is anisotropic. There are three types of osteons identified according to the direction of collagen bundles and successive lamellae. In the first type, the prevalent direction of fiber runs along the longitudinal axis of the osteon (Turner et al. 2001). However, the inner and outer perimeters of the osteon often contain a few concentric lamellae running transversely around the osteon axis. In the second type of osteon, the majority of bundles run concentrically around the osteon axis. The third type of osteon shows alternating light and dark lamellae under polarized light. The basic lamellar pattern has an essential role in the mechanical properties of individual osteons. Longitudinally oriented osteons have greater tensile strength and transversely oriented osteons have greater compressive strength. As the bone growths, there are changes in the pattern of the osteons during continual remodeling in response to the normal physiologic stresses.

Each lamella contains highly oriented collagen arrays that do not branch. Collagen has a basically parallel orientation, however, the fibers form a continuum with frequent inner connections from one bundle to another, not only within the lamella. Many fibers traverse the interlamellar zone as they pass from one lamella to another. This arrangement increases the resistance of bone to mechanical stress.

The role of oxygen in fracture healing

An important factor for delayed fracture healing of nonunion is inadequate blood supply (Dickson et al. 1995). Ischemia creates a hypoxic environment at the fracture area. As a result, cells die, and the differentiation of chondrocytes and

osteoblasts is delayed (Zhang et al. 2002). Oxygen has a role in many cellular processes that are essential for normal fracture healing. Oxygen is needed for aerobic metabolism and for the activity of various enzymes which take part in fracture healing. Lack of tissue oxygen has a direct effect on collagen synthesis, because oxygen is essential for hydroxylation of proline and lysine during collagen cross-linking and bundle formation (Kivirikko et al. 1967). Finally, oxygen is a crucial signaling molecule, which regulates the expression of several angiogenic genes (Fong et al. 2009).

Tissue oxygen may affect stem cells responses when a fracture occurs. Oxygen regulates stem cells mobilization, maintenance, and recruitment to the regions of injury (Lin et al. 2006). It has been reported that oxygen tension influences osteoblasts, osteoclasts, and chondrocytes. Hypoxia affects the expression of genes in cultured osteoblasts, causes dedifferentiation on cultured chondrocytes and stimulates the osteoclasts formation. It is considered that hypoxia influences angiogenesis.

Fracture healing and aging

When age increases, most of the people endure physiological changes, such as the evolution of osteoporosis. As a result, they are more prone to fractures and consecutive healing complications (Gruber et al. 2006). However, few large clinical studies have investigated the effect of age alone on bone fracture healing.

Delayed healing in aged patients may be due to impaired angiogenesis (Rivordet et al. 2012), reduced levels of growth factors and lower rate of mesenchymal progenitor cell division and differentiation. Nikolaav et al. (2009) found that patients aged 65 years and above have longer fracture healing duration that patients aged 18-40 (19.38 weeks and 16.19 respectively). Lu et al. (2005) found that in aged mice the beginning of the periosteal reaction was delayed. As a result, cell differentiation was delayed, the bone formation was decreased, osteogenic invasion of cartilage was delayed, the period of endochondral ossification was protracted, bone formation was decreased, and bone remodeling was impaired. When regulation of osteogenic differentiation is disrupted, it possibly conduces to impaired fracture healing. Bergman et al. (1996) reported that fibroblasts exhibit an age-related decrease, no matter the species examined. Baxter et al. (2004) indicated that when fewer cells are forced to differentiate (in the case of an aging person), they may pre-nature, senesce, and decrease bone healing capability.

Lu et al. (2005) showed that there are delays in osteoblast and chondrocyte differentiation in aging patients. Angiogenesis is impaired because of reduced expression of VEGF and other anabolic factors. With age, there are changes in matrix structure and growth factor concentrations and cell-matrix interactions are disturbed (Frantz et al. 2010, Kurpas et al. 2009).

The capability of bone cells to feel, proves and react to mechanical stimuli decreases with age (Wu et al. 2010). Szulc and Seeman (2009) concluded that with age, the bone deposition decreases after each cycle of bone remodeling. This may be de to reduced number of stem cells or a reduction in lifespan of osteoblasts. Lee et al. (2005) showed that signals for the differentiation of stem cells decline with age. Grynpos et al. (1994) indicated that patients aged 51-79 yrs has less extracellular bone matrix proteins that individuals aged 18-37 yrs.

CHAPTER 3

ANGIOGENESIS AND BONE HEALING

3.1 Role of angiogenesis and VEGF

Angiogenesis is the procedure of establishing new blood vessels from pre-existing ones. This process begins with the remodeling of vascular endothelial cell precursors. As a result, the vessels grow to form branches and develop new vessels. This process is regulated by the angiogenic growth factors and their receptors (Stegen et al. 2015).

The first stage of angiogenesis is the sprouting of endothelial cells. When a vessel is resting, endothelial and mural cells mold a basement membrane around the vessel tube, which blocks endothelial cells from migrating. When a tissue is growing, and new blood cells are required, angiogenic growth factors are produced locally and they stimulate the endothelium cells to degrade the basement membrane (Emanuelle et al. 2012). This process is regulated by matrix metalloproteinases (MMPs). The activity of MMPs enhances the angiogenesis by releasing angiogenic factors in the matrix. Because of these angiogenic signals, some endothelium cells become mobile and vent filopodia.

The tip cells are the beginning of a newly formed vessel, the stalk cells are the trailing endothelial cells. The tip cells' filopodia can "sense" the environment for attractive signals to guide the sprouts into the tissue. Stalk cells from tubes and branches. New vessel circuits are formed when two adjacent tip cells interact. These attachments are consolidated by several procedures such as the deposition of extracellular matrix, the induction of pericytes, decreased proliferation of endothelial cells and enhanced creation of cell junctions. After the maturation of the endothelium, vascular branches are modified to reach the required local rigidity.

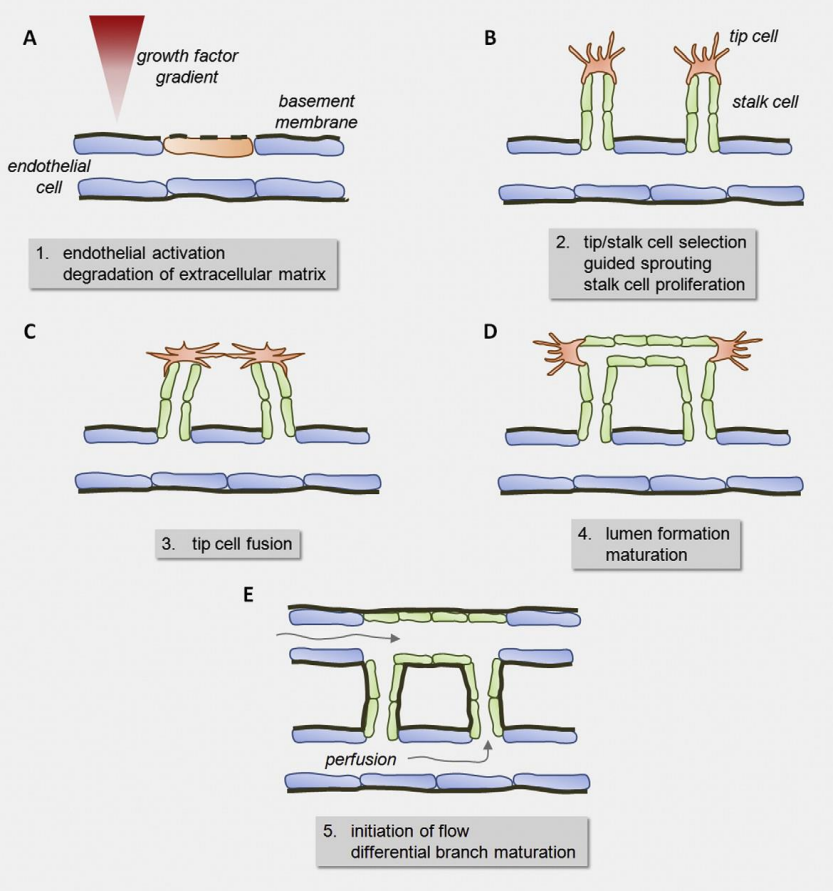

Figure 3.1 Physiological blood vessel formation (Stegen et al. 2015)

VEGF

VEGF is one of the most important angiogenic growth factors and has an essential role during angiogenesis. It has been proposed that VEGF has a role as a focal moderator for other angiogenic factors. It has been reported that VEGF halts the angiogenic operation (Hu et al. 2016). It is found in mammals as a group of structurally homologous glycoproteins: VEGF-A, VEGF-B, VEGF-C, VEGF-D, VEGF-E and placental growth factor (PIGF). The different forms of VEGF have various solubility and bioactivity because of the ability of VEGF to attach to the extracellular matrix to variable degrees.

VEGF-A, the most abundant form, regulates many cellular events such as proliferation and migration of endothelial cells, remodeling of the extracellular matrix, survival of new blood cells and increased vascular permeability (Friehs et al. 2012). At least five isotopes subsist: VEGF121, VEGF145, VEGF165, VEGF189 and VEGF206. VEGF-B is activated during embryonic angiogenesis. VEGF-C and VEGF-D are essential for lymphangiogenesis. PIGF is crucial during pathological angiogenesis. PIGF stimulates angiogenesis, but only in pathological junctures. It is thought that has a role in angiogenesis of placenta.

VEGF receptors

VEGF binds to VEGF receptors (VEGFRs), a group of receptor tyrosine kinases, Neuropilin 1 (Npr1) and Neuropilin 2 (Npr2). There are three VEGFRs which have similar structure (Thomas 2013). They contain a transmembrane helix, an extracellular ligand binding domain, and a cytoplasmic area containing a kinase domain. When the ligand has bound the extracellular domain, the intracellular domain autophosphorylates, and the receptors undergo dimerization.

Receptor	Ligands	Localization
$VEGFR_1$	VEGF-A, VEGF-B, PIGF	Vascular endothelium
$VEGFR_2$	VEGF-A, VEGF-C, VEGF-D, VEGF-E	Vascular and lymphatic endothelium
$VEGFR_3$	VEGF-C, VEGF-D	Lymphatic endothelium

Table 3.1 The VEGFR receptors and their ligands (2017 Springer)

$VEGFR_1$

VEGF-A binds $VEGFR_1$ with higher affinity than $VEGFR_2$, but the tyrosine kinase activity of $VEGFR_1$ is weaker than $VEGFR_2$. It has been suggested that PIGF acts by replacing VEGF-A from $VEGFR_1$. As a result, the bioavailability of VEGF-A is increased. Cells with absence of $VEGFR_1$ have lower sprout formation and migration. Thus, it is believed that $VEGFR_1$ has a positive regulatory role during angiogenesis. During certain circumstances, $VEGFR_1$ transduces a mitogenic signal like $VEGFR_2$.

$VEGFR_2$

$VEGFR_2$ is the main VEGF signaling receptor and is essential for endothelial survival, migration, and proliferation. It innervates vascular permeability and invasion. $VEGFR_2$ has at least four autophosphorylation areas.

VEGFR$_3$

VEGFR$_3$ has an essential role during lymphangiogenesis. Studies in VEGFR$_3$-deficient embryos have shown defects in vasculogenesis. This may be due to decreased VEGFR$_3$ signaling. It is also possible that this is a result of the reduction of VEGF-C bioavailability to VEGFR$_2$ due to binding to VEGFR$_3$. It is believed that VEGFR$_3$ may negatively regulate VEGFR$_2$ signaling.

3.2 The role of VEGF in the inflammation phase during bone repair

After a bone trauma, the hematoma and the inflammation phase initiate bone repair. VEGF is in the hematoma after a bone fracture. The hypoxia in the hematoma stimulates VEGF expression in neighboring bone cells (Street et al. 2000). After the fracture, neutrophils are increased to remove bone debris and microbial pathogens. Their release is regulated by osteoblasts. It has been reported that VEGF stimulates neutrophil chemotaxis. Then macrophages and cytokines are released to the fracture area. The cytokines also stimulate VEGF expression. Macrophages release angiogenic factors, thus VEGF may induce angiogenesis indirectly via macrophages and directly by targeting endothelial cells (Wu et al. 2013).

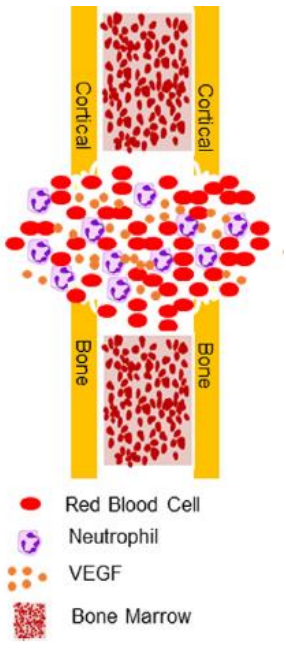

Figure 3.2 Expression and functions of VEGF in the inflammation phase (Hu et al. 2016)

3.3 The role of VEGF in endochondral bone ossification during bone repair

It is believed that VEGF may influence the differentiation of skeletal stem cells from periosteum and bone marrow into chondrocytes or osteoblasts. VEGF also has an essential role in the survival of epiphyseal chondrocytes. During later stages of endochondral ossification, chondrocytes halt proliferation, develop to hypertrophic

chondrocytes, and synthetize collagen. When chondrocytes are hypertrophic, they express Osterix, a strong inducer of VEGF expression. As a result, high levels of VEGF are produced, osteoclasts are recruited into the hypertrophic cartilage and the cartilaginous template is replaced by bony callus. When osteoblast precursors produce high amounts of VEGF, due to Osterix expression, this VEGF induces their differentiation (Carlevaro et al. 2008).

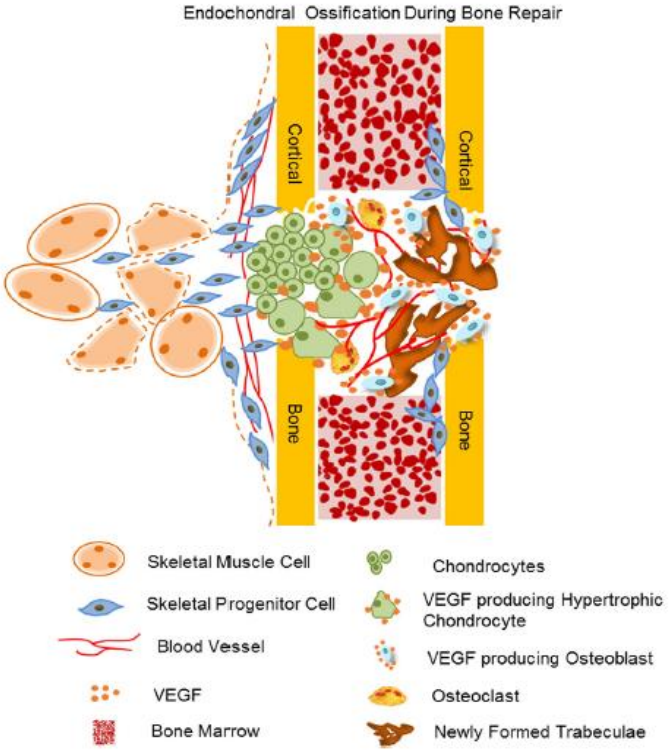

Figure 3.3 The role of VEGF in endochondral bone ossification during bone repair (Hu et al. 2016)

3.4 The role of VEGF in bone healing mediated by intramembranous ossification

The intramembranous bone formation depends on conjugation of osteogenesis and angiogenesis and VEGF has a crucial role in this procedure (Hu et al. 2016). Osteoblasts release VEGF which stimulates angiogenesis via receptors on endothelial cells. As a result, the amount of oxygen and nutrients essential for osteogenesis is increased. When vascularization is increased, it can also lead to inflow of skeletal stem cells and (pre)osteoblasts and to increased levels of osteogenic growth factors such as BMP2 or BMP4. There are also anabolic signals that enhances further the mineralization and differentiation of osteoblasts. Osteoblasts that are maturing also release angiogenic factors, including VEGF. The levels of VEGF have an essential role during bone healing. Little amount of VEGF may disrupt communication between blood and bone vessels which could endanger bone healing. Large amount of VEGF has harmful effects on bone healing, possibly due to inhibition of osteoblastic maturation or by the induction of osteoclasts that absorb the bone that is newly formed (Nakagawa et al. 2000).

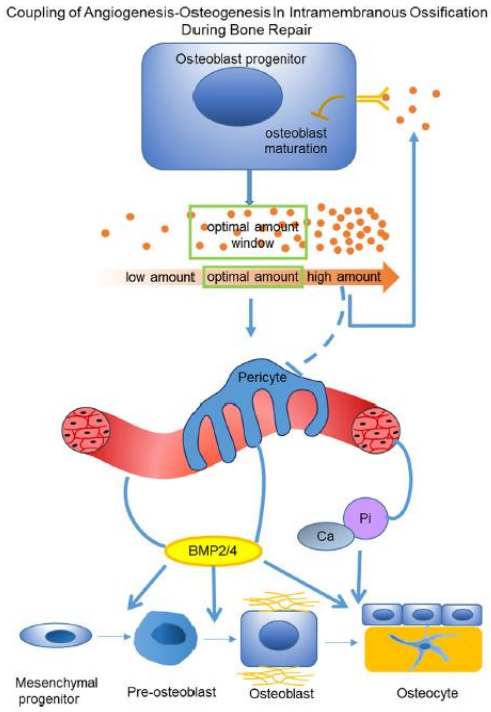

Figure 3.4 The role of VEGF in bone healing mediated by intramembranous oddification (Sun et al. 2016**)**

3.5 Mathematical models of bone healing and angiogenesis

In silico models can shed light on the fracture healing mechanism by testing and comparing various hypotheses on healing procedures. They can also promote the design of strategies for treatment of defective fracture healing. As a result, the cost of research is reduced.

However, fracture healing and angiogenesis are very complicated biological mechanisms that involve the activation of different cells and biochemical factors across different spatial and temporal scales (Carlier et al. 2012). Some biological events range from seconds, (phosphorylation mechanisms) to hours (mRNA transcription) to weeks (remodeling mechanisms, tissue formation). The spatial scales vary from nanometers (molecular level) to millimeters (tissue level) to meters (organism) (Liu et al. 2011, Meier-Schellersheim et al. 2009). As a result, these biological mechanisms are multiscale and must be modeled appropriately.

The approaches in modeling can be separated in two types: continuum and discrete modeling methods. Continuum models employ partial differential equations (PDEs) or ordinary differential equations (ODEs) in order to depict the evolution of tissue densities and cells. The model variables are average, so it is difficult to describe individual cell-matrix and cell-cell interactions (Wang et al. 2008, Thorne et al. 2007). As a result, it is difficult to simulate the individual intracellular mechanisms. Furthermore, continuum models cannot simulate correctly the angiogenesis mechanism because of the inherent discreteness of vascular networks (Zhang et al. 2009). Discrete methods are applied for the simulation of small-scale events (biological mechanisms at cellular and subcellular scales). However, these methods can turn computationally expensive when they are used for simulations of larger cell numbers at the tissue scale (Byrne et al. 2009).

Shefelbine et al. (2005)

The objective of this model was to conclude if intramembranous bone formation and remodeling during trabecular bone fracture healing could be simulated using the same mechanobiological fundamentals as those introduced for diaphyseal fracture healing. Finite element analysis and fuzzy logic for diaphyseal healing were used. The model simulated the forming of woven bone in the fracture gap and consecutive remodeling of the bone to create trabecular bone. It was also demonstrated that the trabecular structure depends on the applied loading conditions.

The fracture gap was modelled in trabecular bone using a micro-scale idealized cubic section (600μm a side) of the fracture gap residing of approximately 38,000 elements. It was modelled on the microscopic level in order to catch the microstructure of the trabeculae. The fracture gap's width was 500μm and was bordered by trabeculae spicules on both edges. The trabeculae adjacent the fracture gap was idealized as rectangular blocks four elements wide and three elements long, with a trabecular thickness of 100μm. The area between trabeculae and in the fracture gap was filled with elements of soft tissue to serve as marrow and the creation of the hematoma in the gap. Using ANSYS, finite element modeling and calculations were performed.

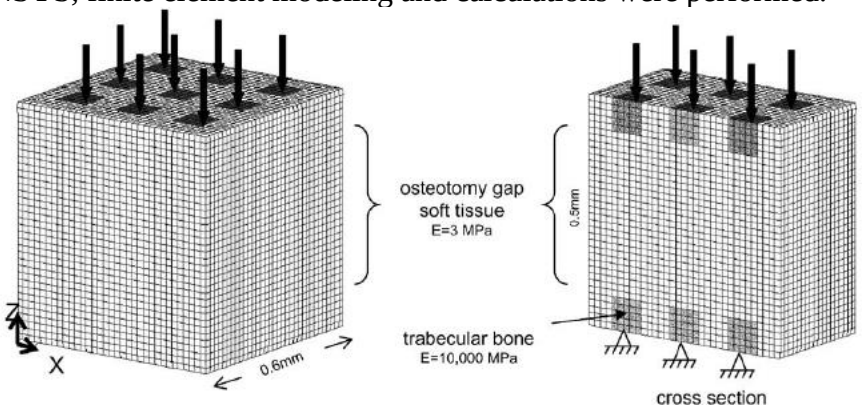

Figure 3.5 Finite element model of the osteotomy gap consisting of trabecular bone and soft tissue proposed by Shefelbine et al. The cross-section shows the trabecular spicules that surround the osteotomy gap (2005).

A fuzzy logic controller was used in order to determine tissue differentiation over time. It consisted of a set or 21 linguistic rules to characterize angiogenesis, tissue destruction, intramembranous and endochondral ossification and remodeling. Input from the finite element analysis was received by the fuzzy controller. Subsequently the fuzzy controller determined the location of the strain state on the tissue differentiation diagram, based on Claes and Heigele (1999), and decided what type of tissue to build. Additionally, to the strain rate, neighboring tissue properties and vascularity are also essential to tissue differentiation, therefore demanding the use of multiple rules and fuzzy logic.

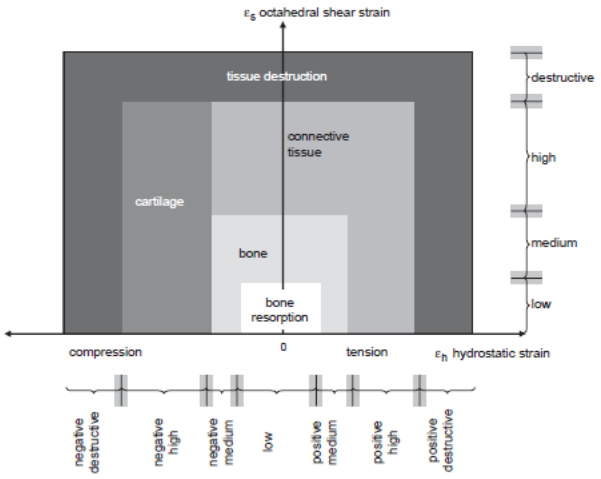

Figure 3.6 Tissue differentiation diagram proposed by Shefelbine et al. The boundaries between the areas are ranges rather that thresholds, making it "fuzzy" (2005).

Chen et al. (2009)

In this study, revascularization was described by two separate mechanisms: nutrition supply and angiogenesis. The mathematical models for nutrition supply and angiogenesis were proposed and combined into an existing fuzzy algorithm of fracture healing. The computational algorithm of fracture healing also consisted of stress analysis and tissue differentiation. It was tested on and compared with animal experimental results published previously.

The fuzzy logic rules were obtained from Shefelbine et al. (2005), with the vascularity replaced by the nutrient supply. However, a different method was used to establish the nutrition state of the tissues. As a result, the overall number of fuzzy logic rules were reduced. The start of the bone formation from the periosteal surface of the cortex was introduced as a supplementary condition. The nutrient supply, the mechanical stimuli, and the material compositions are input into the fuzzy logic controller and the changes of them are calculated.

The simulation results indicated that, for a small and medium-sized fracture gap, the nutrient supply was adequate for fracture healing. For a large-sized fracture gap, non-union may happen by insufficient mechanical conditions or defective nutrient supply. The comparisons with experimental results showed that the improved computational algorithm was capable to simulate abroad range of fracture healing cases and to predict and explain delayed unions and non-unions caused by different mechanical conditions and large gap sizes.

Geris et al. (2009)

The purpose of this study was to provide a mathematical framework in which both mechanical and biological factors in fracture healing are included. Biology and mechanics were connected by making certain parameters of a previously established bioregulatory model dependent on local mechanical stimuli.

Figure 3.7 shows an overview of the implementation of the connected mechanobioregulatory bone regeneration model. The first step of the analysis is a loading step. Based on the local mechanical stimuli obtained from a finite element analysis of the fracture zone, the parameters of the bioregulatory model were adapted

according to the scheme proposed by Bailon-Plaza and van der Meulen (2003) as shown in figure 3.7. Different parameter values (related to proliferation, angiogenesis, differentiation and matrix and growth factor production) were made dependent on different mechanical stimuli. In certain range of values of the mechanical stimulus, these processes were enhanced, whereas for stimuli outside this range, these processes were reduced.

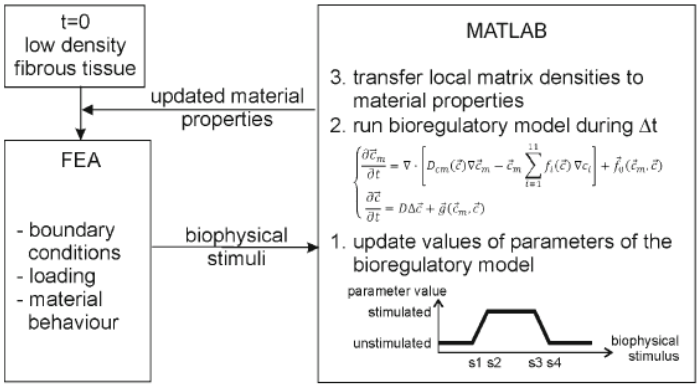

Figure 3.7 Overview of the implantation of the connected mechanobioregulatory model proposed by Geris et al. (2009).

Afterwards, the bioregulatory model is solved for a predefined time interval. The model expresses the change of several continuum type variables as a function of time and spatial coordinates. The continuum type variables include densities of fibroblasts, mesenchymal stem cells, osteoblasts and endothelial cells, chondrocytes, cartilage and bone extracellular matrix (ECM), fibrous tissue, generic chondrogenic, osteogenic and vascular growth factor concentrations. Mathematical expressions for the rate of cell proliferation, migration, differentiation, matrix synthesis and growth factor were defined and made dependent on growth factor concentration and/or local matrix density. The mathematical description of this model leads to a highly connected system of nonlinear partial differential equations (PDE).

Simulation results demonstrated that mechanics acting directly on angiogenesis alone were not able to predict the creation of overload-induced nonunions. However, the direct activity of mechanics on both osteogenesis and angiogenesis was capable to predict overload-induced nonunion creation. As a result, this confirmed the hypotheses of several experimental studies investigating the interdependence between osteogenesis and angiogenesis.

Anderson and Chaplain (1998)

The study presents continuous and discrete mathematical models which describe the creation of the capillary sprout network as a result of chemical stimuli (tumor angiogenesis factors) supplied by a solid tumor. The models also take into consideration crucial endothelial cell-extracellular matrix interactions. The continuous model has a system of nonlinear partial differential equations that describe the initial migratory response of endothelial cells to the tumor angiogenesis factors. Numerical simulations of the system, using parameters based on experimental studies. A discretized form of the partial differential equations was used to establish a biased random-walk model which is capable of tracking individual endothelial cells at the

sprout tips and incorporate anastomosis, mitosis and branching explicitly into the model.

Checa and Prendergast (2008)

In this study a discrete model was developed to simulate angiogenesis and incorporated into an algorithm for simulating tissue differentiation and regeneration. A regular 3D lattice with a separation between points of 0.01nm was used in order to simulate cell activity. The model takes into consideration: the formation of vessel sprouts from pre-existing sprouts or vessels, the growth of sprouts and the fusion of a sprout tip to another sprout tip or another sprout. The path of each capillary was determined by the path of the cells at the capillary tips which moved following a random walk with some directional bias towards higher concentration of growth factors (Terranova, 1985) and the tendency to persist in the same direction as that in its previous step (Stokes, 1991). It was assumed that sprouts only grow at their tips and that the rate of growth depends on the shear strain magnitude at the capillary tip.

To simulate the tissue regeneration process, a 3D stochastic model for cell migration and proliferation based on random walk theory (Perez, 2007) was combined with a mechano-regulation model for tissue differentiation (Prendergast, 1997). The role of blood vessel supply was also included in the model. The 3D simulation domain correlates to the gap tissue in a model of a bone/implant interface.

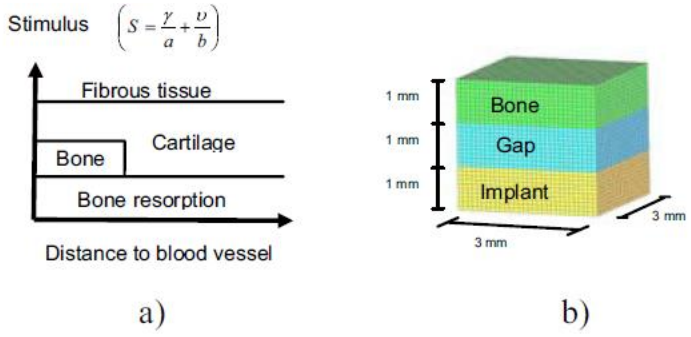

Figure 3.8 a) Mechano-regulation of stem cell fate, b) simple FE model to test simulations proposed by Checa and Prendergast (2008)

Sun et al. (2005)

A new deterministic mathematical formulation to model growth factor-induced angiogenesis was proposed. The replacement of traditionally used endothelial cell density by the capillary indicator function improves the capturing of the capillary network in a finer scale. Mechanisms such as sprout branching, anastomosis and cell proliferation are taken into consideration directly into the continuous mathematical model. Model parameters are modified to determine the strength of these mechanisms on angiogenesis. The model is fully deterministic and generates the overall structure of the capillary network. This structure is like those observed *in vivo*.

The forward Euler's method is used to solve the trajectory equation for the position of an individual sprout tip. The implicit cell center finite difference (CCFD) method is used to solve the diffusion-reaction equation for chemotactic growth factors concentration. The space is discretized using cell center finite differences and the time is discretized using the backward Euler's method.

Milde et al. (2008)

A 3D model of sprouting angiogenesis was presented that considers explicitly the effect of the extracellular matrix and of the soluble as well as matrix-bound growth factors on capillary growth. The computational model depends on a hybrid particle-mesh depiction of the blood vessels. It is introduced an implicit depiction of the vasculature that gives detailed depictions of nutrient transport.

A hybrid approach is used representing molecular species by their concentration and migrating endothelial cells' tip cells by particles. The evolution of molecular species is characterized by reaction-diffusion equations that are discretized on the grid while a particle approach is employed to model the migrating endothelial cells' tip cells. The endothelial density represents the newly formed capillaries. From the 3D representation of the vessels, a level-set approach can easily be used to create tubular structures capable of supporting blood flow. The extracellular matrix is modeled to consist of directed bundles of collagen fibers randomly distributed throughout the domain. A vector field that describes the fiber directions modulates the migration velocity of the endothelial cells in the presence of fibers.

Qutub and Popel (2009)

A multiscale model was introduced to simulate the processes underlying sprouting at the beginning of angiogenesis. The model uses logical rules to guide the action of individual ECs and segments of cells. It was designed by agent-based programming. The activation, motion and proliferation of ECs result in the capillary development in Ed. A new capillary network comes out of complicated cell-cell interactions. Parameters and rules are based on literature data from *in vitro* experiments with ECs. The model can predict tip cell activation, stalk cell formation and sprout development as a function of VEGF concentration.

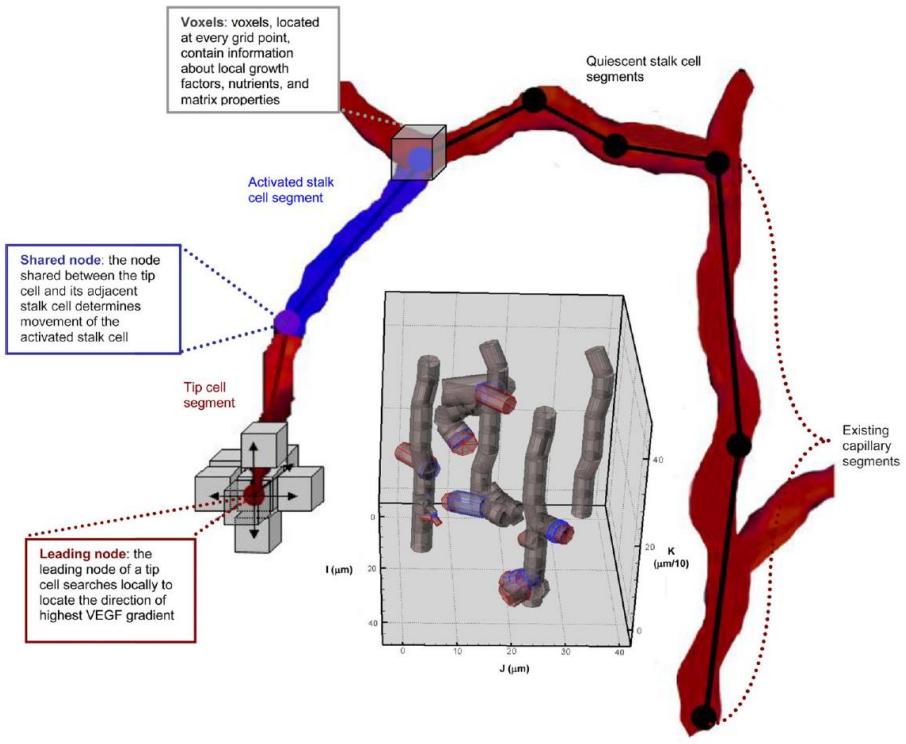

Figure 3.9 Schematic of the 3D model proposed by Qutub and Propel (2009). ECs represent capillaries. An example of a developing network with four capillaries is presented in the grey inset.

CHAPTER 4

ULTRASOUND EFFECT ON BONE FRACTURE HEALING

4.1 LIPUS and bone healing

Experimental evidence has shown that low-intensity pulsed ultrasound (LIPUS) causes significant osteoinductive effects, enhancing the healing of bone defects. Pulsed ultrasound treatment is simple, noninvasive, easy and relatively inexpensive. Studies have shown that ultrasound (US) treatment can reduce the time of bone fracture healing in humans (Heckman et al. 1994). Other studies have indicated that the intensity affects the therapeutic effect of US on bone (Nussbaum 1998). Bone fracture healing may also depend on the frequency of the US. In most studies a US frequency of 1.5 MHz is used, however few studies have investigated the effects of US at different frequencies on the fracture healing.

In intact bones, US energy rapidly attenuates at the soft-tissue interface. As a result, US may only influence cells on the periosteal surface and in the outer layers of the bone cortex (Warden et al. 2001). When a bone is fractured, the integrity of the bone cortex is lost. As a result, the effect at the soft tissue-bone interface is reduced. Therefore, US effects might have a greater chance to affect bone formation through the fracture gap by thermal or non-thermal effects.

Figure 4.1 Commercially available LIPUS device used for fracture healing (Exogen 4000+, Smith & Nephew, Inc., Memphis TN, USA)

Historical background of US treatment

Butchala (1950) first suggested that US might enhance osteogenesis. Maintz (1950) investigated the relationship between bone healing and high intensity US. He reported that rabbit radial fractures showed small changes after US (500 mW/cm^2) was applied, but callus formation was reduced using higher intensities (1000, 1500, 2500 mW/cm^2). Bender et al. (1954), Herrick et al. (1956) and Ardan et al. (1957) reported delayed bone healing and dense fibrous tissue formation in dog femora using very high US intensities. De Nunno (1952) and Corradi and Cozzolino (1953) indicated that high US intensity (200-3000 mW/cm^2) increases callus formation and enhances healing in rabbit radii. Chang et al. (2002) reported a 36% increase in new bone formation and an 80% increase in torsional stiffness of limbs treated with high intensity US (500 mW/cm^2). The mixed results using high intensity US led many to start pulsating the source of the sound head itself or decreasing the output of the US generator. Duarte (1983) developed the use of LIPUS clinically to enhance osteogenesis.

Non-thermal mechanisms

US produces a combination of nonthermal effects: displacement, acoustic streaming and cavitation. Acoustic streaming is defined as the physical forces of the sound waves that provide a driving force capable of displacing ions and small molecules. Organelles and molecules have different molecular weights. Many of these are motionless, but many are freely floating and may move around more stable structures. This mechanical pressure caused by the wave produces unidirectional movement of fluid along and around cell membranes.

Acoustic streaming is associated with transfer of momentum to the fluid. As a result, nutrients redistribute in the culture medium *in vitro* and perturbate the local homeostasis, triggering biological responses. The wave propagation through the highly porous network of mineralized and soft tissues in the fracture callus may stimulate fluid microenvironment in the pores. When acoustic streaming creates fluid flow, the extracellular matrix can be modulated, and shear stress can be applied activating mechanoreceptors on the cell membranes.

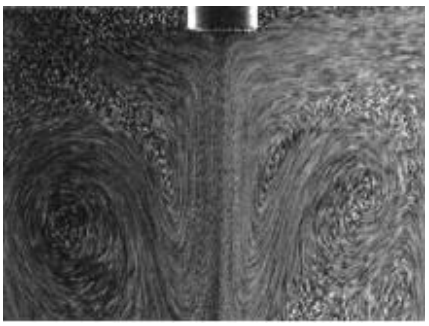

Figure 4.2 Acoustic streaming, visualized by ten superimposed images taken at 200 ms intervals of corn starch particles in the field of a 32-MHz plane transducer (Iwabuchi et al. 2005)

Displacement occurs when LIPUS waves move both fractural ends. The scale of this motion is debated. Claes and Willie (2008) suggested that this motion occurs on a microscopic scale i.e., 0.5-2mm, while Pounder and Harrison (2008) proposed that the motion takes place in nanometric scale i.e., 0.15-0.55nm.

Cavitation is defined as the physical forces of the sound waves on microenvironmental gases within fluid. As the sound waves propagate through the medium, the characteristic compression and rarefaction causes microscopic gas bubbles in the tissue fluid to contract and expand. It has been proposed that the rapid changes in pressure, both in and around the cell, may cause damage to the cell. Substantial injury to the cell can occur when microscopic gas bubbles expand and then collapse rapidly, causing an unstable cavitation. In therapeutic levels of US, this phenomenon is not expected to occur. However, pulsation of gas bubbles can alter the function of the cell due to disruption of cellular activity. It has been suggested that the US at the beginning “injures” the cell and as a result the growth decelerates. Afterwards, the cellular recovery begins, with the characteristic of an increase in protein production.

Thermal mechanisms

Whenever US energy is propagated into a tissue, the amplitude of the wave decreases with distance. This attenuation is due to either absorption or scattering. Absorption occurs when a portion of the wave energy is converted into heat. Scattering is that portion which changes direction. The medium can absorb energy to produce heat and as a result, a temperature increase may occur if the rate at which heat is produced is greater than the rate at which the heat is removed. This temperature increase depends on US parameters and tissue properties. Reported thermal effects include decreased muscle spasm, augmented extensibility of collagenous tissues and increased blood flow. This increase of temperature can be adequate to regulate thermo-sensitive enzymes like metalloproteinase, which has 3-fold reaction rate increase per each 2^{o} raise and are essential for bone matrix remodeling.

Intracellular effects

Direct mechanical effect of the US on cell membranes or proteins can trigger a biological response. When US with intensity between 1 and 2 W/cm^2 is applied, the very low strains caused by US on cells *in vitro* have been shown to stimulate a prompt fluidization of the cytoskeleton resulting in augmented cytoskeletal remodeling (Mizrahi et al. 2012). These mechanisms may contribute to the bioeffects of LIPUS.

Another proposed mechanism of pulsed US is the hypothesis of relative oscillatory displacement between intracellular elements of different densities, such as cell nucleus, and the structure in which they are placed. Or and Kimmel (2009) suggested that LIPUS can trigger cyclic intracellular displacements comparable with, and even larger that, the mean thermal fluctuations, with resonance frequencies in the range of direct oscillatory movement caused by US wave or by the acoustic radiation pressure. The 'bilayer sonophore' model proposed by Krasovitski et al. (2011), describes a mechanism where the intramembranous hydrophobic space between the two monolayer leaflets inflates and deflates periodically when exposed to US, being pulled apart by the negative pressure of a US cycle, and pushed back together by the positive pressure. The main hypothesis is that negative acoustic pressures are large enough to overcome molecular attractive forces of the two leaflets of the cell membrane.

Louw et al. proposed a mathematical model was proposed to predict US-stimulated intracellular stresses and strain, using a biphasic description of the cells in a harmonic standing wave field. It has been reported that strain and stresses are maximized within the cell at two distinct frequencies, which are cell-type dependent through the mechanical and geometric characteristics of its different components. Dilatational deformation induces stresses gradients. As a result, a net force acts on the nucleus and may cause transduction by the nucleus and leads to load-inducible gene expression. Therefore, when excitation frequency matches the cell resonant frequency, stimulated load-inducible gene expression should be maximized.

Molecular effects

US can interact with molecules. Lipids and structures in the cell membranes show an absorption behavior for US, probably linked to relaxation phenomena. In large unilamellar vehicles, these relaxation phenomena are linked to the interaction of US with the hydrophobic side chains, causing a structural reorganization of small domains of molecules (Morse et al. 1999). These interactions can influence the biological

function of molecules. At very high intensities, US can harm biological molecules, such as the DNA degradation, but these intensities are not used in US treatment. It has been reported that US could disrupt multimolecular complexes (Johns 2002). For example, when LIPUS was applied on bone cells, the cytoskeleton was fluidized (Mizrhahi et al. 2012). This may be due to a change of protein conformation. The cause of these phenomena could be due to the local strains induced by US that were large enough to disrupt weak nonspecific bonds, changing protein conformation and causing structural remodeling of the cytoskeleton.

4.2 Effects of LIPUS on cells

Effects on the cells in the inflammatory response

Previous *in vivo* studies have shown that US was more effective in the inflammation and proliferation phase, but not remodeling phase (Spadaro and Albanese 1998, Wang et al. 1994, Yang et al. 1996). Several reports have demonstrated that US affects cells that are essential in the immune response. US has been shown to affect endothelium, macrophage, production of growth factors, angiogenesis, fibroblasts, osteoblasts, proliferation of T-cells, and interleukines.

An intensity range of 5 to 100 mW/cm^2 increases the production of Interleukin-1 and Interleukin-8 (Reher et al. 1997), vascular endothelial growth factor (Rawool et al. 2003, Wang et al. 2004), fibroblast growth factor-b, and collagen (Gaul 1999). The bone healing was promoted, and thrombolysis was accelerated. Kumagai et al. (2012) reported that local osteoprogenitors and osteogenic precursors of systemic circulation were recruited to the fracture region in mice *in vivo* model after LIPUS application. LIIPUS also increases prostaglandin E_2 production, which is a potent inflammation mediator that may enhance proliferation and migration of mesenchymal stem cells (Kokubu et al. 1999).

Effects on angiogenesis

LIPUS up-regulates IL-8 secretion by human osteoblasts (Doan et al. 1999) and gene expression in murine pre-osteoblasts (Bandow et al. 2007). IL-8 induces endothelial cells migration and proliferation, which are essential for angiogenesis during fracture healing. LIPUS also enhances VEGF production in human osteoblasts and human peripheral blood monocytes (Doan et al. 1999). Leung et al. (2004) showed that LIPUS stimulation increased VEGF expression *in vivo* compared to untreated media.

Basic fibroblast growth factor (bFGF) has been reported to be up-regulated by LIPUS application in human osteoblasts. bFGF stimulates fracture healing through an unknown process by enhancing migration and mitogenesis of osteoblasts and MSCs. After LIPUS exposure, co-cultures of human osteoblasts and human umblilical vein endothelial cells showed higher levels of platelet-derived growth factor (PDGF) (Ito et al. 2000). PDGF is a mitogenic factor for MSCs and fibroblasts.

Effects on bone cells

LIPUS has been shown to incite the osteogenic differentiation in vitro (Erdogan et al. 2006). Osteogenic cells are affected by LIPUS stimulation (Leskinen et al. 2008).

As a result, mineralization is enhanced, collagen production is increased, and osteoblasts are stimulated.

Angle et al. (2011) showed that LIPUS intensities lower that current clinical standards enhance osteogenic differentiation of rat bone marrow stromal cells. Leung et al. (2004) showed LIPUS application on periosteal cells could differentiate along an osteogenic pathway, resulting in augmented mineralization. As a result, a few osteogenic markers were increased. After four weeks of LIPUS treatment the cultures showed a four-fold increase in mineralization compared with untreated controls. It is hypothesized that LIPUS enhances mineralization by enhancing the maturation of extracellular matrix facilitating the mineralization of the fracture callus (Saito et al. 2004).

Korstjens et al. (2004) used mouse metatarsal rudiments stimulated by LIPUS. Augmented growth of the ossifying zone was reported, compared with control rudiments. LIPUS did not affect the length of these rudiments. As a result, LIPUS may enhance endochondral ossification.

LIPUS application on fetal mouse metatarsal rudiments *in vitro* has a direct effect on ossifying tissue and osteoblasts by stimulating differentiation and/or cell activity, but not proliferation (Nolte et al. 2004). Other studies have reported that LIPUS enhances the endochondral ossification in an *ex vivo* model of fetal mouse metatarsal. It has been hypothesized that the acceleration of callus mineralization increases mechanical strength.

Study (reference)	**Type of Study**	**f (MHz)**	**I (mW/cm^2)**	**P.R.R. (kHz)**	**D.C. %**	**Results**
Chen et al., 2014	murine preosteoblast cell line	1	100	1	20	LIPUS could adjust the proliferation, differentiation, and mineralization of osteoblasts.
Fung et al., 2014	murine osteocyte-like cell line	1.5	30	-	-	US stimulated osteocytes.
Tabuchi et al., 2013	mouse preosteoblast cell line	1.5	30	1	-	Results provide to the understanding the molecular basis of the processes of the LIPUS response in osteoblast cells.
Li et al., 2012	osteocytic cell line	1.5	-	-	-	LIPUS affects proliferation and differentiation of osteoblasts & osteocytes in *vitro*.
Wu et al., 2009	normal human osteoblast cell line	1.0	30	-	-	LIPUS enhanced osteogenesis in an osteoporotic rat model.
Tang et al., 2007	a murine osteoblastic cell line	1.5	30	1	20	LIPUS application regulates genes expression in osteoblasts.

Bandow et al., 2007	a mouse osteoblastic cell line	1.5	30	1	-	LIPUS activates osteoblasts to express some chemokines.
Maddi et al., 2006	human osteoblast cell line	0.045	30	-	-	US may enhance bone regeneration.
Naruse et al., 2003	osteocytes derived from newborn rat bones	1.5	-	-	-	LIPUS cause distraction osteogenesis that depends on the stimulation of osteoblasts.
Warden et al., 2001	bone-forming cells	1	30	1	-	Ultrasound stimulates expression of some related genes and elevates mRNA levels of ALP and OC that are proteins of the bone matrix.

Table 4.1. Effect of LIPUS alone *in vitro* on fracture healing in animal models (M. Bayat et al, 2018)**.**

Effects on chondrogenesis

Studies have indicated that US application could accelerate chondrogenesis (Ebisawa et al. 2004). Uddin and Qin (2013) revealed that LIPUS application can restore the normal osteogenic differentiation of MSCs. Zhang et al. (2003) applied US *in vitro* to chondrocytes and reported that there was an enhancement in the expression of type X collagen. LIPUS has been reported to augment the differentiation of marrow-derived cells (Naruse et al. 2003) and chondrocytes isolated from rat cartilage (Parvizi et al. 1999).

Lee et al. (2006) reported that LIPUS exposure enhances the expression of chondrogenic markers in rabbit MSCs. Schuman et al. (2006) showed that when LIPUS was applied on MSCs, they had more pronounced chondrogenic phenotype, expressing higher chondrogenic markers. Other studies indicate that LIPUS promoted differentiation of pig and rat primary chondrocytes (Takeutchi et al. 2008, Kobayashi et al. 2009). Several studies have indicated that LIPUS exposure enhances proliferation of chondrocytes from human, rat and pig nucleus pulposus cell line (Takeutchi et al. 2008, Kobayashi et al. 2009, Mukai et al. 2005).

Effects on bone remodeling

Several studies have shown that US application enhances expression of maturing osteoblasts markers and calcium deposition (Angle et al. 2011, Suzuki et al. 2009). Osteoblasts express receptor activator of NF-κB ligand (RANKL) and osteoprotegerin (OPG) proteins. They regulate the function of osteoclasts. RANKL activates osteoclasts and OPG antagonizes its action by binding to the RANK expressed on osteoclasts. LIPUS peaked RANKL gene expression at the third week of LIPUS exposure in differentiating murine osteoblasts, while it was only slightly up-regulated during first, second and fourth weeks. However, OPG expression remained the same throughout three weeks of LIPUS treatment. This indicates that LIPUS may enhances osteoclastogenesis throughout the bone regeneration, peaking on week three, which corresponds to woven bone resorption and lamellar bone formation in mice.

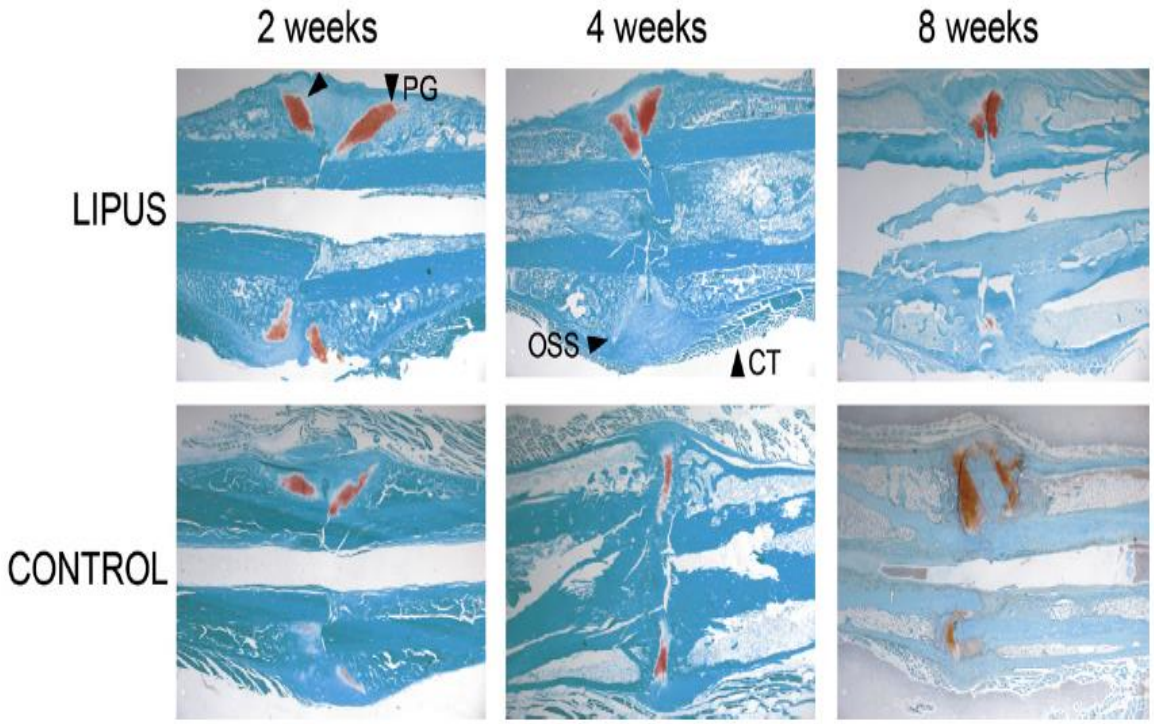

Figure 4.3 Qualitative histology of osteoporotic fracture site in the LIPUS and control groups. At week 2, the LIPUS group shows higher content in cartilage (PG, proteoglycan signal). At week 4, the LIPUS group continued to show higher content of cartilage, calcified tissue also increased (arrows) (OSS, site of endochondral ossification; CT, calcified tissue). At week 8, the LIPUS group showed faster decrease in the amounts of cartilage compared with cartilage amounts in the control group beginning to increase (Cheung et al. 2011).

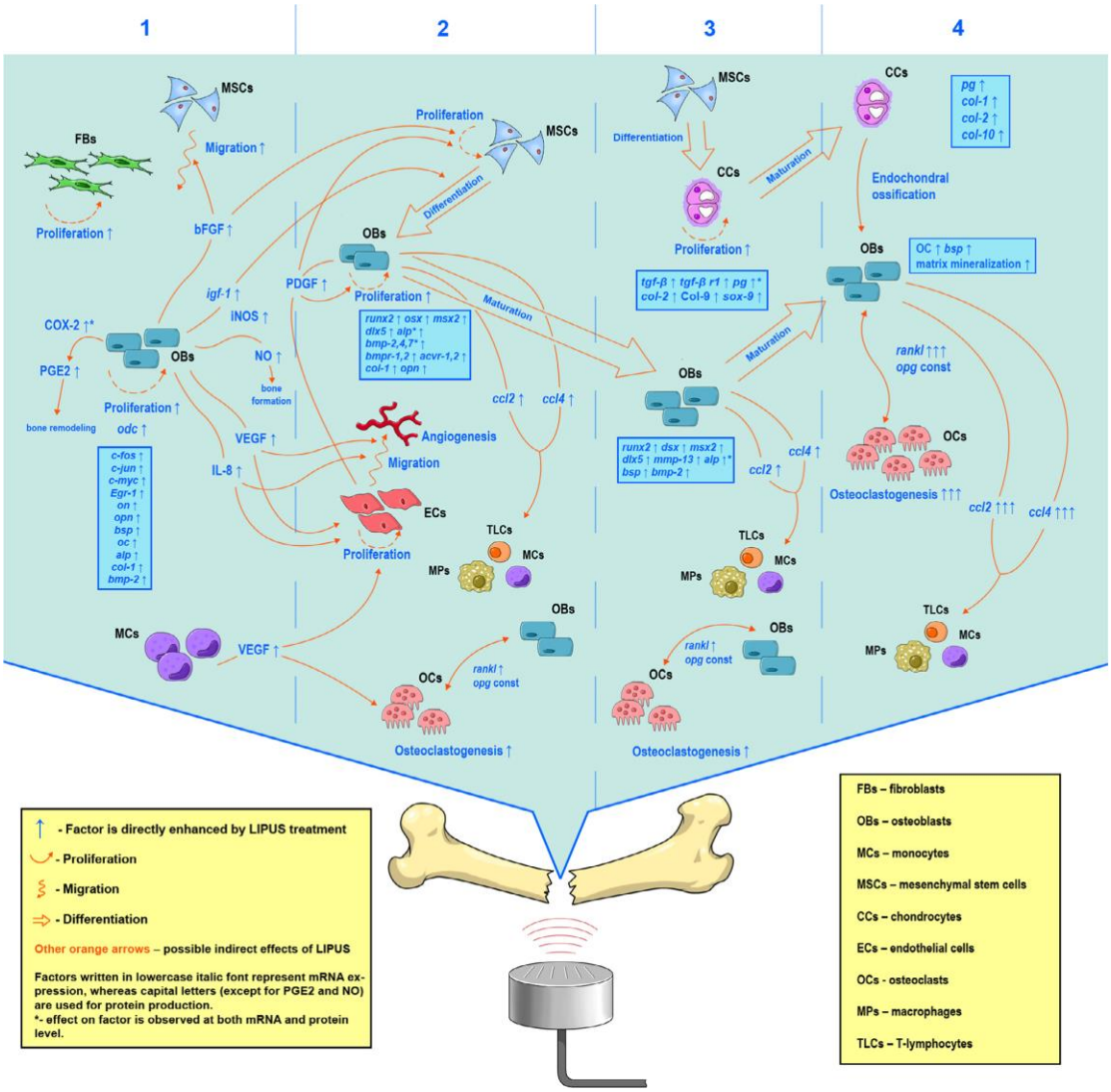

Figure 4.4 Summary of hypothetical LIPUS effects on cellular events from published in-vitro data. The columns represent the four phases during in-vivo endochondral bone fracture healing. Phase 1: processes after the bone fracture: hematoma formation, inflammation and migration of osteogenic precursors.
Phase 2: angiogenesis, proliferation of MSCs and osteoblasts and osteogenic differentiation.
Phase 3: chondrogenesis and maturation of osteoblasts.
Phase 4: maturation of chondrocytes, woven bone formation and remodeling (Padilla et al. 2014).

4.3 Experimental studies

Animal studies

Study (reference)	**Animal &defect**	**f (MHz) & I mW/cm^2**	**P.R.R. (kHz) & D.C. %**	**Main results/Conclusions**
Fontes-Pereira 2016	Rat, a fracture was induced in tibia	1 MHz, 40 W/cm^2	100Hz 20%	There was no significant between-group

				differences in bone-healing processes.
Fung, 2014	Rat, a fracture was induced in femur & was supported with Internal fixation (IF)	1.5 MHz, 30 mW/cm^2	1kHz	The effect of LIPUS depends on the axial distance of the ultrasound beam.
Pomini, 2014	Rat, a unilateral partial fracture of fibula was made	1 MHz, 0.5 W/cm^2	20%	LIPUS can enhance fractures.
Fung, 2012	Rat, a fracture was induced in femur & was supported with IF	1 MHz, Group 1: 30 mW/cm^2 Group 2: 150 mW/cm^2	1kHz 20%	LIPUS at $I_{(SATA)}$150 mW/cm^2 did not cause any enhancement of the fracture healing.
Katano, 2011	Mice, a fracture was made in femur & was supported with IF	-	-	LIPUS causes endothelial cell migration and neovascularization during fracture healing.
Naruse, 2010	Mice, a fracture was induced in femur & was supported with IF	1.5 MHz, 30 mW/cm^2	1kHz	LIPUS dropped to half the endochondral phase in middle-aged mice.
Shakouri, 2010	Rabbit, open osteotomies were made and were stabilized with external fixators (EF)	1.5 MHz, 30 mW/cm^2	1kHz	LIPUS stimulates callus MD and strength of the fractured bone increases insignificantly.
Ramli, 2009	a fertilized egg	Short: 1MHz Long: 45 kHz	Short: 0.1-1.0 W/cm^2 Long: 5-50 mW/cm^2	US can cause neoangiogenesis *in vivo*.
Warden, 2006	Rat, bilateral femural fractures were induced and stabilized with IF	100Hz	100 Hz	No differences between fracture healing treated with ultrasound and no ultrasound.
Sakurakichi, 2004	Rabbit, osteotomy was made in tibia & were stabilized	1kHz	1kHz	LIPUS affect the endochondral pathways.

	with EF & distraction osteogenesis (DO) were done			
Hantes, 2004	Sheep, an osteotomy was made in tibia and was stabilized with an EF	1 MHz, 30 W/cm^2	1kHz	LIPUS can enhance the fracture-healing process.
Heybeli, 2002	Rat, femural osteotomy was made & defect was stabilized with IF	7.5 MHz, 11.8 W/cm^2	1Hz	Diagnostic sonographic device accelerates fracture healing.
Mayr, 2001	Sheep, an osteotomy was done in metatarsus & callus distraction was performed	1.5 MHz, 30 mW/cm^2	1kHz	LIPUS enhances fracture healing.
Azuma, 2001	Rat, femural osteotomy was made & defect was stabilized with IF	1.5 MHz, 30 mW/cm^2	1kHz	LIPUS affects cellular mechanisms in each phase of the healing procedure.
Shimazaki, 2000	Rabbit, open osteotomy was made in tibia & was stabilized with EF & DO were done	1.5 MHz, 30 mW/cm^2	1kHz	LIPUS enhances bone maturation, even in cases of poor callotasis.
Wang, 1994	Bilateral femoral fractures were made & defect was stabilized with IF	1.5 or o.5 MHz, 30 mW/cm^2	1kHz	LIPUS with frequency of 0.5 or 1.5 MHz enhances fracture healing.
Pilla, 1990	Rabbit, bilateral fibular osteotomy was performed	1.5 MHz, 30 mW/cm^2	1kHz	LIPUS enhances biomechanical healing.

Table 4.2 Effect of LIPUS alone on fracture healing in animal models (Bayat et al. 2018)

Clinical trials

Nonunion is a state in which a fracture is not healed within the expected time and where a fracture will not heal without intervention. Xavier and Duante (1983) reported that after brief exposure (20 min/day) to LIPUS (30mW/cm^2) of 26 nonunions, 70% of them were healed. Mayr et al. (1997) reported that 88% and 93% in a group of 29 patients with delayed unions and unions respectively had been healed, with LIPUS application. Nolte et al. (2001) reported an 86% healing rate in a study of 29 unions. LIPUS was the only treatment after surgery. Gebauer et al. (2000) evaluated the effectiveness of LIPUS in a group of patients with 67 long-lasting unions. 66% of the nonunions were healed after approximately 6 months after the beginning of US application. These studies indicate that LIPUS enhances healing in nonunions.

Nolte et al. (2008) obtained biopsies from 13 patients with a delayed union of the osteotomized fibula. They were treated for 2-4 months with or without LIPUS. Histomorphometrical analysis was used to examine bone resorption parameters, angiogenesis and bone formation. When LIPUS was applicated, endosteal callus was formed by direct bone formation without a cartilage intermediate. Indirect bone formation was also reported. In untreated control group, only indirect bone formation was reported. In new bone formation region, LIPUS enhanced bone volume by 33%, mineral apposition rate by 27% and osteoid thickness by 47%. The increase of osteoid thickness is a result of increased osteoid apposition. This indicates that LIPUS has an anabolic effect on osteoblasts. However, no increase in the number of blood vessels was reported in the newly formed bony callus. Cancellous bone volume was increased by 17%, but no effect was reported on mineral apposition rate and osteoid maturation time.

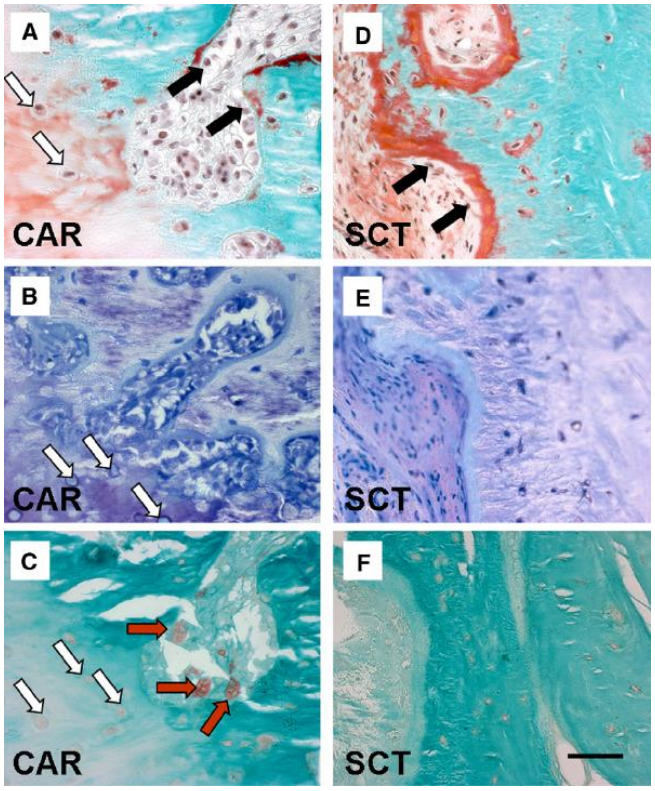

Figure 4.5 Histological sections of delayed unions of the human fibula treated with or without LIPUS showing differences in type of bone formation in the area of new bone formation.
(A, B, C) Consecutive sections of an untreated control biopsy showing endochondral ossification. (A) Newly formed woven bone replaces the cartilage matrix (CAR) at the fracture end. Osteoblasts deposit osteoid at the woven bone surface (black arrows). (B) The cartilage matrix adjacent the fracture end contains high numbers of hypertrophic chondrocytes (white arrows). (C) TRAP-positive osteoclast-like cells (red arrows) resorb the mineralized cartilage matrix.
(D, E, F) Consecutive sections of a LIPUS-treated delayed union showing direct (intramembranous) bone formation. (D) Osteoblasts (black arrows) located in the soft connective tissue (SCT), deposit osteoid at the woven bone surface. (E) Cartilage tissue with hypertrophic chondrocytes is absent adjacent the fracture end. (F) TRAP-positive osteoclast-like cells are absent (Rutten et al. 2008).

Study (reference)	Animal &defect	f (MHz) & I (mW/cm^2)	P.R.R. (kHz) & D.C. %	Main results/Conclusions
Lee, 2016	Ununited femoral neck fracture of 2 patients	-	-	LIPUS can be a possible treatment for delayed union & non-union of femoral neck fractures.
Moghaddam, 2016	Long bone nonunions	1.5 MHz, 30 mW/cm^2	1 kHz	LIPUS does not enhance long bone nonunions.
Nolte, 2016	Metatarsal fractures	-	-	LIPUS-treated patients had a significantly better heal rate.
Biglari, 2016	Long bone nonunions	1.5 MHz 30 mW/cm^2	1 kHz	LIPUS delayed the time of treatment.
Zura, 2015a	Chronic (>1 year) fracture nonunion	EXOGEN		LIPUS accelerates healing of nonunion fractures.
Carlson, 2015	Scaphoid Fracture Nonunions in Adolescents in adolescent patients	1.5 MHz, 30mW/cm^2		LIPUS can enhance scaphoid healing.
Farkash, 2015	Delayed union scaphoid fractures	1.5 MHz, 30mW/cm^2	1 kHz	LIPUS can help heal delayed union scaphoid fractures.
Zura, 2015b	Fresh fracture	Exogen device		LIPUS had a 96% HR.
Liu, 2014	Fractures of the distal radius	1.5 MHz, 30mW/cm^2		LIPUS group reduced fracture healing time.
Watanabe, 2013	Delayed unions and nonunions	1.5 MHz, 30mW/cm^2	1 kHz	LIPUS can be used as an adjuvant therapy in combination with surgery.
Hemery, 2011	Non-union fractures	Exogen® stimulator		Ultrasound is effective in enhancing healing for non-union.
Schofer, 2010	Delayed unions of the tib	1.5 MHz, 30mW/cm^2	1 kHz	LIPUS significantly accelerated bone repair in group compared to no LIPUS application.
Rutten, 2009	Delayed clinical fracture healing	1.5 MHz, 30mW/cm^2	1 kHz	LIPUS does not increase osteogenic cell number, but possibly affects osteogenic cell differentiation.

Rutten, 2008	Delayed union of the osteotomized fibula	1.5 MHz, 30mW/cm^2	1 kHz	LIPUS enhances fracture healing of delayed unions.
Yadav, 2008	Tibial stress fractures	-	-	Ultrasound treatment can accelerate stress fracture.
Lubbert, 2008	Fresh clavicle fractures	1.5 MHz, 30mW/cm^2	1 kHz	LIPUS does not enhance healing duration of fresh clavicle shaft fractures.
Jingushi, 2007	Postoperative delayed union or nonunion of long bone fractures	1.5 MHz, 30mW/cm^2	1 kHz	In long bone fractures, the union rate was 75%.
Handolin, 2005	Lateral malleolar fractures that were fixed with a bioabsorbable screw	1.5 MHz, 30mW/cm^2	1 kHz	No significant difference in bone mineral density between the ultrasound and non-ultrasound group.
Leung, 2004	Complex tibial fracture	1.5 MHz, 30mW/cm^2	1 kHz	LIPUS treated delayed-union cases.
Mayr, 2000	Nonunion fractures	1.5 MHz, 30mW/cm^2	1 kHz	LIPUS could be used as a nonoperative treatment of great potential for bone disorders.
Basso, 1998	Wrist fracture	46.39 MHz, 30mW/cm^2		There was no significant difference in wrist motion and duration of follow-up between the treated and control patients.
Heckman, 1994	Tibial fracture-healing	1.5 MHz, 30mW/cm^2	1 kHz	LIPUS enhances the normal fracture-repair process.

Table 4.3 Effect of LIPUS on fracture healing in patients (Bayat et al. 2018)

Effects on mechanical properties of the bone

Pilla et al. (1990) reported that after LIPUS application on a fibula osteotomy model there was an increase in torsional strength in rat bone fracture models. Several enhanced biological procedures may be responsible of this increase, such as a more rapid formation of the matrix due increase of growth factors in the local environment, the augmented mineralization of the matrix by enzymes involved in the calcification procedure and a more organized matrix laid down at the fracture area. Two enzymes implicated in the process of converting the soft collagenous callus to hard fracture callus are MMP-13 and alkaline phosphate.

Azuma et al. (2001) showed that in an *in vivo* rat model of fracture repair, application of LIPUS at the early, mid or late stages of fracture repair caused an increased torsional strength over control untreated fractures. Yang et al. (1996) reported an increased maximum torque and a slightly decreased torsional stiffness using 50 mW/cm^2 compared to 100 mW/cm^2. Wang et al. (1994) showed that there was no significant difference in maximum torque or torsional stiffness in rat femora with LIPUS intensity of 30 mW/cm^2 stimulation with a frequency of 0.5 Hz compared to 1.5 Hz. Both frequencies enhanced maximum torque and torsional stiffness.

4.4 Parameters of LIPUS stimulation

Intensity

In order to enhance tissue healing, US should be used in the range of 0.1-0.5 W/cm^2. Any intensity lower that 0.1 W/cm^2 did not show any benefit (Al-Karmi 1994). When US was applied on metatarsal long bone rudiments of fecal mice, for 5 minutes at 0.15 W/cm^2, proliferation in cartilage was stimulated (Witlink et al. 1995). Heybeli et al. (2002) reported that US treatment with intensity of 11.8 mW/cm^2 enhanced fracture healing and bone density in rat femora. Min et al. (2006) reported that the most effective application of LIPUS was at an intensity of 200mW/cm^2 for soft tissue. According to Iwanabe et al. (2016) the gap closure took place earlier at 160mW/cm^2 *in vitro* compared with 240 mW/cm^2 .

Fung et al. (2012) used femoral fractured Sprague-Dawley rats and divided that into three groups: control, LIPUS-30 (30 mW/cm^2) and LIPUS-150 (150 mW/cm^2). Weekly endpoint microCT, radiographs, biological tests and histomorphometry were performed. The results indicated that LIPUS-30 induced higher woven bone percentage, higher low-density bone volume fraction and failure torque than control group and LIPUS-150. Reher et al. (1997) also reported that the production of bone matrix by house calvaria bone was reduced when the intensity was higher than 100 mW/cm^2.

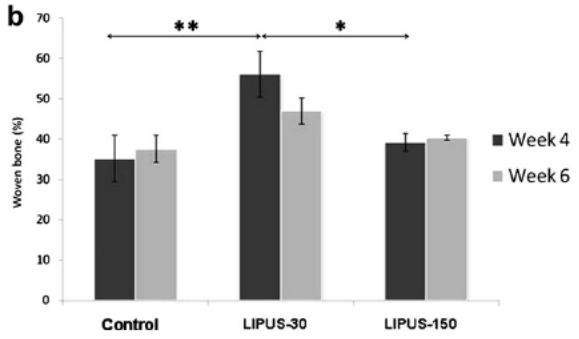

Figure 4.6 Quantitative histologic woven bone percentage results compared at week 4 and 6. LIPUS-30 was significantly higher than control and LIPUS-150 in week 4 (Fung et al. 2012).

Several reports have indicated that intensity of 30 mW/cm^2 can enhance fracture healing and this US setting has been approved by FDA in treatments of nonunions and fresh fractures. Wang et al. (1994) showed that 30 mW/cm^2 intensity can enhance stiffness and maximum torque.

Angle et al. (2010) applied US with three intensities: 2, 15 and 30 mW/cm^2 on rat bone marrow stromal cells. They reported that 2 mW/cm^2 induced the highest increase in mineralization among other intensity groups.

Frequency

To investigate the effects of frequency of LIPUS on bone and particularly on mandibular bone defects in a rabbit model, Bronoosh et al. used 56 adult Dutch rabbits. They were divided randomly into control, LIPUS-1 (1MHz), and LIPUS-3 (3 MHz) groups. A mandibular defect was created in all rabbits. The effect of LIPUS was assessed by frequency (1 or 3 MHz) and timing (2 and 4 weeks). Bone density, histology, and stereology were measured and were compared at the end of 2 and 4 weeks. LIPUS-3 caused a significantly higher bone formation compared to the control group at the end of week 4. Bone density was also higher at the end of week 4 that week 2. LIPUS-3 also increased the numerical density of osteoblasts and osteocytes at the end of week 4. However, LIPUS-1 did not enhance the healing process. This may happen due to loss of integrity of bone cortex in the defect area. It was demonstrated that the rate of bone formation in the defect depends on the frequency and the period of application of LIPUS.

Lai et al. (2011) tested the effects of US at different frequencies on fracture healing over three weeks in a rabbit fibular fracture model. 45 adult New Zealand White rabbits were divided into five groups: a control group and four groups for US frequencies: 0.5, 1.0, 1.5, and 2.0 MHz. The four groups that had been treated with US had greater new bone formation and torsional stiffness of the fibula that the control group. However, between the groups that had been treated with US there was no significant difference. However, Dyson and Brooks et al. (1983) and Wanh et al. (1994) found that 1.5MHz was the most efficient in enhancing the bone healing. Tsai et al. (1992) reported significantly greater mineral apposition rates with US stimulation of 1.5 MHz compared to 3 MHz. Frequency of 1.5 MHz is commonly used to enhance osteogenesis in experiments and clinical trials.

Percentage of duty cycle

The percentage of duty cycle affects the US dosage delivery. LIPUS (duty cycle <100%) with low intensity mostly induces nonthermal effects on tissues. Greenleaf et al. (2003) reported that after LIPUS application, there was a motion in nanometer scale in osteotomized radius of cadaver. *In vitro* experiments have shown that this mechanical signal might be further transduced by some cellular biochemical reactions, such as cytoskeleton modifications (Hauser et al. 2009), signaling pathways (Olkku et al. 2010) and activation of integrin intracellular signaling (Zhou et al. 2004).

Time and duration

Sant' Anna et al. (2005) found that an increase in gene expression was the greatest after 3 days of exposure to US. Neupmann Feres et al. (2016) showed that LIPUS application enhances the osteoclast's activity. When daily application time was doubled (from 10 minutes to 20 minutes per day) the resorption rate was increased. Cheung et al. (2010) used LIPUS on fractured rats and reported that healing began earlier (5-6 weeks after the fracture) that the control group (7-8 weeks after the fracture). Callus formation was increased with LIPUS application.

CHAPTER 5

NUMERICAL SIMULATION OF ULTRASOUND EFFECT THROUGH A BIOLOGICAL MODEL

5.1 The computational multiscale model

The base is the model introduced by Peiffer et al. (2011) which has eleven differential equations describing the spatiotemporal variation of mesenchymal stem cells (c_m), fibroblasts (c_f), chondrocytes (c_c), osteoblasts (c_b), fibrous extracellular matrix (m_f), cartilaginous extracellular matrix (m_c), bone extracellular matrix (m_b), generic osteogenic (g_b), chondrogenic (g_c), vascular growth factors (g_v), and the concentration of oxygen and nutrients (n). The discrete variable c_v describes the sprout dynamics.

Spatiotemporal evolution of MSCs:

$$\frac{\partial c_m}{\partial t} = \nabla \cdot (\underbrace{D_m \nabla c_m}_{\text{diffusion}} - \underbrace{C_{mCT}\, c_m \nabla(g_b + g_v)}_{\text{chemotaxis}} - \underbrace{C_{mHT} c_m \nabla m}_{\text{haptotaxis}}) \tag{5.1}$$

$$+\underbrace{A_m c_m (1 - a_m c_m)}_{\text{proliferation}} - \underbrace{F_1 c_m}_{\substack{\text{osteogenic}\\ \text{differentiation}}} - \underbrace{F_2 c_m}_{\substack{\text{chondrogenic}\\ \text{differentiation}}} - \underbrace{F_4 c_m}_{\substack{\text{fibroblastic}\\ \text{differentiation}}}$$

Spatiotemporal evolution of fibroblasts:

$$\frac{\partial c_f}{\partial t} = \nabla \cdot \left(\underbrace{D_f \nabla c_f}_{\text{diffusion}} - \underbrace{C_f c_f \nabla g_b}_{\text{chemotaxis}}\right) + \underbrace{A_f c_f \left(1 - a_f c_f\right)}_{\text{proliferation}} \tag{5.2}$$

$$+ \underbrace{F_4 c_m}_{\substack{\text{fibroblastic}\\ \text{differentiation}}} - \underbrace{F_3 d_f c_f}_{\substack{\text{endochondral}\\ \text{ossification}}}$$

Spatiotemporal evolution of chondrocytes:

$$\frac{\partial c_c}{\partial t} = \underbrace{A_c c_c (1 - a_c c_c)}_{\text{proliferation}} + \underbrace{F_2 c_m}_{\substack{\text{chondrogenic}\\ \text{differentiation}}} - \underbrace{F_3 c_c}_{\substack{\text{endochondral}\\ \text{ossification}}} \tag{5.3}$$

Spatiotemporal evolution of osteoblasts:

$$\frac{\partial c_b}{\partial t} = \underbrace{A_b c_b (1 - a_b c_b)}_{\text{proliferation}} + \underbrace{F_1 c_m}_{\substack{\text{osteogenic}\\ \text{differentiation}}} + \underbrace{F_3 c_c}_{\substack{\text{endochondral}\\ \text{ossification}}} - \underbrace{d_b c_b}_{\substack{\text{osteocyte}\\ \text{differentiation}}} \tag{5.4}$$

Spatiotemporal evolution of fibrous matrix density:

$$\frac{\partial m_f}{\partial t} = \underbrace{P_{fs}\left(1 - \kappa_f m_f\right) c_f}_{\text{production}} + \underbrace{Q_f m_f m_c c_b}_{\text{resorption}} \tag{4.5}$$

Spatiotemporal evolution of cartilaginous matrix density:

$$\frac{\partial m_c}{\partial t} = \underbrace{P_{cs}(1-\kappa_c m_c)c_c}_{production} - \underbrace{Q_c m_c c_b}_{resorption} \tag{5.6}$$

Spatiotemporal evolution of bone matrix density:

$$\frac{\partial m_b}{\partial t} = \underbrace{P_{bs}(1-\kappa_b m_b)c_b}_{production} \tag{5.7}$$

Spatiotemporal evolution of chondrogenic growth factor concentration:

$$\frac{\partial g_c}{\partial t} = \nabla\big(\underbrace{D_{gc}\nabla g_c}_{diffusion}\big) + \underbrace{E_{gc}c_c}_{production} - \underbrace{d_{gc}g_c}_{denaturation} \tag{5.8}$$

Spatiotemporal evolution of osteogenic growth factor concentration:

$$\frac{\partial g_b}{\partial t} = \nabla\big(\underbrace{D_{gb}\nabla g_b}_{diffusion}\big) + \underbrace{E_{gb}c_b}_{production} - \underbrace{d_{gb}g_b}_{denaturation} \tag{5.9}$$

Spatiotemporal evolution of vascular growth factor concentration:

$$\frac{\partial g_v}{\partial t} = \nabla\big(\underbrace{D_{gv}\nabla g_v}_{diffusion}\big) + \underbrace{E_{gvb}c_b + E_{gvc}c_c}_{\substack{hypoxia\text{-}independent\\ production}}$$

$$-g_v\Big(\underbrace{d_{gv}}_{denaturation} + \underbrace{d_{gvc}c_v}_{\substack{cellular\\ uptake}}\Big) \tag{5.10}$$

Spatiotemporal evolution of oxygen & nutrients concentration:

$$\frac{\partial n}{\partial t} = \nabla\big(\underbrace{D_n\nabla n}_{diffusion}\big) + \underbrace{E_n c_v}_{production} - \underbrace{d_n n}_{consumption} \tag{5.11}$$

After the inflammation stage, the granulation tissue (contributing to m_f), fibroblasts (c_f), MSCs (c_m) and osteogenic growth factors fill the fracture callus. The MSCs differentiate into osteoblasts (c_b) (intramembranous ossification (m_b)) and the chondrocytes (c_c) lay down a cartilage template (m_c) which fills the callus region. The hypertrophic chondrocytes express VEGF and other angiogenic growth factors (g_v). As a result, osteoblasts and blood vessels are attracted. Woven bone (endochondral ossification (m_b)) gradually resorbs and replaces the cartilage template.

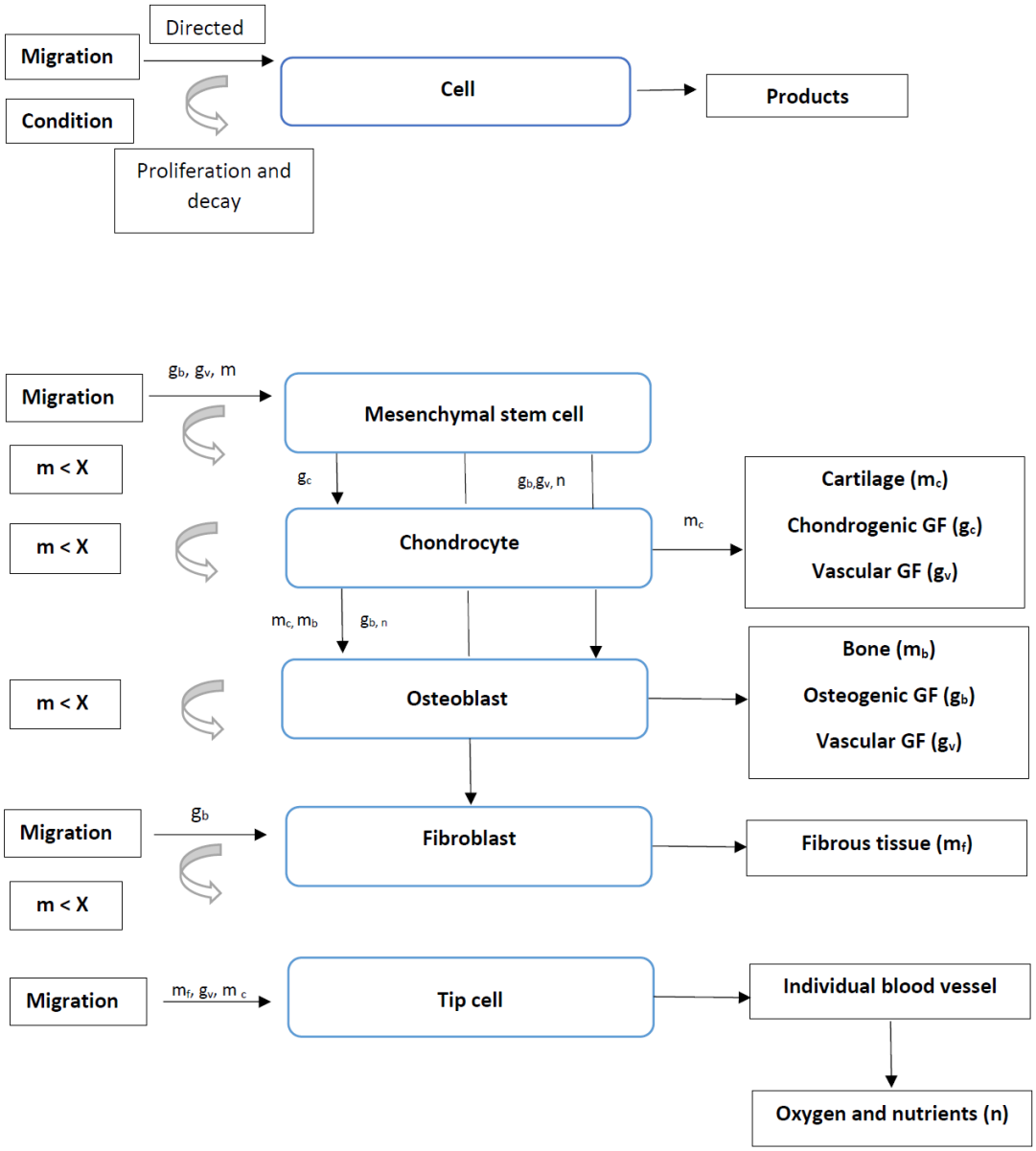

Figure 5.1 Schematic overview of the model.

The total tissue density is: $m=m_c+m_f+m_b$. X is the maximum tissue density for proliferation. If a variable is involved in a regeneration subprocess, it is noted by demonstrating that variable next to the arrow describing that process.

The parameters of the model were taken from *in vitro* and *in vivo* experiments by Geris et al. (2008). When there were none experimental values for some parameters, they were estimated by considering the results of a mathematical stability analysis and confirmed by comparison with a normal femoral rodent fracture healing (Harisson et al. 2003). The functional forms related to migration (C_{mCT}, D_m, C_f, C_{mHT}) proliferation (A_b, A_c, A_f, A_m), chondrogenic differentiation (F_2) and chondrogenic and osteogenic growth factor production (E_{gb}, E_{gc}) were derived from Geris et al. (2008). Functional forms related to vascular growth factor production and osteogenic differentiation were modified to consider the effect of oxygen and nutrients.

The differentiation of mesenchymal stem cells toward osteoblasts is given by:

$$F_1 = \left(\frac{Y_{11} g_b}{H_{11}+g_b} + \frac{Y_{11} g_v}{H_{12}+g_v}\right) \cdot \frac{Y_{12} n^6}{I_v^6+n^6} \quad (5.12)$$

The factor between the brackets indicates that both angiogenic and osteogenic growth factors mediate the differentiation. The last factor expresses that the intramembranous ossification depends on the availability of nutrients and oxygen.
The differentiation of mesenchymal stem cells toward chondrocytes is given by:

$$F_2 = \frac{Y_2 g_c}{H_2+g_c} \cdot \frac{Y_{2n} n}{K_{2n}^6+n^6} \quad (5.13)$$

The endochondral ossification is given by:

$$F_3 = \frac{m_c^6}{B_{ec}^6+m_c^6} \cdot \frac{Y_3 g_b}{H_3+g_b} \cdot \frac{n^6}{B_v^6+n^6} \quad (5.14)$$

The first factor shows that only hypertrophic chondrocytes play a part in the endochondral ossification. The other factors express that the osteogenic growth factors (second factor) and oxygen and nutrients (last factor) are essential.

The oxygen and nutrients released by blood vessels are given by:

$$E_n = \frac{G_n H_n^6}{H_n^6+n^6} \quad (5.15)$$

The functional forms in equations 1-11 that have not been changed from Geris et al. (2008) are summarized below:

-Random motion and haptokinesis: $D_m = \frac{D_{hm} m}{K_{hm}^2+m^2}$ (5.16)

-Chemotaxis of mesenchymal stem cells: $C_{mCT} = \frac{C_{mCT}(g_b+g_v)}{K_{kCTm}^2+(g_b+g_v)^2}$ (5.17)

-Chemotaxis of fibroblasts: $C_f = \frac{C_{kf} g_b}{K_{kf}^2+g_b^2}$ (5.18)

-Haptotaxis: $C_{mHT} = \frac{C_{kHTm}}{(K_{kHTm}+m)^2}$ (5.19)

-Proliferation: $A_i = \frac{A_{i0} m}{K_i^2+m^2} \cdot \frac{A_{in} n}{K_{in}^2+n^2}$ for i=*m, f, c, b* (5.20)

-Production of chondrogenic growth factors: $E_{gc} = \frac{G_{gc} g_c}{H_{gb}+g_c} \times \frac{m}{K_{gc}^3+m^3}$ (5.21)

Production of osteogenic growth factors: $E_{gb} = \frac{G_{gc} g_c}{H_{gb}+g_c}$ (5.22)

However, the model must be adapted in order to consider the influence of US. For this reason, the idea of Xu et al. (2006) was adopted. When a fluid-saturated medium is subjected to a small amplitude oscillatory pressure gradient, such as under US influence, the pressure fluctuation causes micro fluid flow through the sample so that to release the differential pressure. This effect can be described by dynamic diffusion:

$$\frac{\partial p}{\partial t} = \nabla\left(D_p \nabla \mathrm{p}\right) \tag{5.23}$$

where D_p is the diffusivity of the US acoustic pressure.

When pressure p is accredited to interstitial fluid pressure, through Darcy's law the pressure gradient is correlated to interstitial fluid velocity:

$$\boldsymbol{u} = -K \nabla \mathrm{p} \tag{5.24}$$

where K is the hydraulic conductivity of the interstitium or permeability coefficient.

Adopting the idea of Phips and Kohandel (2011), who proposed a mathematical model to describe the diffusion of proangiogenic (f_p) and antiangiogenic (f_a) factors in solid tumors:

$$\frac{\partial f_i}{\partial t} = D_j \nabla^2 f_j - k_j f_j + g_j - \nabla \cdot (\boldsymbol{u} f_i),\ j = p, a \tag{5.25}$$

with D_j, k_j and g_j illustrated in Phips and Kohandel (2011).

Eq. (5.10) was modified in order to introduce the US influence on VEGF (g_v):

$$\begin{aligned}\frac{\partial g_v}{\partial t} = {} & \nabla \cdot \left(D_{gv} \nabla g_v\right) + E_{gvb} c_b + E_{gvc} c_c - g_v\left(d_{gv} + d_{gvc} c_v\right) \\ & -\nabla \cdot (\mathbf{u} \mathrm{g_v})\end{aligned} \tag{5.26}$$

where **u** satisfies Eq. (5.24).

In Eq. (5.26) by replacing **u** via Darcy's law it can be written in terms of interstitial pressure p:

$$\begin{aligned}\frac{\partial g_v}{\partial t} = {} & \nabla \cdot \left(D_{gv} \nabla g_v + K g_v \nabla p\right) + E_{gvb} c_b + E_{gvc} c_c \\ & -g_v\left(d_{gv} + d_{gvc} c_v\right)\end{aligned} \tag{5.27}$$

Equations (5.1)-(5.9), (5.11), and (5.27) are the system of PDEs that constitute the new model. The variables, functional forms, and non-dimensionalized parameters in these PDEs are the same as those in the model by Peiffer et. al. (2011).

The base of the model of blood vessel network is the solution of tip cell velocity equations proposed by Sun et al. (2005). In order to simulate blood vessel growth, tip velocity equations are solved. These equations describe the motion of the corresponding tip cell (Sun et al. 2005, Peiffer et al. 2011).

5.2 Mathematical description of angiogenesis

The discrete value c_v represents the blood vessels. In equations (5.10) and (5.11) takes the value 1 when a grid volume has a blood vessel and otherwise takes the value 0. This indicates that the vessel diameter is defined by grid resolution in its current implementation. The evolution of c_v depends on anastomoses, branching and blood vessel growth.

Blood vessel growth

The model computes the movement of the corresponding tip cell, to describe the growth of blood vessel. This is achieved by solving tip cell velocity equations of the form:

$$\frac{d\boldsymbol{x}_t}{dt} = v_t \frac{\boldsymbol{u}_t}{\|\boldsymbol{u}_t\|_2} \tag{5.28}$$

where $\mathbf{x}_t$ represents the position, u_t the speed and $\mathbf{u}_t$ the direction of motion of the tip cell. The concentration of VEGF affects the tip cell speed.

When VEGF concentrations is below $g_v^* = 10\ ng/ml$, there is no blood vessels growth. When VEGF concentrations are higher, the tip cells move faster. This is mathematically described as:

$$u_t = \begin{cases} 0, & if\ g_u < g_u^* \\ u_t^{max} \frac{g_u^6}{g_u^6 + (g_u^*)^6} & if\ g_u \geq g_u^* \end{cases} \quad \text{where } u_t^{max} = 35\ \mu m/day \tag{5.29}$$

The direction of tip cell movement is described by:

$$\boldsymbol{u}_t = K(k_c \nabla g_v + k_h \nabla(m_f + m_c)) \quad \text{where } k_c = 1 - k_h \tag{5.30}$$

The chemotactic coefficient (k_c) and haptotactic coefficient (k_h) are set to 0.5.

$$\text{The matrix } K \text{ is defined as: } K = \begin{pmatrix} 1 & 0 \\ 0 & 1 \end{pmatrix} + k_a \begin{pmatrix} -u_y^2 & u_x u_y \\ u_x u_y & -u_x^2 \end{pmatrix} \tag{5.31}$$

Where the unit vector (u_x, u_y) determines the orientation of the matrix fibers and parameter k_a describes the influence of the fiber orientation on the growth direction of blood vessels. The k_a value can vary from 0 (no influence) up to 1 (maximal influence).

5.3 Model parameters, initial and boundary conditions and geometry

Model parameters

In order to calculate the diffusivity of US acoustic pressure D_p, the corresponding materials properties are used, since at the beginning of the fracture healing the bone callus is loaded with only granulation tissue. As a result, D_p equals to 28.7×10^{-3} mm^2/day (Cowin, 1999).

The hydraulic conductivity K equals the permeability coefficient. According to Cowin (1999), for the granulation tissue it equals to 10^{-14} m^4/Ns. However, simulations are also performed for the values of cartilage ($K=10^{-15}$ m^4/Ns) and bone ($K=10^{-16}$ m^4/Ns) (Johnson 1984, Cowin 1999) in order to examine the sensitivity of the model result for different combinations of D_p and K.

The influence of US intensity on bone healing is examined for four different values i.e. I_1=15, I_2=30, I_3=60 and I_4=75 mW/cm^2. The intensity is proportional to the square of acoustic pressure, in the case of a linear wave propagation:

$$I = \frac{|p|^2}{Z} \tag{5.32}$$

where p is the acoustic pressure and Z the acoustic impedance. Using the Z value for blood i.e. $Z=1.66$ Kg/m^2, and the four values for intensity, four different values of acoustic pressure are derived i.e., p_1=0.8, p_2=2.4, p_3=4.8 and p_4=6.1 kPa which are used as boundary conditions.

The new parameters which are introduced are non-dimensionalized using these equations:

$$\widetilde{D}_p = \frac{D_p T}{L^2}, \widetilde{K} = \frac{KT}{L^4} F_o, \tilde{p} = \frac{p}{p_o} \tag{5.33}$$

where L=3.5 mm, T=1 day, F_o=1.5kN, p_o=1kPa.

Geometrical domain

For numerical implementation, a spatial domain taken from a real callus geometry of a standardized femoral rodent fracture was used. The initial and boundary conditions are based on Grestenfield et al. (2003). All variables are deemed no-flux boundary conditions, except from those demonstrated in Fig. 5.1. Only one-fourth of the domain is considered due to symmetry issues. At the beginning of the fracture healing, the callus is thought to be filled with fibrous tissue i.e. $m_f^{init} = 10$ mg/ml. During the first 3 post-fracture (PF) days, fibroblasts and mesenchymal stem cells are released into the callus tissue from periosteum, the bone marrow and the surrounding tissues ($c_f^{bc} = 2x10^4$cells/ml and $c_m^{bc} = 2x10^4$cells/ml). During the first 5 PF days, an initial amount of chondrogenic growth factors is considered at the degrading bone ends ($g_c^{bc} = 2x10^4$mg/ml). During the first 10 PF days, osteogenic growth factors are also released through the cortex ($g_b^{bc} = 2x10^4$mg/ml).

Periosteum acts as a source of ultrasound acoustic pressure to stimulate transducers' application during axial ultrasound transmission. Four different boundary conditions i.e., p_1=0.8, p_2=2.4, p_3=4.8 and p_4=6.1 kPa are examined, in order to simulate US treatments at different intensities, such as *in vitro* and *in vitro* experiments.

All bone healing simulations have been performed though the two-dimensional (2D) model shown in Fig. 5.2. This simplification is not far from the real solidification process because fracture healing is almost an axisymmetric problem.

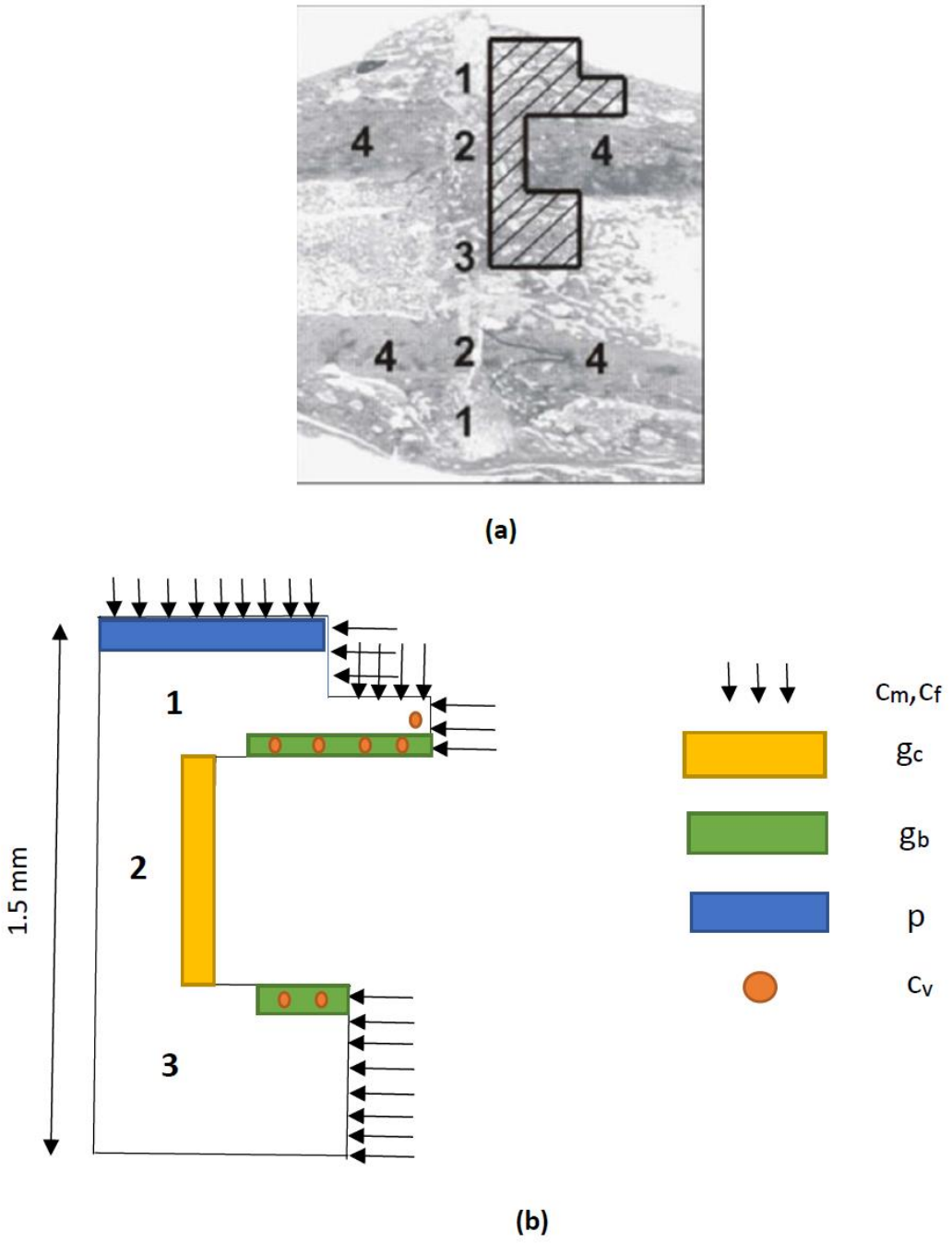

Figure 5.2 (a) The geometrical domain of the model: (1) periosteal callus, (2) intercortical callus, (3) endosteal callus, (4) cortical bone ends. (b) The callus region used for the model with boundary conditions and initial positions of the tip cells. The origin of the coordinate system is placed in the left bottom corner of the geometrical domain.

Numerical implementation

The system of the partial differential equations is solved on a 2D grid with a grid cell size of 25μm, with the method of lines (MOL). Using finite volume method, the PDEs are spatially discretized ensuring non-negativity of the variables and mass conservation (Gerisch and Chaplain, 2006). The resulting ordinary differential equations (ODEs) are solved using ROWMAP, a ROW-code of order 4 with Krylov

techniques for large stiff ODEs (Weiner et al. 1997). After each time step for the continuous variables, the location and the intracellular level of the discrete ECs is updated. The haptotactic guidance of the tip cell motion is randomly initialized.

D_m	Mesenchymal stem cells' migration
D_f	Fibroblasts' migration
D_{gc}	Chondogenic growth factors' migration
D_{gb}	Osteogenic growth factors' migration
D_{gv}	Vascular growth factors' migration
D_n	Oxygen & nutrinets'migration
C_{mCT}	Chemotactic response of mesenchymal stem cells
C_{mHT}	Haptotactic response of mesenchymal stem cells
A_m	Proliferation rate of mesenchymal stem cells
A_f	Proliferation rate of fibroblasts
A_c	Proliferation rate of chondrocytes
A_b	Proliferation rate of osteoblasts
F_1	Differentiation towards osteogenic and angiogenic factors
F_2	Differentiation towards chondrocytes
F_3	Endochondral replacement of chondrocytes
F_4	Differentiation towards fibroblasts
C_f	Chemotactic response of fibroblasts
P_{cs}	Cartlage's matrix synthesis rate
P_{bs}	Bone's matrix synthesis rate
P_{fs}	Fibroblast's matrix synthesis rate
Q_f	Fibrous tissue degradation component during endochondral ossification
Q_c	Cartilage degradation component during endochondral ossification
E_{gc}	Production of chondogenic and osteogenic growth factors by chondocytes
E_{gb}	Production of chondogenic and osteogenic growth factors by osteoblasts
E_{gvb}	Production of aniogenic growth factors by osteoblasts
E_{gvc}	Production of aniogenic growth factors by chondrocytes
E_n	Oxygen & nutrinets's release by the blood vessels
d_{gv}	Consumtion of angiogenic growth factor
d_{gv}	Consumtion of angiogenic growth factor through chondrocytes
d_b	Consumtion of osteoblasts
d_{gc}	Consumtion of chondrogenic growth factor
d_{gb}	Consumtion of osteogenic growth factor
d_n	Consumtion of oxygen & nutrients

Table 5.1 Summary of the functional terms in the model of Peiffer.

CHAPTER 6

NUMERICAL METHODS

6.1 ROWMAP

ROWMAP is a ROW-code with Krylov techniques for large stiff initial value problems. The base of the method is the ROW-methods of the code ROS4 of Hairer and Wanner. Krylov techniques are used for the solution of linear systems. A special multiple Arnoldi procedure assures order p=4 already for low dimensions of the Krylov subspaces separately of the dimension of the differential equations.

Introduction

For the numerical solution of stiff initial value problems:

$$y'(t) = f\big(t, y(t)\big),$$
$$y(t_0) = y_0 \,\epsilon\, R^n, \tag{6.1}$$

implicit or linearly implicit methods must be applicated for stability. For large dimensions *n*, most of the computing time of these methods is consumed for the calculation of the Jacobian and in the solution of linear equations. Krylov methods have been widely applicated in implicit methods for stiff ordinary differential equations to stimulate the linear algebra in these integration systems. Krylov techniques in ODE codes are do not require the explicit computation and storage of the full Jacobian ("matrix-free methods") and do not require special structure of the systems (banded Jacobian, etc.). However, the methods exploit sparsity. ROW-methods are very efficient solution methods for stiff problems. The code ROS4 executes well for low and medium accuracy requirements.

A ROW-method for autonomous systems (6.1) is given by:

$$(I - h\gamma A)(k_i + \sum_{j=1}^{i-1} \frac{\gamma_{ij}}{\gamma} k_j) = f_i + \sum_{j=1}^{i-1} \frac{\gamma_{ij}}{\gamma} k_j,$$
$$f_i = f(u_{m+1}^{i}),$$
$$u_{m+1}^{(i)} = u_m + h \sum_{j=1}^{i-1} a_{ij} k_j,$$
$$u_{m+1} = u_m + \; h \textstyle\sum_{i=1}^{s} b_i k_j, \tag{6.2}$$

where $A = f_y(u_m)$ (6.3)

if some approximation *T* replaces A, Eq. (6.2) becomes a *W-method.*

Krylov-W-methods are considered where low-rank approximations replaces the matrix *A*: $T_i = Q_i Q_i^T A$ (6.4)
at each stage. The orthogonal matrices $Q_i = \{q_1, \dots, q_{ki}\} \,\epsilon\, R^{n,\kappa_i}$, where Q_i $(i > 1)$ is an extension of Q_{i-1}, are calculated using a special multiple Arnoldi process (MAP). The stage equation (6.2) becomes:

$$(I - h\gamma T_i)(k_i + \textstyle\sum_{j=1}^{i-1} \frac{\gamma_{ij}}{\gamma} k_j) = f_i + \sum_{j=1}^{i-1} \frac{\gamma_{ij}}{\gamma} k_j =: w_i. \tag{6.5}$$

Since:

$$(I - h\gamma Q_i Q_i^T A)^{-1} = I + h\gamma Q_i (I - h\gamma H_\iota)^{-1} Q_i^T A, \qquad H_\iota = Q_i^T A\, Q_i \in R^{\kappa_i,\kappa_i}, \tag{6.6}$$

the stage increment k_i may be calcylated by:

$$k_i = (I - h\gamma T_i)^{-1} w_i - \sum_{j=1}^{i-1} \frac{\gamma_{ij}}{\gamma} k_j = [I + h\gamma Q_i (I - h\gamma H_i)^{-1} Q_i^T A]\, w_i - \sum_{j=1}^{i-1} \frac{\gamma_{ij}}{\gamma} k_j, \tag{6.7}$$

and equations must be solved for dimension κ_i only. The special Arnoldi process assurres, that the right-hand side w_i at the *i*th stage belongs to the subspace:

$$K_i = span\,\{q_1, \dots, q_{ki}\} = range\; Q_i, \tag{6.8}$$

i.e. $Q_i Q_i^T w_i = w_i$ (6.9)

In this case the relation (6.7) is further simplified leading to *Krylov-W-method*:

$$k_i = Q_i (I - h\gamma H_i)^{-1} Q_i^T w_i - \sum_{j=1}^{i-1} \frac{\gamma_{ij}}{\gamma} k_j,$$

$$w_i = f_i + \sum_{j=1}^{i-1} \frac{\gamma_{ij}}{\gamma} k_j,$$

$$f_i = f(u_{m+1}^i),$$

$$u_{m+1}^{(i)} = u_m + h \sum_{j=1}^{i-1} a_{ij} k_j,$$

$$u_{m+1} = u_m + h \sum_{i=1}^{s} b_i k_j. \tag{6.10}$$

Extensive numerical tests have been performed with a 3-stage method of order 2. The main results are:

- Krylov-W-method is efficient for low accuracy requirements comparing with multistep code VODPK.
- The dimensions of Krylov subspaces must be limited in order to ensure the memory requirements of the Arnoldi process. The stability of the method is sufficient for low Krylov dimensions and was primarily affected by the first stage. The evaluation of the linear case showed that the dimension of the Krylov subspace must be increased at least by one for each new function evaluation at a higher stage. This rule must be followed in the limits on κ_i at different stages.
- The proper control of the stage residuals (ktol) of the Krylov process in relation to the accuracy tol applied for the overall integration system, is one of the main difficulties of the system. Buttner et al. (1995) performed an error analysis and proposed a choice ktol≈tol/h. However, this tolerance was missed sometimes

due to practical restrictions of the Krylov subspace dimensions. The code though still executed well in situations where the residuals of the stage systems were much larger than ktol. The stepsize control maintained the overall accuracy of the code. This suggests that the basis of the stepsize control procedure was robust for definite restrictions on the dimensions κ_i. As a result, a proper relation was found between the embedded solutions and the errors of the propagated.

A special multiple Arnoldi process

For the determination of the approximate solution u_{m+1} (6.2) *s* systems of linear equations with the same coefficient matrix must be solved. Firstly, for the solution of: $(I - h\gamma A)\widetilde{k_i} = w_i$, the classical Arnoldi method may be used to create a sequence of orthonormal vectors $q_1, \dots, q_{ki}$ that are the basis for the Krylov subspace:

$K_1 = K(A, q_1, \kappa_1) \coloneqq span\{q_1, \dots A\kappa^{\kappa_1 - 1} q_1\}.$

This procedure incorporates Krylov steps A_{qj} with Gram-Schmit-orthogonalization:

$$q_{j+1} = \frac{u}{\|u\|_2}, \quad u = \left(I - \sum_{l=1}^{j} q_i q_i^T \right) A q_j.$$

With the vectors q_j the matrices $Q_1 = (q_1, \dots, q_{ki})$ and $H_1 = Q_1^T A Q_1$are created. The matrix $H_1$is in Hessenberg form. The residual of the Krylov approximation from (6.10) can be calculated from subspace data:

$r \coloneqq (I - h\gamma A)k_1 - w_1 = -h\gamma(I - Q_1 Q_1^T) A q_{\kappa_1} e_{\kappa_1}^T l_1$

$$l_1 = (I - h\gamma H_1)^{-1} Q_1^T w_1. \tag{6.11}$$

without knowing $k_1 = Q_1 l_1$. At higher stages i>1 the data about *A* included in Q_1 and H_1 is re-used and the Arnoldi procedure is carried on in an appropriate way.

The ROW-methods of order 4 are basic integration methods (except for GR4A) and have the following properties:

- $b_3 = 0$
- $f_4 = f_3$,
- an embedded method of order $p = 3$ has been created.

The Krylov-W-method ROWMAP employs the subsequent special multiple Arnoldi process. The gram-Schmidt orthonalization was formalized:

$u \xleftarrow{GS(i)} w \Leftrightarrow$ u:=$(I - \sum_{m=1}^{i} q_m q_m^T) w$,

in order to improve the readability of this method.

Special Multiple Arnoldi Process (MAP) for ROWMAP

Stage 1: Classical Arnoldi procedure

$q_1 := \frac{u}{\|u\|}, \quad u := w_1 = f(u_m),$

$q_{j+1} := \frac{u}{\|u\|}, \quad u \xleftarrow{GS(i)} Aq_j, \;\; j = 1, \dots, \kappa_1 - 1, \kappa_1 \geq 4.$

Stage 2: $\kappa_2 = \kappa_1 + 3$, involve w_2, one block Arnoldi step with block-size 2.

$q_{\kappa+1} := \frac{u}{\|u\|}, \quad u \xleftarrow{GS(\kappa_1)} w_2,$

$q_{\kappa_1+2} := \frac{u}{\|u\|}, \quad u \xleftarrow{GS(\kappa_1+1)} Aq_{\kappa_1},$

$q_{\kappa_2} := \frac{u}{\|u\|}, \quad u \xleftarrow{GS(\kappa_1+2)} Aq_{\kappa_{1+1}}.$

Stage 3: $\kappa_3 = \kappa_2 + 1$, involve w_3.

$q_{\kappa_3} := \frac{u}{\|u\|}, \quad u \xleftarrow{GS(\kappa_2)} w_3.$

Stage 4: Finally, **:** $\kappa_4 = \kappa_3 + 3$, one block Arnoldi step with block-size 3.

$q_{\kappa_3+1} := \frac{u}{\|u\|}, \quad u \xleftarrow{GS(\kappa_3)} Aq_{\kappa_{1+2}},$

$q_{\kappa_3+2} := \frac{u}{\|u\|}, \quad u \xleftarrow{GS(\kappa_{3+1})} Aq_{\kappa_2},$

$q_{\kappa_4} := \frac{u}{\|u\|}, \quad u \xleftarrow{GS(\kappa_3+2)} Aq_{\kappa_3}.$

The basis vectors are gathered in matrices $Q_i = (q_1, \dots, q_{\kappa i})$ and their column spaces are: $K_i = spanQ_i, i$ =1,…4.

- The first dimension κ_i is at least 4 and regulated by accuracy requirements for the residual *r*. The other dimensions grow by at most $\kappa_2 = \kappa_1 + 3$, $\kappa_3 = \kappa_2 + 1$, $\kappa_4 = \kappa_3 + 3$.
- If one of the vectors *u* disappears, the equivalent step is avoided decreasing the Krylov dimensions.
- The subspace is extended by w_3 only at the third stage, since the weight b_3 is zero.
- The right-hand side w_4 in step 4 is already included in the Krylov subspace K_3 since $f_4 = f_3$.

The approach for selecting the sequence of basic vector yields the following properties:

1. $w_i \in K_{i,}\ i = 1, \dots, 4.$
2. $Aq_l \in span\{q_1, \dots, q_k\}, l = 1, \dots, \kappa_3.$
3. If at some stage l and some $k \leq i$ holds

$$\left(T_i^l - A^l\right) w_k = 0 \; for \; l = 1, \dots, q,$$

then the same is true for stage $j > i \geq k$:

$$\left(T_i^l - A^l\right) w_k = 0 \; for \; l = 1, \dots, q.$$

The matrices $H_i = Q_i^T A Q_i, i > 1$, generated by the MPA will no longer be in strict Hessenberg form. At stages 2 and 3, extra subdiagonals emerge starting in columms κ_1 and κ_2. If $\kappa_1 \geq 4$, the ROWMAP method with $b_3 = 0$ has consistency order *p=4* too.

The order has been acquired under the condition of classical consistency order ($\|hA\| \to 0$). However, this may not be realistic for very stiff systems. The stepsize control is performed following the classical orders. The special MAP maintains these classical orders.

ROWMAP has order *p=4* with Krylov dimensions:

$$\kappa_1 \geq 4, \; \kappa_{\mathbf{2}} = \kappa_1 + 3, \; \kappa_{\mathbf{3}} = \kappa_2 + 1, \kappa_{\mathbf{4}} = \kappa_3 + 3 \tag{6.12}$$

independent of *n*. The essential subspace dimensions are 4, 7, 8, 11. For stability reasons however, a larger dimension is required $\kappa_1 \geq 4$. In ROWMAP for the step $t_m \to t_{m+1}$ the dimension κ_1 is determined by the condition:

$$h \cdot \sqrt{\frac{1}{n} \sum_{i=1}^{n} \left(\frac{r_i}{atol_i + rtol_i |u_i(t_m)|}\right)^2} \leq \theta. \tag{6.13}$$

r is the stage residual, $atol_i$ and $rtol_i$ are the components of an absolute and a relative tolerance vector and $u(t_m)$ is the numerical solution at t_m. If (6.13) cannot be assured during the Arnoldi repetition because of memory restrictions on κ_1 the orders 4(3) of ROWMAP are still accurate if the rules (6.12) are adopted. As a result, the stepsize control still should be capable of handling the case by reducing the stepsize.

6.2 Finite Volume Method

The Finite Volume Method (FMV) is a discretization method for the approximation of a single or a system of partial differential equations (PDEs). These equations are used to model a broad number of fields. They specify the relationships between partial derivatives of unknown fields, respecting variables inside the domain (space, time).

A mesh is created, which exists in a segregation of the domain where the space variable resides. The elements of the mesh are called control volumes. The integration of the PDE for each control volume develops a balance equation. The set of balance equations is then discretized according to a set of discrete unknowns.

In order to FVM to be efficient, the main concern is the discretization of the fluxes at the boundaries of each control volume. To ensure efficiency, the numerical fluxes are generally:

- conservative, i.e. the flux joining a control volume from its neighbor must be the opposite of the one joining the neighbor of this control volume,
- consistent, i.e. the numerical flux of a regular function interpolation keeps the continuous flux as the mesh size vanishes.

The derived system of discrete equations depends on a finite set of unknowns, and may be linear or non-linear, depending on the original problem. Subsequently, this system is solved exactly or approximately, using direct or iterative solvers (linear equations) and fixed points or Newton type methods (nonlinear equations).

Fundamental principles

The following PDE is under conservative form:

$$\partial_t A(x,t) + \nabla \cdot F(x,t) = S(x,t) \tag{6.13}$$

where the space variable *x* is part of the domain $\Omega \subset R^d$ (d is the space dimension, with d≥ 1), and the time variable *t* is part of interval [0,*T*], with *T*>0. The scalar function *A*, defined in Ω x [0,*T*], indicates the density of some quantity, and $\partial_t A$ is the time derivative. The function *F*, defined in Ω x [0,*T*] and valued R^d, indicates the flux of this quantity, and $\nabla \cdot F$ is the space divergence. The function *S*, defined in Ω x [0,*T*] and valued in R, is a source term. The initial condition: $A(x,0) = A_{ini}(x)$ for $x \epsilon \Omega$ is inflicted, where the function $A_{ini}|$ is defined in Ω and valued in R. Boundary conditions are also applied, that depend on the considered equation. Functions *A* and *F* may not be regular, so the derivatives in (6.13) may be weak.

The functions *A*, *S* and *F* are connected to a set of unknown fields $(u_j)_{j=1,\dots,N}$, where u_j is an unknown function defined from Ω x [0,*T*] to R. Such connections can be written as:

$$\begin{gathered} A(x,t) = A(u_1(x,t), \dots, u_N(x,t)x,t), \\ S(x,t) = S(u_1(x,t), \dots, u_N(x,t)x,t), \\ F(x,t) = F(u_1(x,t), \dots, u_N(x,t), \nabla u_1(x,t), \dots, \nabla u_N(x,t)x,t), \end{gathered} \tag{6.14}$$

where the functions *A*, *S* and *F* are given.

The domain Ω is divided into a mesh, *M*. The mesh M is a finite set of nonoverlapping subsets of Ω, which satisfy some regularity properties. Some of these properties are critical for the analysis of the scheme, while others are critical to assure the convergence and precision the of the method, depending on the type of term that is discretized. The elements of *M*, *K* and *L*, are the control volumes. $|K|$ is the measure of a control volume *K* (its length if *d*=1, area if *d*=2, volume if *d*=3). The boundary ϑK of each control volume *K* is segregated into the finite set ε_K, named the set of the extremities (*d*=1) or edges (*d*=2) or faces (*d*=3) of *K*. An element of σ of ε_K is either placed on the boundary of Ω or belongs to $\varepsilon_K \cap \varepsilon_L$, where *K* and *L* are two neighboring control volumes.

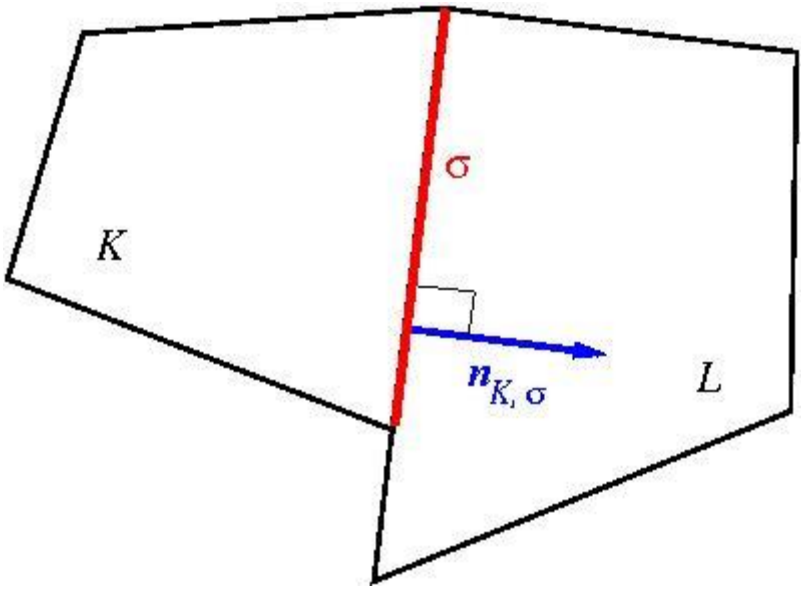

Figure 6.1 Two control volumes with a common face (Eymard 2010)

The (d-1)-dimensional measure of a face $\sigma \in \varepsilon_K$ is $|\sigma|$. A strictly growing finite sequence $t^{(0)} = 0 < t^{(1)} < \cdots < t^{(N)} = T$ is set for the time discretization, with $\delta t^{(n)} = t^{(n)} - t^{(n-1)}$ for $n = 1, \ldots, N$. The classical finite volume estimation relies on the estimation of the balance equations of the control volumes between time $t^{(n-1)}$ and t^n. These balance equations can be acquired by integrating (6.13) on $K \times [t^{(n-1)}, t^n]$ and using the divergence formula:

$$\int_K \left(A\left(x, t^{(n)}\right) - A\left(x, t^{(n-1)}\right)\right) dx + \sum_{\sigma \in \varepsilon_K} \int_{t^{(n-1)}}^{t^{(n)}} \int_\sigma F(x,t) \cdot \boldsymbol{n}_{K,\sigma}(x)\, ds(x) dt =$$

$$\int_{t^{(n-1)}}^{t^{(n)}} \int_K S(x,t) dx dt,$$

where ds(x) is the integration complying with the (d-1)-dimensional measure of the boundary and $\boldsymbol{n}_{K,\sigma}(x)$ is the unit vector normal to σ at point x, outward to K. The discretization of the above balance equation can be written as:

$|K|\left(A_K^{(n)} - A_K^{(n-1)}\right) + \delta t^{(n)} \sum_{\sigma \in \varepsilon_K} |\sigma| F_{K,\sigma}^{(n)} = \delta t^{(n)} |K| S_K^{(n)}$,

where $A_K^{(n)}$ (resp. $A_K^{(0)}$) estimates $\frac{1}{|K|}\int_K A(x, t^n) dx$ (resp. $\frac{1}{|K|}\int_K A_{ini}(x) dx$),

$F_{K,\sigma}^{(n)}$ estimates $\Phi_{K,\sigma}^{(n)} = \frac{1}{\delta t^{(n-1)}} \int_{t^{(n-1)}}^{t^{(n)}} \int_\sigma F(x,t) \cdot \boldsymbol{n}_{K,\sigma}(x) ds(x) dt$,

and $S_K^{(n)}$ estimates $\frac{1}{\delta t^{(n)} |K|} \int_{t^{(n-1)}}^{t^{(n)}} \int_K S(x,t) dx dt$.

For a face σ common to two control volumes K and L, since $\boldsymbol{n}_{K,\sigma}(x) + \boldsymbol{n}_{L,\sigma} = 0$ for $x \in \sigma$, the normal fluxes in the original problem satisfy the conservation property:

$\Phi_{K,\sigma}^{(n)} + \Phi_{L,\sigma}^{(n)} = 0$. The discrete form of this property is: $F_{K,\sigma}^{(n)} + F_{L,\sigma}^{(n)} = 0$. This is the basis of FVM method, and it is crucial for confirming convergence characteristics.

Discrete expressions in terms of discrete unknowns must then be given for the terms $A_K^{(n)}$, $F_{K,\sigma}^{(n)}$ and $S_K^{(n)}$. These discrete unknowns are usually estimations of the unknown functions $(u_j)_{\ j=1,\dots,N}$ at different locations (faces, vertices , grid blocks) and times. $u_{j,K}^{(n)}$ (resp. $u_{j,\sigma}^{(n)}$) is the estimation of function u_j in control volume *K* (resp. at face σ) at time $t^{(n)}$.

Examining the case in (6.14), the function *A* can be employed to define $A_K^{(n)}$:

$$A_K^{(n)} = \frac{1}{K}\int_K A\left(u_{1,K}^{(n)}, \dots, u_{N,K}^{(n)}, x, t^n\right)dx.$$

It is more difficult to obtain an expression for $F_{K,\sigma}^{(n)}$ from (6.14) complying with the discrete variables, due to no systematic method to empoly the function *F* which assures stability and accuracy on general grids. The arguments for the discrete expression of $S_K^{(n)}$ are generally $u_{j,K}^{(m)}, \dots, m = n$ or $n-1$.

6.3 MOL

Method of lines (MOL) is a general procedure for the solution of time dependent PDEs. The spatial, boundary value, derivatives in the PDE are replaced with algebraic approximations. Afterwards, the spatial derivatives are not declared explicitly in terms of the spatial independent variables. As a result, only the initial value variable remains, usually time.

The equation:

$$u_t + uu_x = 0 \tag{6.15}$$

is the linear advection equation. In physics, u is a linear or flow velocity. It is one of the simplest PDEs, but it can be challenging to integrate because it propagates discontinuities, a characteristic of first order hyperbolic PDEs.

An algebraic approximation must replace the spatial derivative u_x. This can be achieved using a finite difference:

$$u_z \approx \frac{u_i - u_{i-1}}{\Delta_x} \tag{6.16}$$

where *i* is an index indicating a position on a grid in x and Δ_x is the spacing in *x* on the grid, considered constant for the time being. The left end value of *x* is *i=1*, and the right end value of x is *i-M*. As a result, the grid in x has *M* points. The MOL approximation of eq. (6.15) is:

$$\frac{du_i}{dt} = -u\frac{u_i - u_{i-1}}{\Delta_x}, \quad 1 \le i \le M \tag{6.17}$$

Eq. (6.17) is an ODE because there is only one independent variable, *t*. It also represents a system of *M* ODEs. This change from a PDE, eq. (6.15), to a system of ODEs, eq. (6.17) is the basis of MOL. In order to calculate the solution of the PDE, a solution to the approximating system of ODEs is calculated. The determination of the

PDE problem must be done, before integrating *t*. Since eq. (6.15) is first order in *t* and in *x*, it requires one initial condition and boundary condition. They may be:

$$u(x, t = 0) = f(x) \tag{6.18}$$

$$u(x = 0, t) = g(t) \tag{6.19}$$

Since eqs. (6.17) comprise *M* initial value ODEs, *M* initial conditions are required and from eq. (6.18), these are:

$$\mathrm{u}(x_i, \mathrm{t} = 0) = \mathrm{f(x)}, \quad 1 \leq i \leq M \tag{6.20}$$

Also, utilization of boundary condition (6.19) gives grid point *i=1*

$$u(x_i, \mathrm{t}) = \mathrm{g(t)}, \quad \mathrm{t} \geq 0 \tag{6.21}$$

Eqs. (6.17), (6.20), (6.21) are the complete MOL approximation of eq. (6.15) subject to eqs. (6.18) and (6.19). The solution of this ODE system gives the *M* functions:

$$u_1(t), u_2(t), \ldots u_{M-1}(t), u_M(t) \tag{6.22}$$

that is, an approximation to $u(x, t)$ and the grid points $i = 1,2, \ldots M$.

ODE Integration within the MOL

The numerical integration of the *M* ODEs of eq. (6.17) is examined. If the derivative $\frac{du_i}{dt}$ is estimated by a first order FD:

$$\frac{du_i}{dt} \approx \frac{u_i^{n+1} - u_i^n}{\Delta t} + O(\Delta t) \tag{6.23}$$

where *n* is an index for the variable *t* (*t* moves onward in steps, *n*), then a finite difference is an estimation to the derivative of eq. (6.17):

$$\frac{u_i^{n+1} - u_i^n}{\Delta t} = -u \frac{u_i^n - u_{i-1}^n}{\Delta x}$$

or solving for u_i^{n+1}:

$$u_i^{n+1} = u_i^n - \left(\frac{u\Delta t}{\Delta x}\right)\left(u_n^i - u_{i-1}^n\right), i = 1,2, \ldots M \tag{6.24}$$

Eq. (6.24) has the valuable characteristic that it grants u_i^{n+1} explicitly. As a result, it can be solved at the advanced point in *t, n+1*, from the solution at the base point *n*. Explicit numerical integration of eqs. (6.17) using the forward finite difference eq. (6.23), is generally called the forward Euler method. This method is the most basic form of ODE integration.

While the explicit form of eq. (6.24) is computationally useful, it has a possible restrain. If the time step Δt is above a critical value, the computation becomes unstable, which is evident by successive changes in the dependent variable, $\Delta u = u_i^{n+1} - u_i^n$,

becoming larger and eventually unbounded as the computation moves onward in *t* (for increasing *n*). For this method eq. (6.24) to keep being stable, the dimensionless group ($u\frac{\Delta t}{\Delta x}$), which is called the Courant-Friedricks-Lewy or CFL number, must stay under a critical value, in this case, unity. As a result, there is an upper limit on Δt for a given *u* and Δx. When the accuracy must be increased of eq. (6.24) by using smaller Δx, a smaller value of Δt is essential to hold the CFL number under its critical value. As a result, there is difficulty in improving accuracy while keeping stability.

To bypass the stability limit of the explicit Euler method of eq. (6.23) a backward finite difference for the derivative in *t* can be used:

$$\frac{du_i}{dt} \approx \frac{u_i^n - u_i^{n-1}}{\Delta t} + O(\Delta t) \tag{6.25}$$

so, the finite difference approximation of eq. (6.17) is:

$$\frac{u_i^n - u_i^{n-1}}{\Delta t} = -u\frac{u_i^n - u_{i-1}^n}{\Delta x} \tag{6.26}$$

or after the rearrangement (with $\left(u\frac{\Delta t}{\Delta x}\right) = a$):

$$(1+a)u_i^n + au_{i-1}^n = u_i^{n-1}, i = 1,2,\dots M \tag{6.27}$$

The eq. (6.27) cannot be solved explicitly for the solution at the advanced point, u_n^i, in terms of the solution at the base point u_i^{n-1}. Eq. (6.27) is implicit in u_n^i due to u_{i-1}^n being also unknown. As a result, eq. 6.27 must be solved written for each grid point i=1,2,…*M* as a simultaneous system of bidiagonal equations. This is called the implicit Euler method. This method has no stability limit (is unconditionally stable comparing with the explicit method with the CFL number). If the ODE system approximating the PDE is nonlinear, a system of nonlinear algebraic equations must be calculated. The system of nonlinear equations is usually computed by a version of Newton's method which can be very demanding computationally for large number of ODEs.

Although there is no limit for stability, there is a limit for accuracy. One way to bypass this accuracy limitation is the use of a higher finite difference approximations for the derivatives in eq. (6.15). However, applying a von Neumann stability analysis it is demonstrated that this way does not certainly assure more accurate solutions, or even stable solutions.

CHAPTER 7

RESULTS

Numerical simulations based on the numerical implementation mentioned in chapter 6 are executed for various values of ultrasound intensities I and hydraulic conductivity $\widetilde{K}$. These simulations provide an understanding of the mechanisms involved in bone healing with US application. In order to evaluate the model, the predicted spatiotemporal evolution of tissue fractions in callus is compared with experimental data (Miedel et al. 2013, Harisson et al. 2003).

7.1 Effect of ultrasound on spatiotemporal tissue development

At the beginning of fracture healing, mesenchymal stem cells and fibroblasts migrate, and growth factors are released into the callus from adjacent tissues. Afterwards, mesenchymal stem cells differentiate into chondrocytes. Once chondrocytes become hypertrophic, they produce angiogenic growth factors. As a result, the angiogenic and chondrogenic mechanisms begin. Endochondral ossification occurs, through oxygen and nutrients delivered from vessels. Bone then gradually fills the fracture gap, while the densities of fibrous and cartilage tissue decrease.

In Fig. 7.1 the development of the tissue density in the callus during normal healing with US application is presented, for $\widetilde{D_p} = 2.35 \times 10^{-3}$ and $\widetilde{K} = 0.1$. At the beginning, the bone matrix density is minimum, but as the days pass and the fracture healing proceeds, it is gradually increased. Around day 15, blood vessels begin to develop networks. After the fracture, VEGF levels are very low. Around day 15 they reach the peak which is compatible with the appearance of vessels networks around the same day. As the fracture healing goes towards to the end, VEGF levels begin to reduce, until zero. Around day 1, interstitial fluid pressure is low and at the upper part of the geometrical domain, but gradually increases and spreads throughout the domain.

In Fig. 7.2 the development of the tissue density in the callus during normal healing without US application is presented. Both models can depict the mechanisms of bone healing. Without the US effect, the production of vascular growth factors starts at the first post fracture week (PFW 1) in periosteal callus, and at PFW 2 in the endosteal callus (Fig. 7.2). When US is applied, the angiogenesis occurs about a week earlier that without the US application, around day 3 PF in the periosteal callus and day 8 in the endosteal (Fig. 7.2).

In Fig. 7.1 the intercortical ossification starts around day 23, but in Fig. 7.2, without the US treatment, this happens around day 28-29. US influences branching and anastomosis mechanisms. As a result, the vascular network is created faster within the callus area and the bone is healed at around day 31 PF. Without the US the bone healing is completed around day 35 PF.

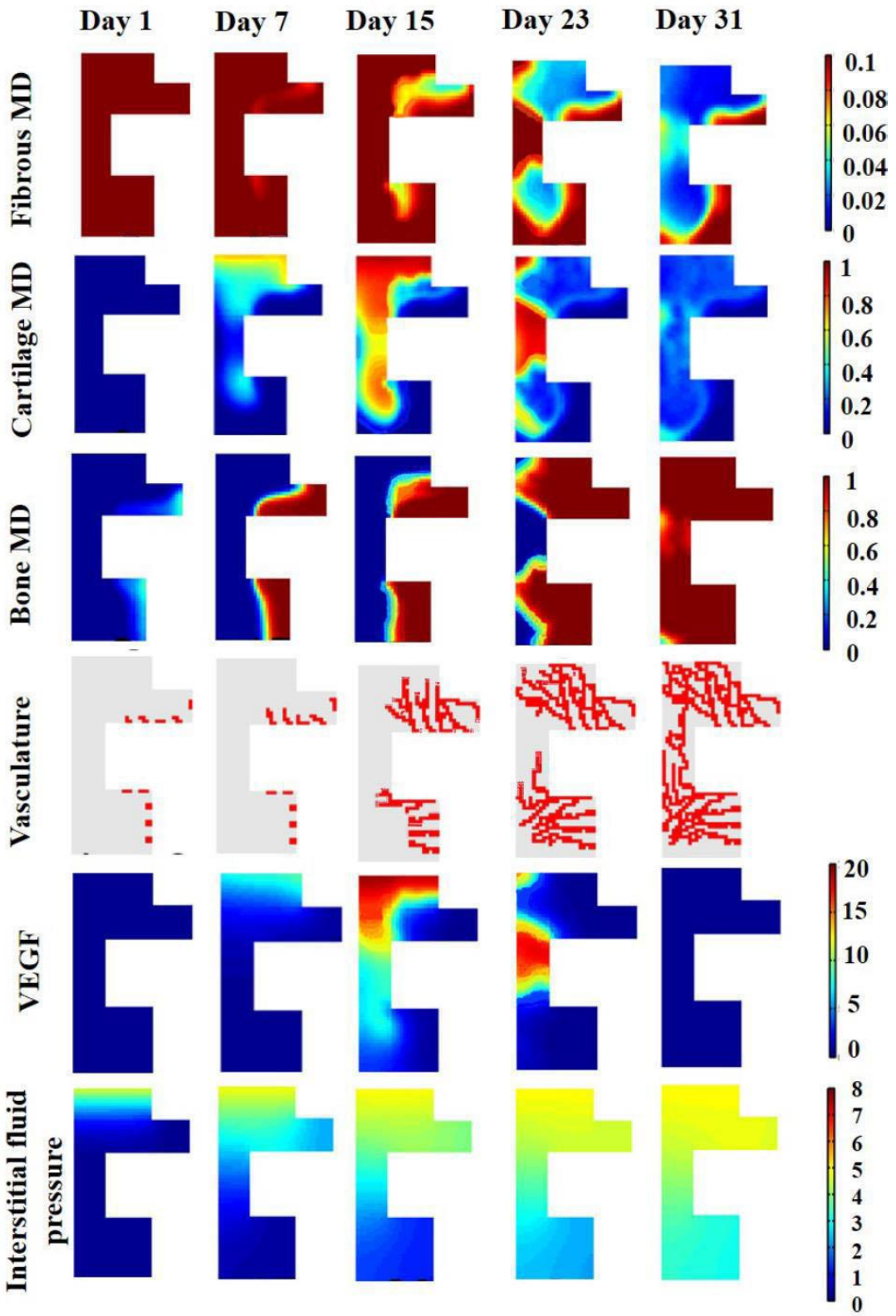

Figure 7.1 Predicted spatiotemporal development of fibrous tissue, cartilage bone matrix density (MD, x0.1g/ml), vasculature and VEGF under the effect of ultrasound in normal fracture healing ($\widetilde{D_p} = 2.35 \times 10^{-3}$) for $\tilde{K} = 0.1$, and the evolution of the interstitial fluid pressure of ultrasound.

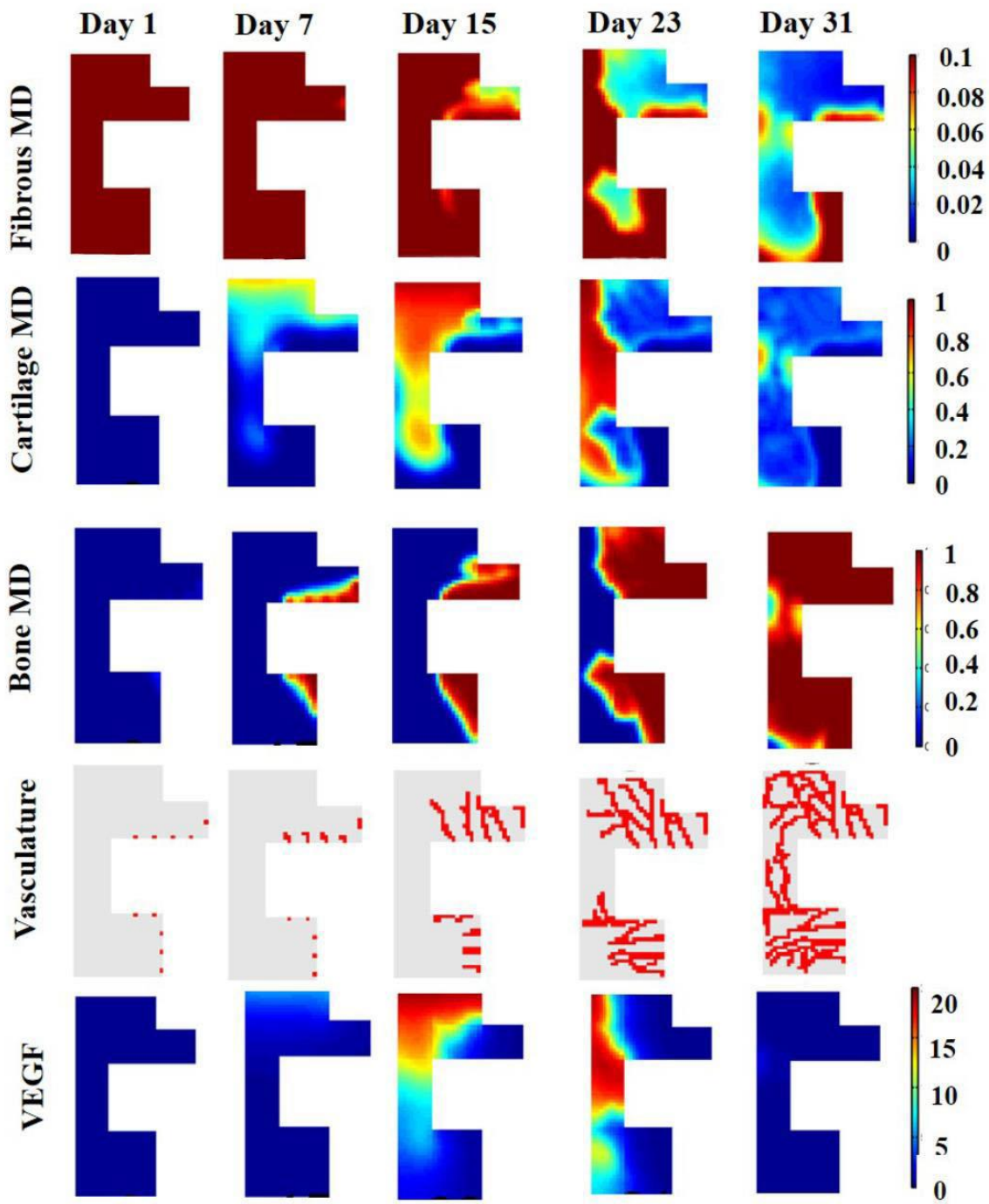

Fig. 7.2 Predicted spatiotemporal development of fibrous tissue, cartilage bone matrix density (MD, x0.1g/ml), vasculature and VEGF without the effect of ultrasound in normal fracture healing (Peiffer et al. 2011).

In Fig. 7.3 the development of tissue density in the callus during aged bone fracture healing, under the influence of US is presented. The parameters of the model were modified to consider the effect of aging. In normal fracture healing the process is completed around day 26 PF, but in an aged fracture healing it is completed around day 35. The blood vessels networks take longer time to develop than in normal healing. The production of VEGF starts around day 7 PF as in normal healing, however, the concentrations essential for the fracture healing take longer to be reached. The intercortical ossification starts around day 25 PF.

In Fig. 7.4 the development of tissue density in the callus during aged bone fracture healing, without the influence of US is presented. In this case also the fracture healing takes longer to complete, around day 40 PF. The endochondral ossification occurs around day 27 PF.

As a result, US application can aid fracture healing even in an aging patient, reducing fracture healing time. Clinical trials have also reported that US is an effective treatment for non-unions in the elderly. However, more clinical trials should be done in order to understand the exact mechanisms behind this effect.

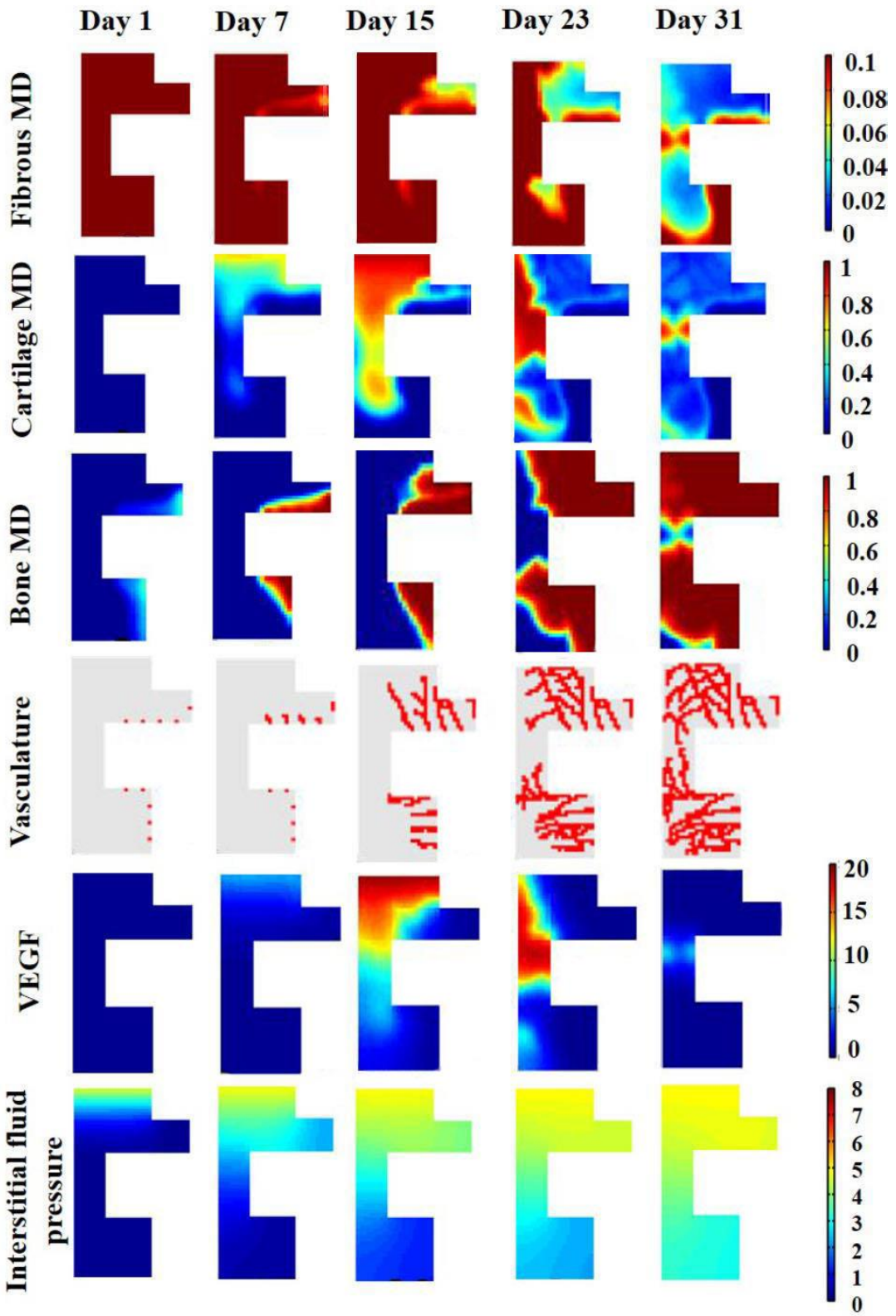

Figure 7.3 Predicted spatiotemporal development of fibrous tissue, cartilage bone matrix density (MD, x0.1g/ml), vasculature and VEGF under the effect of ultrasound in aged fracture healing ($\widetilde{D_p} = 2.35 \times 10^{-3}$) for $\widetilde{K} = 0.1$, and the evolution of the interstitial fluid pressure of ultrasound.

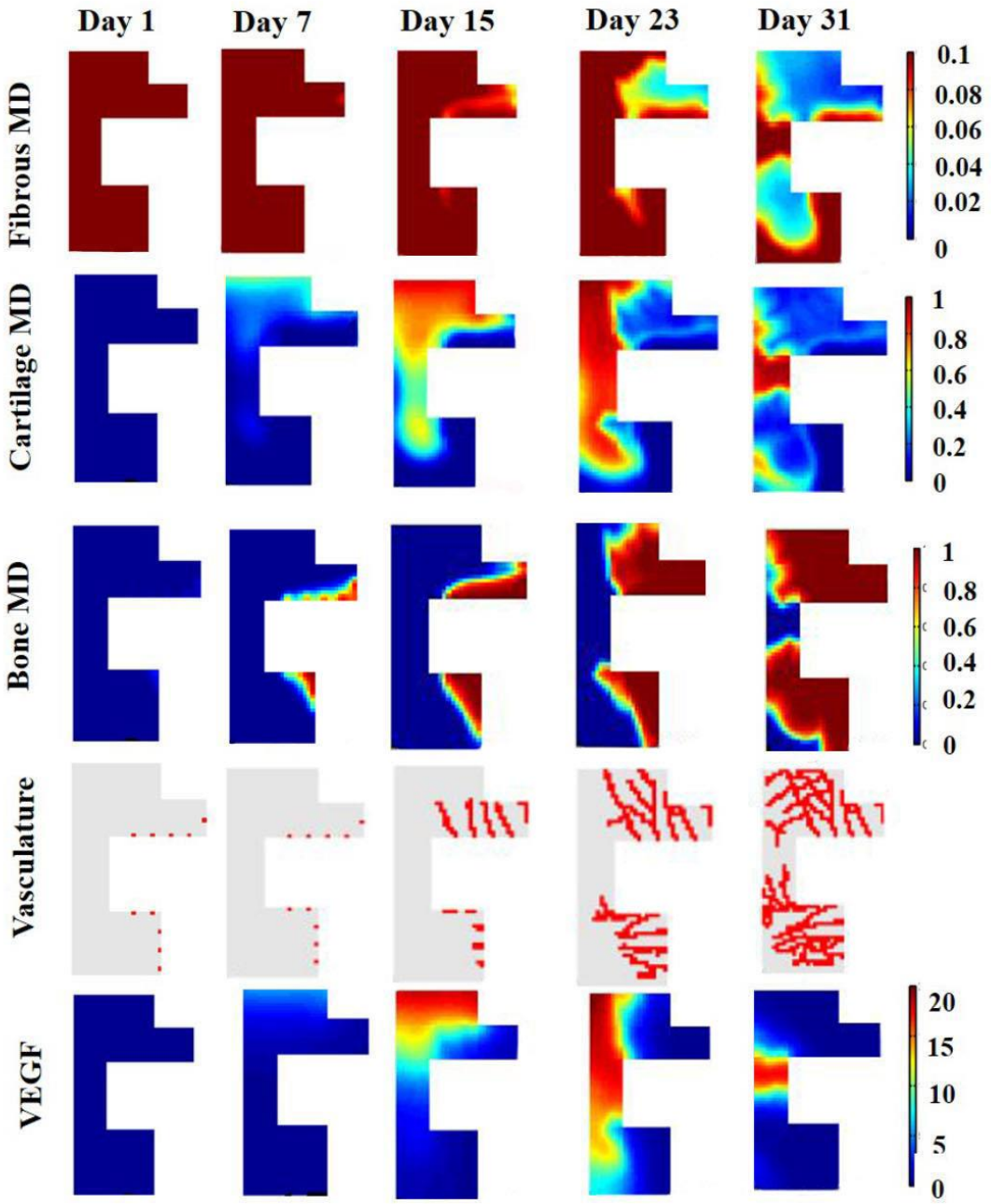

Figure 7.4 Predicted spatiotemporal development of fibrous tissue, cartilage bone matrix density (MD, x0.1g/ml), vasculature and VEGF under the effect of ultrasound in aged fracture healing ($\widetilde{D_p} = 2.35 \times 10^{-3}$) for $\tilde{K} = 0.1$.

7.2 Sensitivity analysis

Fig 7.5 demonstrates the blood vessel network for US intensity I=50mW/cm^2 and for three different values of $\tilde{K}$ (0.1, 0.01, 0.001). For $\tilde{K} = 0.1$ blood vessels' branching occurs earlier that in two other cases. At day 23 the blood vessels have occupied most of the periosteal and endosteal callus and begin to penetrate the intercortical callus. For $\tilde{K} = 0.01$ and for $\tilde{K} = 0.001$ the tip cells move in almost similar directions. As a result, as $\tilde{K}$ escalates, blood vessels produce more branches and fill the callus region earlier.

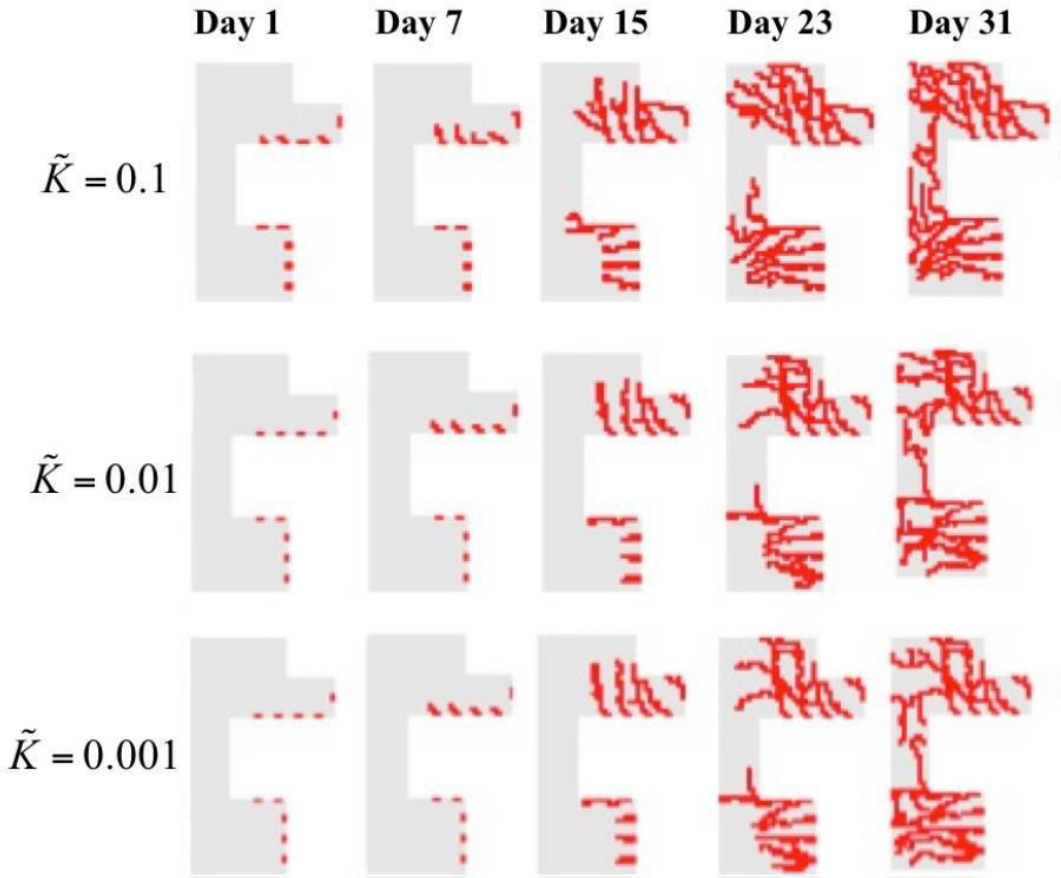

Figure 7.5 The development of vasculature for different values of $\tilde{K}$ from 0.001 to 0.1. The ultrasound intensity is I=50mW/cm^2.

Figure 7.6 demonstrates the development of bone matrix density and the vascular density in the callus area for three values of $\tilde{K}$ (0.1, 0.01, 0.001). The equivalent results collected from the model without the US application (Peiffer et al. 2011) are also illustrated in each figure. For $\tilde{K} = 0.1$ the bone matrix density is higher throughout the bone healing than for the other cases (Fig. 7.6(a)). The bone matrix is 84.23% at day 25 PF, whereas without US application it is equal to 69.53%. For $\tilde{K} = 0.01$ and $\tilde{K} = 0.001$, bone matrix density is almost indistinguishable and is higher than the case without US until day 23. Afterwards, it becomes slightly lower. This indicates a more distinct impact of US at the beginning of the healing procedure.

Similar results can be seen for the vascular densities in the callus (Fig. 7.6(b)). For $\tilde{K} = 0.1$ the vascular density is higher throughout the bone healing than for the other cases. The vascular density for $\tilde{K} = 0.1$ is equal to 40.06% at day 30 PF and 37.59% without the US. For $\tilde{K} = 0.01$ and $\tilde{K} = 0.001$, the vascular density follows a similar pattern until day 22 with values higher than the case without US application. Afterwards, in case for $\tilde{K} = 0.01$, it reaches higher values than the initial model. For $\tilde{K} = 0.001$, until the day 28, the vascular density is a little lower and at day 30 it has almost the same as the model without US.

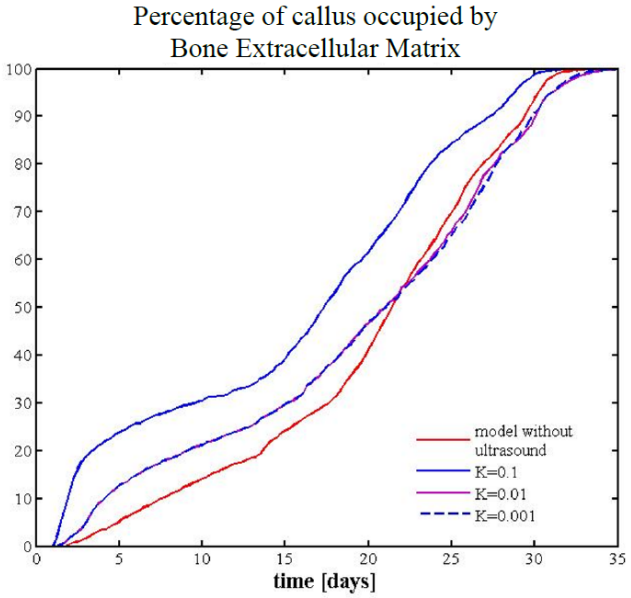

(a)

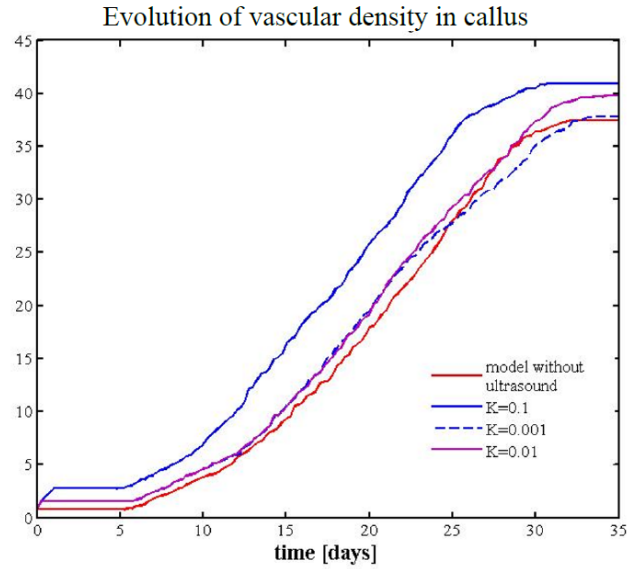

(b)

Figure 7.6 Predicted temporal development of (a) bone matrix density and (b) vascular density in callus for $\widetilde{K} = 0.001, 0.01, 0.1$. The equivalent results for the model without US (Peiffer et al. 2011) are also demonstrated.

Table 7.1 demonstrates the surface fraction of blood vessels in the callus throughout the healing procedure for US with $\widetilde{K} = 0.1$ and without US application. Increased fractions can be seen for the US model with the most important differences at PFW2 and PFW3.

	PFW2 (DAY 14)	**PFW3 (DAY 21)**	**PFW4 (DAY 28)**
$\widetilde{K} = 0.1$	14.18	27.54	39.50
Model without US	8.07	19.65	34.04

Table 7.1 Surface fractions of blood vessels in callus (%)

7.3 Influence of ultrasound intensity on vasculature evolution

In Fig. 7.7 the evolution of blood vessel network for different US intensities varying from 15 to 75mW/cm^2 is demonstrated. For all the cases, in PFW 1 the vasculature is restricted and there are a few blood vessels aside from the fracture line. After day 14 PF, the US stimulates the creation of branches in the periosteal and endosteal callus faster than the model without US. Furthermore, in all cases US directs the tips in almost similar directions different from those demonstrated in the model of Peiffer et al. (2011). At day 23 PF, the blood vessels have almost filled the callus apart from a small area in the endosteum. US accelerates angiogenesis, with the most distinct effect at the intensity of 60mW/cm^2. However, at 75mW/cm^2 there is not any significant impact. As a result, the intensity of 60mW/cm^2 is the best intensity for the enhancement of angiogenesis.

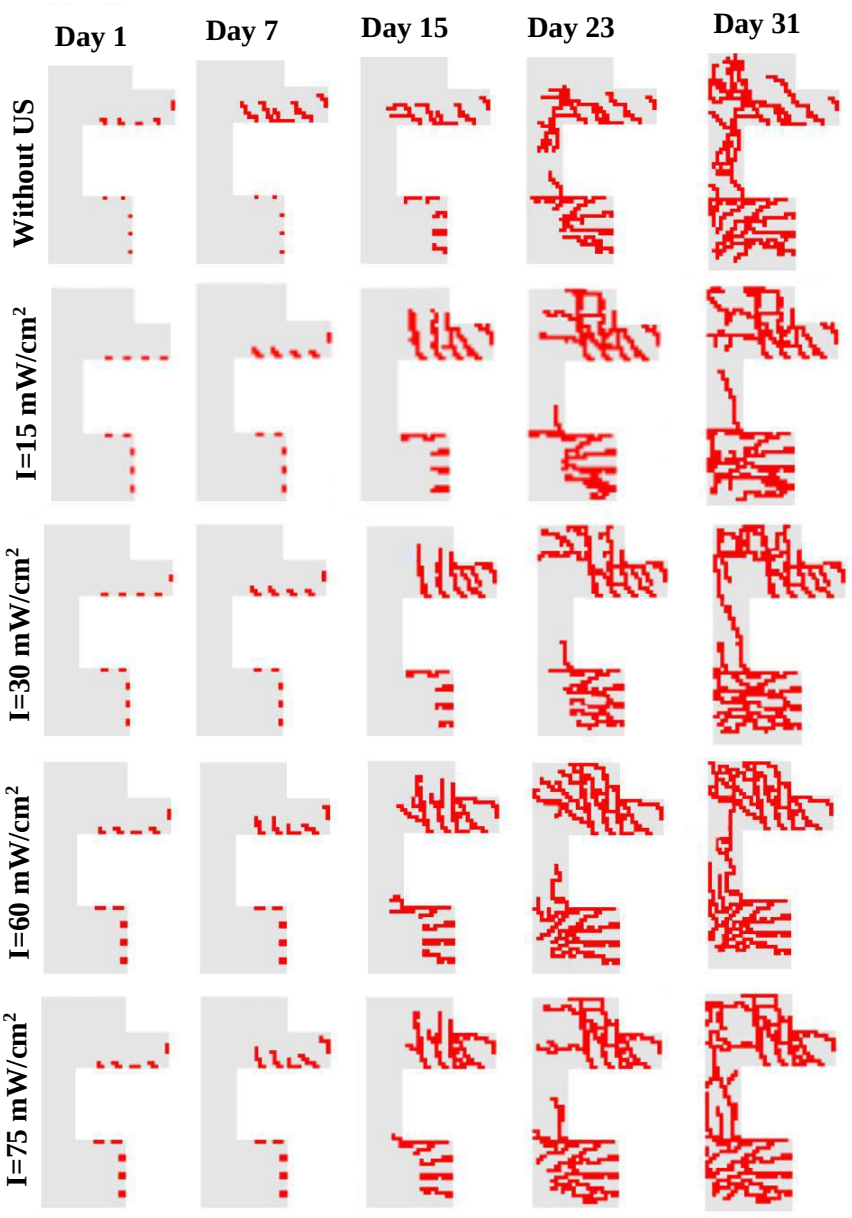

Figure 7.7 The development of vasculature for different US intensities varying from 15 to 75mW/cm^2, with $\tilde{K} = 0.1$. The correlated results for the model without the US effect (Peiffer et al.2011) is also demonstrated.

7.4 Comparison with experimental (*in vivo*) data

Fig. 7.8 compares the temporal development of the tissue fractions in the periosteal, intercortical and endosteal callus from experiments (Harrison et al. 2003), with the results of the Peiffer model (2011) and the results for the proposed US model (for $\widetilde{K} = 0.1$). To compute the tissue fractions, the spatial images were binarized using tissue-specific thresholds (when the tissue does not subsist the value is 0 and 1 when the tissue subsists in a grid cell). Afterwards, an equal weight was allotted to distinct tissues (if two tissues subsist in a grid cell, that grid cell region was divided by two). Both models can predict the general course of the experimental data. In fracture healing, as the bone fraction gradually increases, the fibrous tissue vanishes and the cartilage at the beginning increases, extend to a maximum and then drops.

US affects all the mechanisms of tissue development and degradation in the entire callus region. The fibrous tissue drops faster in the periosteal and endosteal callus that the model without US. Furthermore, in the experimental data, the cartilage numbers in the endosteal callus are higher than those predicted from US model. At day 5 the fibrous tissue fraction in the endosteal callus is 72% and at day 23 it is 2% in the US model. In the Peiffer model the corresponding values are 94% and 10%. At days 5 and 20 the fibrous tissue fraction is 80% and 42% respectively. Under the US effect, cartilage development in the endosteal callus begins at day 9 and is completed by day 25. Respectively, with no US influence, the cartilage formation begins at day 13 and is completed by day 30.

The bone tissue fraction increases faster in the US model with the most important differences in the endosteal callus. Callus bone fraction in increases from 60% (day 20) to 91% (day 30). Respectively, in the model without US, increases from 28% to 88% and in the experimental data from 55% to 74%. In the periosteal, callus bone fraction increases from 42% (day 15) to 93% (day 25). Respectively, in the model without US, increases from 30% to 85%.

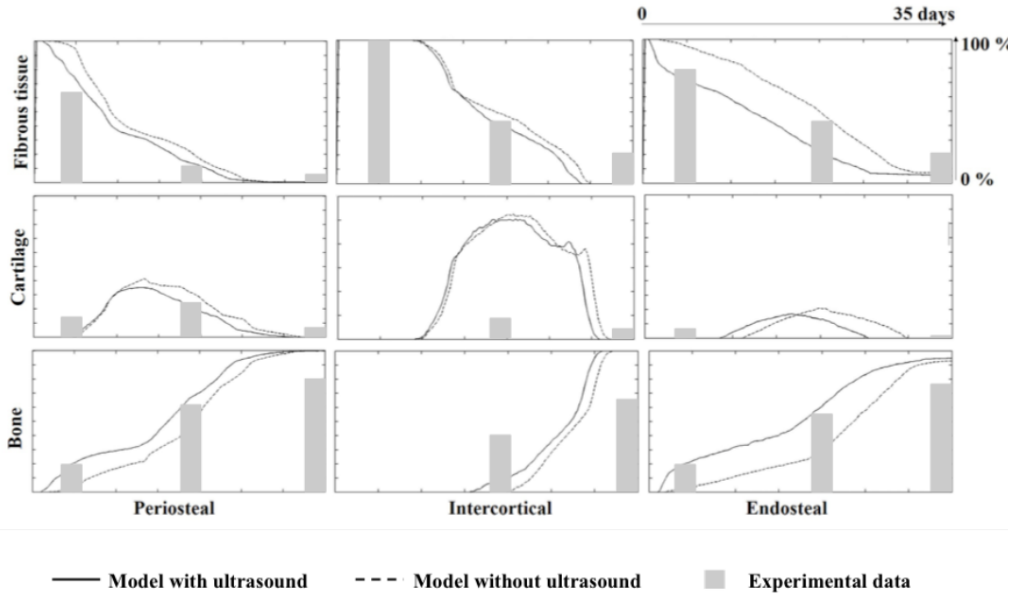

Figure 7.8 Temporal development of the bone cartilage and fibrous tissue fractions (%) in the periosteal, intercortical and endosteal callus collected from the newly introduced model ($\widetilde{K} = 0.1$) and the model of Peiffer et al. (2011).

7.5 Discussion

It was presented a hybrid mathematical model for deriving bone healing predictions under the US influence. The model was based on the one presented in Peiffer et al. (2011) and was further extended by including an additional equation describing the spatiotemporal evolution of the acoustic interstitial fluid pressure and appropriately modifying the equation that describes the spatiotemporal evolution of VEGF. US affects VEGF and other factors, but in this study only influence on VEGF was considered.

The hydraulic conductivity $\widetilde{K}$ was assumed equal to the permeability coefficient of the granulation tissue i.e. $\widetilde{K} = 0$. However, simulations were performed by assuming values which correspond to dimensionalized permeability coefficients of all tissues that take part in bone healing procedure in order to verify the assumption and investigate the model's sensitivity. Values outside the examined range caused either no blood vessel formation or physically unacceptable results and as a result they were ignored.

The model could capture intramembranous, endochondral ossification and other essential events in normal fracture healing. Due to the positive effect of the US on the angiogenesis process, the ossification process was accelerated by around 10 days. US causes i) an earlier beginning of angiogenesis in the periosteal and endosteal callus, ii) augmented branching of blood vessels and iii) the creation of blood vessel network was sped up throughout the whole callus area. US also accelerates aged bone healing, reducing healing time.

The sensitivity analysis for $\widetilde{K}$ demonstrates that US directs the tip cells in similar directions that are different from those in the initial model. In all the cases, after the second PF week, more dense blood vessel networks were developed due to enhanced branching, compared with no US effect. For $\widetilde{K} = 0.1$ the US had the most significant effect due to the highly affected VEGF transport by the US acoustic pressure. For $\widetilde{K} = 0.01, 0.001$ there was observed a delayed invasion of the tip cells in the endosteal callus because $\widetilde{K}$ is related to the ability of US passing through the callus area. For $\widetilde{K} = 0.1$, the bone matrix and vascular density had the highest values. Additionally, higher amounts of blood vessels were observed, particularly during weeks 2-4.

From previous studies, it has been demonstrated that US parameters affect the angiogenesis and bone healing. A range of intensities (15 to 75mW/cm^2) was examined, which are usually used in experimental studies. As the intensity was increased, the influence of US on the evolution of vasculature was enhanced. However, when the intensity was 75mW/cm^2, the US influence on angiogenesis was declined. As a result, the optimal intensity was 60mW/cm^2.

Comparisons between volume fractions in the endosteal, periosteal and intercortical callus among the computational models and experimental results indicated that both models can predict the spatiotemporal evolution of bone healing. However, both models indicate a faster resorption of fibrous tissue matrix and a faster evolution of fracture healing than the experimental observations. This could be due to 2D geometry instead of 3D. Furthermore, the maturation of the time cells is not considered in the hybrid model. It was also demonstrated that the cartilage density values were unnaturally increased, probably since oxygen and nutrients are not considered to the cartilage production process by the hybrid model.

Under the US influence, the cartilage fraction in the periosteal callus declines faster and cartilage formation and degradation in the endosteal callus take place earlier. This could be due to an earlier endochondral ossification. Several studies have also

indicated that US causes an earlier endochondral ossification as a result of an earlier chondrogenesis and cartilage hypertrophy. Furthermore, a faster decline in the fibrous tissue volume fraction and an augmented bone formation rate occur under the US influence. The model of Peiffer et al. (2011) predicted almost identical bone matrix percentages in the callus area at days 10 and 20 PF. However, the US model showed 20% higher bone formation within the callus area, showing the positive effect of US in fracture healing.

One limitation of the model is that the effect of the mechanical environment on the regeneration procedure is not considered. However, the effect of mechanical loading may be more noticeable in models of large animals, which is not the objective of this study. Another limitation is the simple 2D model. Similar models have been used in order to study the US propagation during bone healing (Protopappas et al. 2008). Moreover, when the ratio of the wall thickness to the outer radius is small, the theory predicts that US dispersion in tube can be practically approximated by the corresponding modes in a plate (Vavva et al. 2009). The use of lower-dimensional models as a first approach of a study is an established method in applied mathematics since computational costs and geometric complexity make the investigation of 3D models much more complex (Peiffer et al. 2011).

From previous experimental studies it has been shown that US influences several cellular procedures that take place during the bone healing. As a result, the model was extended in order to consider the influence of US on VEGF production. However, more studies must be conducted in order discover the exact influence of US on fracture healing and the parameters of US that are safe for clinical trials.

7.6 Conclusion

A bioregulatory model was introduced that involves the effect of US on bone healing process and angiogenesis. The effect of US on VEGF transport was modeled by inserting two additional parameters (D_p and K) in the mathematical framework and by applying an additional boundary condition of US acoustic pressure in the periosteal area of callus, in order to simulate the presence of US transducer during axial transmission. The enhancement of angiogenesis and bone healing was most for $\widetilde{K} = 0.1$. Additionally, after the examination of a range of intensities, 60mW/cm^2 was optimal for the invigoration of angiogenesis and bone healing. It was also indicated that US promotes the endochondral ossification, by comparing the predicted results of the model and experimental data. As a result, bone formation is accelerated, and healing time is reduced because of a much faster decline in the fibrous tissue volume fraction.

This model could be a step towards the creation of new mathematical models that could describe even more accurately the impact of US on bone healing. As a result, US could be used as a mean of monitoring the healing process and its endpoint.

REFERENCES

Anderson ARA, Chaplain MAJ. "Continuous and Discrete Mathematical Models of Tumor-induced Angiogenesis" *Bulletin of Mathematical Biology*, 1998, 60, 857–900.

Al-Qtaitat AI, Aldalaen SM. "A review of non-collagenous proteins; their role in bone" *American Journal of Life Sciences*, 2014, 2(6), 351-352.

Arikan H, Çiçek K. "Haematology of amphibians and reptiles: a review" *North-Western Journal of Zoology*, 2014, 10, 190–209.

Bayat M, Virdi A, Rezaei F, Chien S. "Comparison of the in vitro effects of low-level laser therapy and low intensity pulsed ultrasound therapy on bony cells and stem cells" *Progress in Biophysics and Molecular Biology*, 2018, 133, 36-48.

Bayat M, Virdi A, Virdi A, Jalalifirouzkouhi R, Rezaei F. "Comparison of effects of LLLT and LIPUS on fracture healing in animal models and patients: A systematic review" *Progress in Biophysics and Molecular Biology*, 2018, 132, 3-22.

Boskey AL, Coleman R. "Aging and bone" *J Dent Res*, 2010, 85(12), 1333-1348.

Bronoosh P, Tanideh A, Noorafshan A. "Effects of low-intensity pulsed ultrasound on healing of mandibular bone defects: an experimental study in rabbits" *Int. J. Oral Maxillofac. Surg.*, 2015, 44, 277–284.

Buckwalter JA, Hunzinker E, Rosenberg L. "Articular cartilage: composition and structure" *American Academy of Orthopaedic Surgeons*, 1988, 405-425.

Carlier A, Geris L, Castel N, Carmeliet G, Oosterwyck H. "Oxygen as a critical determinant of bone fracture healing—A multiscale model" *Journal of Theoretical Biology*, 2016, 392, 254-264.

Checa S, Prendergast PJ. "Including angiogenesis in mechanobiological models of tissue differentiation" *Journal of Biomechanics*, 2008, 37(1), 129-145.

Chen G, Niemeyer F, Wehner T, Simon U, Schuetz MA, Pearsy MJ, Claes LE. "Simulation of the nutrient supply in fracture healing" *Journal of Biomechanics*, 2009, 42, 2575–2583.

Cheung WH, Chow SK. "Low intensity pulsed ultrasound accelerated callus formation, angiogenesis and callus remodeling in osteoporotic fracture healing" *Ultrasound in Med.& Biol.*, 2011, 37(2), 231-238.

Cheung WH, Miclan T, Chow SK, Young F, Volker A. "Fracture healing in osteoporotic bone" *Injury, Int. J. Core Injured*, 2010, 47S2, 521-526.

Claes L, Willie B. "The enhancement of bone regeneration by ultrasound" *Progress in Biophysics and Molecular Biology*, 2007, 93, 384-398.

Eymard R, Gallouet T, Herbin R. "Finite volume methods" *Techniques of Scientific Computing, Part III*, 2000, 713-1020.

Foulke BA, Keydal AR, Murray DW, Pandit H. "Fracture healing in the ederly: a review" *Maturitas,* 2016, 92, 49-55.

Hamdi S, Schiesser WE, Griffiths GW. "Method of lines" *Scholarpedia*, 2007, 2(7), 2859.

Lu C, Saless N, Wang X. "The role of oxygen during fracture healing" *Bone*, 2003, 52, 220-229.

Cowin SC. "Bone Mechanics" *CRC Press*, 1989, 4-10.

Geris L, Vander Sloten J, Van Ooosterwysk H. "Connecting biology and mechanics in fracture healing: an integrated mathematical modeling framework for the study of nonunions" *Biomech Model Mechanobiol,* 2010, 9, 713–724.

Hu K, Olsen BR. "The roles of vascular endothelial growth factor in bone repair and regeneration" *Bone 91*, 2016, 30-38.

Imai Y, Hasegawa T, Takeda D. "The osteogenic activity of human mandibular fracture haematoma-derived cells is stimulated by low-intensity pulsed ultrasound in vitro" *Int. J. Oral Maxillofac. Surg.*, 2014, 43, 367–372.

Junqueira LC, Carneiro J, Foltin J, Lebowitz, H, Boyle PJ. "Basic Histology, Text & Atlas (10th ed.)" *McGraw-Hill Companies*, 2003, 106-144.

Farhi DC. "Pathology of bone marrow and blood cells (2nd ed.)", *Wolters Kluwer Health/Lippincott William & Wilkins*, 2008, 15-17.

Ferretti C, Mattioli-Belmonte M. "Periosteum derived stem cells for regenerative medicine proposals: Boosting current knowledge" *World Journal of Stem Cells*, 2014, 6(3), 266-277.

Fung CH, Cheung WH. "Effects of different therapeutic ultrasound intensities on fracture healing rats" *Ultrasound in Med. & Biol.*, 38(5), 2012, 745–752.

Krüger JP, Hondke S, Endres M, Pruss A, Siclari A, Kaps C. "Human platelet-rich plasma stimulates migration and chondrogenic differentiation of human subchondral progenitor cells" *Journal of Orthopedic Research*, 2012, 30(6), 845–52.

Lai CH, Chuang CC, Li JKJ. "Effects of Ultrasound on Osteotomy Healing in a Rabbit Fracture Model" *Ultrasound in Med. & Biol.*, 2011, 37(10), 1635-1643.

Laugier P, Haïat G. "Bone Quantitative Ultrasound" *Springer*, 2011, 1-6.

Mahamutha A, JothiPriya S. "Healing Mechanism in Bone Fracture" *Journal of Pharmaceutical Sciences and Research*, 2015, **7**(7), 441–442.

Malizos NM, Hantes ME, Protopappas V, Papachristos A. “Low-intensity pulsed ultrasound for bone healing: An overview” *Injury, Int. J. Care Injured*, 2006, 37S, 56-62.

Marsell R, Einhorn TA. "The biology of fracture healing" *Injury*, 2012, 42(6), 551-555.

Mehta JL, Mathur P, Dhalla NS. “Biochemical Basis and Therapeutic Implications of Angiogenesis (Advances in Biochemistry in Health and Disease)” *Springer*, 2017, 15-20.

Meisenberg G, Simmons W. “Principles of medical biochemistry” *Elsevier Health Sciences*, 2006, 243-250.

Milde F, Begdorf M, Koumoutsakos P. “A Hybrid Model for Three-Dimensional Simulations of Sprouting Angiogenesis” *Biophysical* Journal, 2008, 95, 3146–3160.

Netter FH, Dingle RV, Mankin HJ. “Musculoskeletal system: anatomy, physiology, and metabolic disorders” *Summit, New Jersey: Ciba-Geigy Corporation*, 1990, 170.

Nussbaum E. “The Influence of Ultrasound on Healing Tissues” *J Hand Therapy*, 1998, 11, 140-147.

Pounder NM, Harrison AJ. “Low intensity pulsed ultrasound for fracture healing: A review of the clinical evidence and the associated biological mechanism of action” *Ultrasonics*, 2008, 48, 330–338.

Rutten S, Nolte PA, Korstjens CM. “Low-intensity pulsed ultrasound increases bone volume, osteoid thickness and mineral apposition rate in the area of fracture healing in patients with a delayed union of the osteotomized fibula” *Bone*, 2008, 43, 348–354.

Rutten S, Nolte PA, Korstjens CM. “Low-intensity pulsed ultrasound affects RUNX2 immunopositive osteogenic cells in delayed clinical fracture healing” *Bone*, 2009, 45, 862–869.

Saran U, Piperni SG, Chatterjee S. “Role of angiogenesis in bone repair” *Archives of Biochemistry and Biophysics*, 2014, 561, 108-117.

Shefelbine JS, Augat P, Claes L, Simon U. “Trabecular bone fracture healing simulation with finite element analysis and fuzzy logic” *Journal of Biomechanics*, 2005, 38, 2440–2450.

Smith RS, Smith TJ, Blieden TM, Phipps RP. "Fibroblasts as sentinel cells. Synthesis of chemokines and regulation of inflammation" *The American Journal of Pathology*, 1997, 151 (2), 317–322.

Stegen S, Gastel N, Carmeliet G. “Bringing new life to damaged bone: The importance of angiogenesis in bone repair and regeneration” *Bone*, 2015, 70, 19-27.

Sun S, Wheeler MF, Obeysekere M, Patrick CW. "A deterministic model of growth factor-induced angiogenesis" *Bulletin of Mathematical Biology*, 2005, 67, 313–337.

Urist MR. "Fundamental and clinical bone physiology" *J. B. Lippincott Company*, 1980, 13-60.

Voet D, Voet J, Pratt C. "Fundamentals of Biochemistry: Life at the Molecular Level" *Hoboken, New Jersey: John Wiley & Sons*, 2016, 235.

Weiner R, Schmitt BA, Podhaisky H. "ROWMAP a ROW-code with Krylov techniques for large stiff ODEs" *Applied Numerical Mathematics*, 1997, 25, 303-319.